Mathematical Analysis of Host–Parasitoid Dynamics

Kelsey Marcinko

A dissertation
submitted in partial fulfillment of the
requirements for the degree of

Doctor of Philosophy

University of Washington

2020

Reading Committee:

Mark Kot, Chair

Nathan Kutz

Dobromir Dimitrov

Program Authorized to Offer Degree:
Department of Applied Mathematics

University of Washington

Abstract

Mathematical Analysis of Host–Parasitoid Dynamics

Kelsey Marcinko

Chair of the Supervisory Committee:
Associate Professor Mark Kot
Department of Applied Mathematics

Host and parasitoid systems are of great interest to ecologists, both because of the global prevalence of insect parasitoids and the impact of parasitoids in regulating their hosts. The direct connection between parasitized hosts and parasitoid offspring leads to simple and specific modeling assumptions. The discrete-time models used for host–parasitoid interactions are also sometimes used for more general predator–prey systems or even to describe consumer–resource dynamics in the broadest sense. In this dissertation, I examine some of the specific building blocks involved in formulation of host–parasitoid models and determine the impacts of these assumptions. I begin with an introduction that includes biological context and a brief overview of the mathematical frameworks used in my work.

Next, I present a systematic comparison and analysis of four discrete-time, host–parasitoid models. For each model, I specify that density-dependent effects occur prior to parasitism in the life cycle of the host. I compare density-dependent growth functions arising from the Beverton–Holt and Ricker maps, as well as parasitism functions assuming either a Poisson or negative binomial distribution for parasitoid attacks. I show that overcompensatory density-dependence leads to period-doubling bifurcations, which may be supercritical or subcritical. Stronger parasitism from the Poisson distribution leads to loss of stability of the coexistence

equilibrium through a Neimark–Sacker bifurcation, resulting in population cycles. My analytic results also revealed dynamics for one of my models that were previously undetected by authors who conducted a numerical investigation. In this section, I also emphasize the importance of clearly presenting biological assumptions that are inherent to the structure of a discrete-time model in order to promote communication and broader understanding.

Climate change has created new and evolving environmental conditions, impacting all species, including hosts and parasitoids. Building on my work with nonspatial host–parasitoid models, I next consider integrodifference equation (IDE) models of host–parasitoid systems to incorporate space and climate-driven shifts in habitats. I describe and analyze three IDE models of host–parasitoid systems to determine criteria for coexistence of the host and parasitoid. Specifically, I determine the critical habitat speed, beyond which the parasitoid cannot survive. By comparing the results from three IDE models, I investigate the impacts of assumptions that reduce the system to a single-species model. I also compare critical speeds predicted by a spatially-implicit difference-equation model with critical speeds determined from numerical simulations of the IDE system. The spatially-implicit model uses approximations for the dominant eigenvalue of an integral operator. The classic methods to approximate the dominant eigenvalue for IDE systems do not perform well for asymmetric kernels, including those that are present in shifting-habitat IDE models. Therefore, I compare several methods for approximating dominant eigenvalues and ultimately conclude that geometric symmetrization and iterated geometric symmetrization give the best estimates of the parasitoid critical speed.

TABLE OF CONTENTS

LIST OF FIGURES

LIST OF TABLES

ACKNOWLEDGMENTS

I want to first express gratitude to my advisor, Mark Kot. I have learned so much from Mark, and I appreciate the wealth of historical and mathematical knowledge that he has imparted to me, the time he invested in me, and his instruction on the nuanced distinction between a hyphen and an en dash. I wish to also thank the members of my committee, Nathan Kutz, Dobromir Dimitrov, and Patrick Tobin, for their guidance along the way.

The Department of Applied Mathematics has been an incredible community for the past five years. I am grateful to Bernard Deconinck for his consistent role as a mentor for me and for his words of encouragement in a particular conversation in my first year when I was questioning my ability to succeed in the program. The AMATH staff have also been cheerfully helpful and always supportive. A special thanks to Lauren Lederer, who has provided a safe place for any conversation and is someone that I can deeply trust. Thank you to Karen Beaudry for sharing a love of tea-drinking and for attending my general exam to support me. Thank you to Laurie Feldman and Sarah Riley for their support while I taught a CFRM class and managed a crisis situation. Thanks also to Alan Perry and Tony Garcia for taking care of logistical details, which are too often overlooked but necessary for all of our success. Thank you to all of the AMATH faculty for sharing their knowledge and advice.

I am filled with gratitude for all of my fellow students who have navigated this road with me and who have shared their advice, experiences, and wisdom. Firstly, thank you to my initial cohort for working and learning together in this endeavor — this also includes Brian Krouse, John Kerin, Riley Molloy, and Ali Brauer, who navigated the challenges of

the first year before moving on to other pursuits. Conversations and connecting with you all built an important foundation for my time at UW. Thank you to my counterpart, Kelsey Maass, who has been a steadfast friend from the very beginning. Thank you to Ben Liu and Nora Gilbertson, for conversations about mathematical ecology, practice presentations, suggestions for my work, and more importantly, laughter, support when things were tough, and friendship. Thank you to Katherine Owens for always being ready with a hug and conversations to pull me out of my work for a needed rest. Thanks to Ryan Creedon for sharing teaching ideas, being a great listener, and general enthusiasm. Thank you to older students whose advice and experiences have buoyed me and guided me, whether or not they recognized their impact: Jake Price, Sam Rudy, Brian de Silva, Jeremy Upsal, Kathleen Champion, Brisa Davis, Weston Barger, Andreas Freund, Donsub Rim, Saumya Sinha, Ben Segal, Lowell Thompson, Bethany Lusch and others. Thank you to Bethany Sutherland, for friendship and for coordinating gatherings of AMATH women for fun events!

One of the great joys of my time in Seattle has been the Teaching Discussion Group. I am particularly grateful to Jake Price, for creating and leading the group and for all that I have learned from him about teaching mathematics and navigating the path towards the career that I envision for myself. Thank you also to Craig Gin, a fellow teaching-enthusiast! Craig, thank you for your support, encouragement, brainstorming, wisdom, and friendship. I am also indebted to my previous teachers and professors for their role in preparing me to succeed and for their example of caring and mentorship through teaching.

Thank you to Allison Snyder, Monika Jelic, and Kate Kinsman for creating a welcoming home for my first year in Seattle. Thank you also to Will Pollock, Cristi Bratt, Kurtis and Krisula Reardon, and Jordan Scholten for years of friendship and support, and particularly for your company and laughter at monthly dinners during my first year. I deeply needed that space of fellowship and soul-care. Will, thank you also for your consistent encouragement,

listening, and prayer as we have both pursued PhDs at UW. Thank you also to many other friends that have listened and cared for me throughout this journey. Thank you to Colleen Forbes for countless cups of tea. Megan Morrison, thank you for being my housemate for the past four years and for all the ways that you have lifted and encouraged me. You are an inspiring applied mathematician, and I have missed you during the past few months!

I have been blessed also by several faith communities in Seattle. Thank you to the leadership and members of the Embrace UW group, including David and Laurie Brenner and Nathan Kutz. Thank you for creating such a unique space to consider the impact of faith in academia. Thank you to the Bible study ladies from UPC, my MC from the Hallows Church, and my CG at Trinity Church — I have been strengthened by knowing you and am grateful for your prayers and care.

Finally, words cannot express my thankfulness for my family. In addition to their faithful caring from a distance for four and a half years, they graciously welcomed me home for the final months of thesis-writing in the midst of a global pandemic. Mom and Dad, I would not be here today without you. Thank you. Justin, thanks for always believing in your sister and for listening whenever I needed to talk.

There are many more names that I could list here, but to keep things from getting too much longer, I will simply say that if I have not thanked you by name, know that I am nevertheless grateful for knowing you and for your role in this undertaking.

DEDICATION

For my teachers. From preschool to graduate school,
inside and outside the classroom, at home and in nature places.

Chapter 1

INTRODUCTION

The field of ecology, named by Ernst Haeckel in 1866, focuses on the interactions between organisms and the relationships between species and their environments [46]. Within population ecology, two of the major areas of investigation are the requirements for species to persist and the dynamics of extant populations. Ecologists want to know what environmental conditions are necessary for a particular species to exist in a given habitat, what habitat is suitable or optimal for a particular species, and how interactions between species will impact the dynamics of each population.

Within the scope of the incredible diversity of life, there is a large class of species for which there are discrete, non-overlapping generations, including, for example, many species of insects and annual plants. Difference-equation mathematical models are appropriate for such populations, especially for cases with well-synchronized births and deaths within the population. Studies and models that also incorporate space allow for more nuanced descriptions of population dynamics and densities across a landscape. Integrodifference equations (IDEs) combine discrete-time descriptions of a population with continuous space, explicitly describing distinct phases of population growth and dispersal in the life cycle of individuals.

In this dissertation, I specifically focus on using difference equations and IDEs to model the population dynamics of host–parasitoid systems. Parasitoids are incredibly abundant on earth and comprise somewhere between 4% and 10% of all metazoan, or multicellular, species [29, 32, 33]. Most parasitoids are in the order Hymenoptera (sawflies, ants, bees,

and wasps) or the order Diptera (two-winged flies) [29, 32, 33]. Adult female parasitoids lay their eggs on or inside a host egg, larvae, or pupae, depending on the particular parasitoid species. The parasitized host provides the source of nutrition for the parasitoid larvae during its development, and the host ultimately dies.

While host–parasitoid systems have been studied with mathematical models since Thompson's work in the 1920s [88, 89, 90] and Nicholson and Bailey's work in the 1930s [71], there continues to be much interest in further developing theoretical understanding and incorporating experimental data. Interest in studying parasitoids extends beyond the intrinsic value of furthering science; parasitoids have been studied and widely used in biological-control programs because of their role in regulating populations of agricultural pests [29, 62].

My work seeks to develop specific understanding of the impacts of a particular set of building blocks of host–parasitoid models. Different biological assumptions that characterize different mathematical models give different predictions and results for the dynamics of a host–parasitoid system. Before describing the specific elements that I investigated in the work in this dissertation, I will give a brief overview of the modeling frameworks used in my research.

1.1 Modeling population dynamics with difference equations

Growth of populations in nature is not unlimited. In general, one expects individuals in a population to compete for limited resources, and regulation of populations by density-dependent factors is a well-established principle. There are two particularly common single-species difference-equation models, each based on one of two types of intraspecific competition that limits population growth.

If a species exhibits contest competition, some individuals monopolize a resource, and thus resources are distributed unequally among individuals [70]. Population dynamics with

contest competition are often modeled with the Beverton–Holt stock-recruitment curve [12],

$$N_{t+1} = \frac{R_0 N_t}{1 + \frac{(R_0-1)}{K} N_t}, \tag{1.1}$$

where N_t is the size of the population at generation t. The net reproductive rate, R_0, is the largest possible per capita recruitment rate for the population. The carrying capacity of the population is denoted K.

Alternately, in scramble competition, resources end up divided relatively equally among the competitors [70]. The Ricker model [78] was also developed in the context of fisheries, but this model assumes scramble competition. The difference equation is

$$N_{t+1} = N_t e^{r(1-N_t/K)}, \tag{1.2}$$

where $r = \ln(R_0)$ is the intrinsic rate of growth.

Both equations (1.1) and (1.2) have equilibria at $N_t = 0$ and $N_t = K$, where equilibria or fixed points are found by letting $N_{t+1} = N_t = N^*$ and solving for N^*. At $N^* = 0$, the population is extinct and remains extinct. At $N^* = K$, births and deaths are equal, so the population size does not change over time. The parameter R_0 (or r) determines whether the population will approach the extinction fixed point or the carrying capacity fixed point over time. If $R_0 < 1$ ($r < 0$), the population approaches extinction. For the Beverton–Holt model, if $R_0 > 1$, the population approaches its carrying capacity, K, and we say that $N^* = K$ is asymptotically stable and $N^* = 0$ is unstable. For the Ricker equation, if $0 < r < 2$, then K is asymptotically stable. For $r > 2$, the Ricker model displays more complicated dynamics, eventually including chaos.

A general difference equation model for two interacting species is

$$N_{t+1} = F_N(N_t, P_t), \tag{1.3a}$$

$$P_{t+1} = F_P(N_t, P_t). \tag{1.3b}$$

Fixed points for a two-species system are found by letting $N_{t+1} = N_t = N^*$ and $P_{t+1} = P_t = P^*$ and solving system (1.3) for all solution pairs (N^*, P^*). Stability of each fixed point is determined by computing the Jacobian of system (1.3),

$$J(N,P) = \begin{bmatrix} \frac{\partial F_N}{\partial N} & \frac{\partial F_N}{\partial P} \\ \frac{\partial F_P}{\partial N} & \frac{\partial F_P}{\partial P} \end{bmatrix}, \tag{1.4}$$

and evaluating the Jacobian at fixed point (N^*, P^*). If the eigenvalues of the resulting matrix satisfy $|\lambda_1|, |\lambda_2| < 1$, then the fixed point is asymptotically stable. If either $|\lambda_1| > 1$ or $|\lambda_2| > 1$, the fixed point is unstable.

A fixed point where only the host persists is known as an exclusion equilibrium [7, 10, 42, 43, 54]. If both populations persist, then the system is in a coexistence state. Throughout this dissertation, I will be examining the conditions and biological parameters that determine whether a host–parasitoid system results in extinction, exclusion (host-only existence), or coexistence. In Chapter 2, I will also consider whether the coexistence state is a fixed point, a cycle, or a more exotic attractor.

1.2 Integrodifference equations

The mathematical models analyzed in Chapter 3 are integrodifference-equation (IDE) models. Integrodifference equations have been largely embraced by ecologists to develop mechanistic models for investigating population dynamics. These models are especially beneficial and relevant in the context of changing environmental conditions globally. Studies of population persistence with spatial constraints have the potential to inform policy decisions about refuges, habitat use, and human development in the context of conservation. Spatial ecologists are also concerned about the dynamics of invading populations. In many cases, nonnative invading species can have detrimental impacts on local populations, and are broadly contributing to the global biodiversity crisis [66]. Alternatively, in biological control, a natural-enemy species may be intentionally introduced into an environment for

the purpose of controlling an invading host species. Decisions regarding biological control may be guided by spatial mathematical models of population dynamics. These types of models can also be used to predict the impact of range expansions due to climate change and the ability of a species to colonize newly suitable habitat. As other habitats shrink or move polewards in latitude or upwards in elevation, mathematical IDE models can be used to predict a species' ability to shift with the habitat. Numerous researchers have contributed to the use of integrodifference equations in studying these pressing questions. I refer those who are interested to Lutscher's [57] recently published text, which provides an excellent survey of IDEs in spatial ecology.

The simplest integrodifference equation for a species with discrete, nonoverlapping generations is

$$N_{t+1}(x) = \int_{\Omega} k(x,y) f\left[N_t(y)\right] dy, \tag{1.5}$$

where $N_t(x)$ is the population density at location x of the t-th generation. At each spatial location, y, the population grows according to the recruitment function, f. Individuals then disperse according to the dispersal kernel, $k(x,y)$, representing movement from location y to location x. The population density at location x at time $t+1$ is then found by integrating over the spatial domain, Ω, to account for contributions from all locations y at the previous time-step. For a particular y, the dispersal kernel is a probability density function in x.

One of the benefits of modeling with integrodifference equations is the flexibility to choose a kernel that best approximates the dispersal of a given species. The behavior of IDEs with certain classes of kernels differs drastically from the dynamics resulting from classic reaction-diffusion models [53], such that the predictions from IDEs are better approximations for some biological systems.

The direct motivation for my own work began with a transition in recent years from studying biological invasions with IDEs to studying whether species can keep up with climate-driven range shifts. Zhou and Kot [105, 106] developed an IDE model for a single species in

a moving habitat to determine the critical speed, c^*, of the habitat shift beyond which the population cannot survive. In order to incorporate more biological realism into this basic model, Harsch et al. [31] developed an IDE model to determine the critical speed for an age- or stage-structured population on a moving habitat. To investigate the implications of a more realistic two-dimensional habitat, Phillips and Kot [74] explored the effects of width and length of a two-dimensional patch on population persistence. They also considered the effects of different types of dispersal kernels on critical speed for these more geometrically complicated habitat patches.

A moving-habitat IDE model for a single species has the form

$$N_{t+1}(x) = \int_{-L/2+ct}^{L/2+ct} k(x,y) f\left[N_t(y)\right] dy, \tag{1.6}$$

where the habitat is shifting with climate velocity c. Beyond a critical speed, c^*, the population cannot persist. For a single species, the critical speed depends on the dispersal kernel (both the average dispersal distance and the shape of the kernel), the patch length, L, and the specifics of the recruitment function, f.

Because populations do not exist in isolation, the next logical step is to incorporate interspecific interactions into IDE moving-habitat models. Rinnan [80] modeled two competing species with a shifting habitat patch to determine conditions for extinction, coexistence, and extirpation of one of the two species. My original goal and motivation was to build on the analysis of moving-habitat IDE models, now with a different category of interspecific interactions, those of host–parasitoid systems. Chapter 3 details the results of my work with host–parasitoid IDE models.

1.3 "Building blocks" and their impacts

Throughout this dissertation, I am interested in developing an understanding of the specific consequences of different modeling assumptions or choices, the contributions of different "building blocks" of a model, in other words. What are the ranges of possible dynamics of a

host–parasitoid system with compensatory vs. overcompensatory density-dependence? Can the dynamics of a two-species system be approximated by a model that is reduced to a single species? Is an IDE model still useful if I remove the "building block" that explicitly models space?

Additional complexity can always be incorporated into a model. In the context of host–parasitoid models, one could consider systems with Allee effects, spatial refuges, multiple competing parasitoids, hyperparasitism, age or stage structure, etc. While each of these factors can contribute additional biological realism to a model, I argue that it is critical to understand the impacts of the basic building blocks before investigating a more complicated mathematical model.

In Chapter 2, I consider non-spatial models of host–parasitoid systems to develop an understanding of the range of potential population dynamics in simple nonspatial models. In my initial reading, it became apparent that a large number of papers did not provide sufficiently clear explanations of the biological assumptions underlying their models. The work of May et al. [61] indicates that the sequence of density dependence and parasitism in the life cycle of the host can greatly impact the resulting population dynamics. My work compares the dynamics of four models, developed with the explicit assumption that density-dependence precedes parasitism in the life cycle of the host. I compare the resulting dynamics and the impact of assuming compensatory vs. overcompensatory density-dependence and the difference between a fractional and an exponential form of parasitism. Recall that intraspecific contest competition is linked to compensatory density-dependence, while scramble competition is linked to overcompensatory density-dependence. The different parasitism functions arise from differing assumptions about how parasitoids may or may not aggregate in searching for hosts [60]. The models studied here yield rich mathematical phenomena including chaos, and I was able to determine how different building blocks in the model change the resulting dynamics in the system.

In Chapter 3, I develop and analyze discrete-time, continuous-space IDE models for host–parasitoid systems affected by climate-driven range shifts. Broadly, the analysis in this chapter allows me to consider when simplifications of the full two-species explicit-space IDE model result in useful predictions about the critical speed for host and parasitoid coexistence. In this chapter, I consider three specific IDE models. For the first case, I approximate the host population with the assumption that it exists on a large enough habitat to be considered infinite in comparison to the finite parasitoid habitat patch. Additionally, I assume high enough host reproduction that the density of the host is at its carrying capacity throughout its habitat. The system reduces to a single IDE equation for the parasitoid, similar to the way that Neubert et al. [69] approximated a predator invasion by assuming that the predator wave has negligible impact on the prey.

For the second and third cases of Chapter 3, I consider a true two-species IDE system and instead simplify the problem by representing space implicitly, rather than explicitly. This is accomplished by averaging the host and parasitoid populations over their patches and reducing the IDE system to a system of difference equations. Space is implicitly included in the difference-equation system with a term that approximates the effective survivorship after dispersal. This approximation doesn't indicate the shape of the population distribution of either the host or parasitoid on the habitat patch, but it provides sufficient information to predict the critical speed when the parasitoid species will go extinct and the system will approach an exclusion state asymptotically. There are many ways to approximate the proportion of individuals that land in the habitat-shifted patch after dispersal. Mathematically, this is a problem of approximating the dominant eigenvalue of a particular integral operator. I compare the accuracy of a number of these approximations in predicting the critical speed. I also include two iterative methods that can be used to improve the critical speed estimation. My hope is that my comparison of methods and recommendations will guide other researchers in further study of IDEs with moving habitats.

At this point, the biological motivation for improving theoretical understanding and mathematical modeling of host–parasitoid systems should be clear. Hosts and parasitoids are incredibly abundant. Climate change, devastation of crops by agricultural pests, and loss of biodiversity are all pressing global challenges. It is my hope that my work has made a contribution, however small, to improving scientific understanding of hosts and parasitoids, as well as the broader field of population ecology. In any case, though I did not anticipate studying population dynamics of insects when I began my time at the University of Washington, I have grown to more deeply appreciate the complexities of population ecology and specifically, the rich nuances of modeling hosts and parasitoids.

Chapter 2

A COMPARATIVE ANALYSIS OF HOST–PARASITOID MODELS WITH DENSITY DEPENDENCE PRECEDING PARASITISM

2.1 Introduction

The interactions between insect parasitoids and their hosts are of great interest to ecologists. Roughly 8.5% of insect species are parasitoids [29], and they play a significant role in regulating their hosts. Because parasitoid species are specialists on suitable prey, they are often used in biological control programs. This has fueled much interest in developing a better understanding of the dynamics of parasitoids and their hosts. Mathematical models of these host–parasitoid systems are also notable because of the simple and specific modelling assumptions that result from the direct connection between parasitized hosts and parasitoid offspring.

Nicholson and Bailey [71] laid the foundation for the study of discrete-time host–parasitoid models. Their basic model assumed that oviposition by parasitoids is limited by the number of encounters with hosts and not by parasitoid egg-supply. In addition, they assumed that the number of encounters with hosts is proportional to host abundance and that hosts are equally susceptible to randomly distributed encounters. Their model, however, yields unstable dynamics. As a result, much of the subsequent literature has sought to investigate factors that induce stability.

In a particularly influential paper, Beddington et al. [9] incorporated density-dependent

host recruitment, resulting in the model

$$N_{t+1} = N_t e^{r\left(1-\frac{N_t}{K}\right)} e^{-aP_t}, \tag{2.1a}$$

$$P_{t+1} = cN_t \left(1 - e^{-aP_t}\right). \tag{2.1b}$$

Here, N_t is the host density, P_t is the parasitoid density, r is the intrinsic rate of growth, K is the host carrying capacity, a is the parasitoid searching efficiency or area of discovery, and c is the parasitoid clutch size. For a detailed explanation of searching efficiency, see [71].

Beddington et al. [9] did not specify the life-stage of the host species for which N_t is the density. This is in contrast to Nicholson and Bailey [71], who provide extensive biological detail for their model. Beddington et al.'s model also fails to provide a coherent explanation of when the density dependence and parasitism occur during the life cycle of the host. Specifying the order of events is critical when both density dependence and parasitism affect the host population.

Model (2.1) is an example of the more generalized model

$$N_{t+1} = N_t g(N_t) f(P_t), \tag{2.2a}$$

$$P_{t+1} = cN_t[1 - f(P_t)]. \tag{2.2b}$$

Model (2.2) assumes that parasitism affects the original N_t hosts, so that a fraction of hosts, $f(P_t)$, survive parasitism. The survivors then produce offspring with a per capita recruitment, $g(N_t)$, that depends on the original number of hosts. The model also assumes that new parasitoids are produced in proportion to the number of parasitized hosts. Murdoch et al. [64] note that the host biology described above is unlikely, though May et. al. [61] provide the example of the winter moth (*Operophtera brumata*) and a fly, *Cyzenis albicans*, that have this biology.

May et al. [61] evaluated model (2.2) along with two other models to investigate whether the temporal sequence of host density-dependence and parasitism can affect the dynamics

of the populations. In a conclusion that is consistent with the earlier findings of Wang and Gutierrez [98], May et al. noted that the 'sequence of density dependence and parasitism in the host life-cycle can have a significant effect on the population dynamics' [61]. May et al. further recommended that model (2.2) be abandoned unless the biology of a particular system demands it.

Numerous investigators [7, 22, 23, 32, 36, 37, 43, 45, 54] have nevertheless cited Beddington et al. [9] and use the structure of model (2.2). These authors often derive their models from previous work, without a careful explanation of the underlying biology. Many books [4, 20, 25, 65, 91] also present some version of model (2.2). Mills et al. [62], Murdoch et al. [64], and Hassell [33], are among the few authors who recognize and discuss the biological assumptions inherent in model (2.2).

In this chapter, we carefully develop, analyze, and compare four models that assume that density-dependent growth precedes parasitism. These models correspond to a biologically reasonable alternative system presented by May et al. [61]. We consider two functions for density dependence of the host and two functions for parasitism. For each combination of these nonlinear functions, we perform stability analyses to determine dynamics and bifurcations. From these analyses, we conclude that stronger nonlinearity in the density-dependence term produces different effects than stronger parasitism.

This chapter has eight sections. In the second section, we present the biological assumptions underlying our models and the general form of our equations. In the third section, we outline our methods of analysis. In the following four sections, we present four models. The first two models use a fractional function for parasitism, while the next two models use an exponential form. The first and third models assume compensatory density-dependence, while the second and fourth models include overcompensatory density-dependence. The first model yields highly stable dynamics. The second model has a period-doubling route to chaos. A Neimark–Sacker bifurcation occurs in the third model. The fourth model has exponential

functions for both density dependence and parasitism, leading to the greatest variability in dynamics. For certain parameter values, there are two interior equilibria, no more than one of which is stable. Both a Neimark–Sacker bifurcation and a subcritical period-doubling bifurcation occur in this model. We conclude with a discussion of the value of understanding the differences between these models.

2.2 Model formulation

We now consider the model

$$N_{t+1} = N_t G(N_t) F(P_t), \tag{2.3a}$$

$$P_{t+1} = cN_t G(N_t)[1 - F(P_t)]. \tag{2.3b}$$

Although this model is consistent with more than one biological scenario, we make several specific choices here. Let N_t be the density of reproducing host adults, and let P_t be the density of adult female parasitoids. $G(N_t)$ is the host per-capita-recruitment. $F(P_t)$, in turn, is the fraction of host offspring that escape parasitism, while $1 - F(P_t)$ is the fraction of host offspring that succumb to parasitism.

In order to analyze zero-growth isoclines more easily, we let $H(P_t)$ be the fraction of hosts that succumb to parasitism per adult female parasitoid,

$$H(P_t) = \frac{1 - F(P_t)}{P_t}. \tag{2.4}$$

System (2.3) can now be written

$$N_{t+1} = N_t G(N_t)[1 - P_t H(P_t)], \tag{2.5a}$$

$$P_{t+1} = cN_t G(N_t) P_t H(P_t), \tag{2.5b}$$

where c is the clutch size. More precisely, c is the average number of female parasitoids laid on a single host that emerge and successfully become reproducing adults. This model is consistent with the second formulation discussed by May et al. [61].

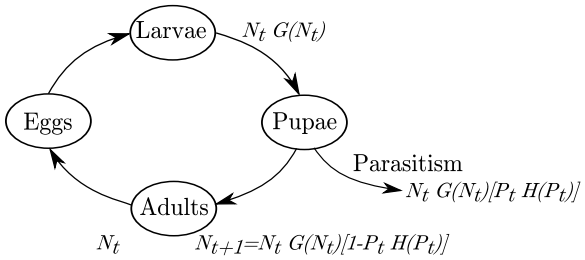

Figure 2.1: A host life-cycle diagram that illustrates a set of biological assumptions that match the formulation of the model set-up with density-dependent competition preceding parasitism. N_t is the density of viable adult hosts that reproduce, and P_t is the density of adult female parasitoids.

Figure 2.1 illustrates a host life-cycle scenario that matches the biological assumptions of system (2.5). As above, N_t is the density of reproducing host adults. These adults lay eggs that hatch into larvae. The larvae compete for resources, and $N_tG(N_t)$ larvae survive to the end of larval development. The larvae become pupae, some of which are parasitized, leaving N_{t+1} adults in the next generation.

Although the scenario we have described is that of a pupal parasitoid, we emphasize that this is not the only biological scenario described by systems (2.3) and (2.5). The key point, emphasized by Murdoch [64] and Hassell [33], is that this formulation matches a host life-cycle in which density-dependent competition precedes parasitism.

We now return to the model. For host density-dependent recruitment, we compare Beverton–Holt growth,

$$N_tG(N_t) = \frac{R_0N_t}{1+\frac{(R_0-1)}{K}N_t}, \tag{2.6}$$

and the Ricker curve,

$$N_tG(N_t) = N_te^{r\left(1-\frac{N_t}{K}\right)}. \tag{2.7}$$

Here $R_0 = \exp(r)$ is the net reproductive rate, $r = \ln(R_0)$ is the intrinsic rate of growth, and K is the carrying capacity. Recall that the Beverton–Holt growth function is compensatory while the Ricker growth function is overcompensatory.

Early investigators [71, 89] used the zero term of the Poisson distribution for $F(P_t)$, the fraction of hosts that escape parasitism. May [60] considered varying levels of aggregation and proposed the use of the zero term of the negative binomial distribution,

$$F(P_t) = \left(1 + \frac{aP_t}{\kappa}\right)^{-\kappa}. \tag{2.8}$$

May's use of this function influenced Livadiotis et al. [55], who studied system (2.2) with κ-parameterized functions for both parasitism and density-dependent intraspecific competition. The formulation used by Livadiotis et al. highlights the similarities in the exponential ($\kappa \to \infty$) and rational ($\kappa = 1$) functions most commonly used for $F(P_t)$ and $G(N_t)$.

In this chapter, we focus on two forms of May's function, given by $\kappa = 1$ and $\kappa \to \infty$. From equation (2.4), these values of κ give the fraction of hosts that succumb to parasitism per adult female parasitoid as

$$H(P_t) = \frac{a}{1 + aP_t} \tag{2.9}$$

and

$$H(P_t) = \frac{1}{P_t}\left(1 - e^{-aP_t}\right) \tag{2.10}$$

respectively.

Other than in May et al.'s paper [61], system (2.5) has not been studied in a way that compares functional forms for modelling parasitism and density dependence. Using equations (2.6), (2.7), (2.9), and (2.10) with system (2.5), we will formulate four possible models and compare their dynamics in Sections 2.4–2.7.

2.3 Methods of analysis

Each of our four models can be written in the general "density-dependence first" form of system (2.5). We now nondimensionalize. If we let $y_t = aP_t$, $x_t = N_t/K$, and $b = acK$, we obtain

$$x_{t+1} = x_t u(x_t, y_t), \tag{2.11a}$$

$$y_{t+1} = y_t v(x_t, y_t), \tag{2.11b}$$

where

$$u(x_t, y_t) = g(x_t)[1 - y_t h(y_t)], \tag{2.12}$$

$$v(x_t, y_t) = b x_t g(x_t) h(y_t). \tag{2.13}$$

For Beverton-Holt growth,

$$g(x_t) = \frac{R_0}{1 + (R_0 - 1)x_t}, \tag{2.14}$$

while for Ricker growth,

$$g(x_t) = e^{r(1-x_t)}. \tag{2.15}$$

Both expressions of per-capita recruitment can be found from $G(N_t)$ by directly substituting $x_t = N_t/K$. We will call (2.14) *fractional per-capita-recruitment*, which produces compensatory density-dependence, and (2.15) *exponential per-capita-recruitment*, which produces overcompensatory density-dependence.

Similarly, the fraction of hosts that succumb to parasitism, $yh(y)$, can be rewritten with

$$h(y_t) = \frac{1}{1 + y_t}, \tag{2.16}$$

for $\kappa = 1$, and

$$h(y_t) = \frac{1}{y_t}\left(1 - e^{-y_t}\right), \tag{2.17}$$

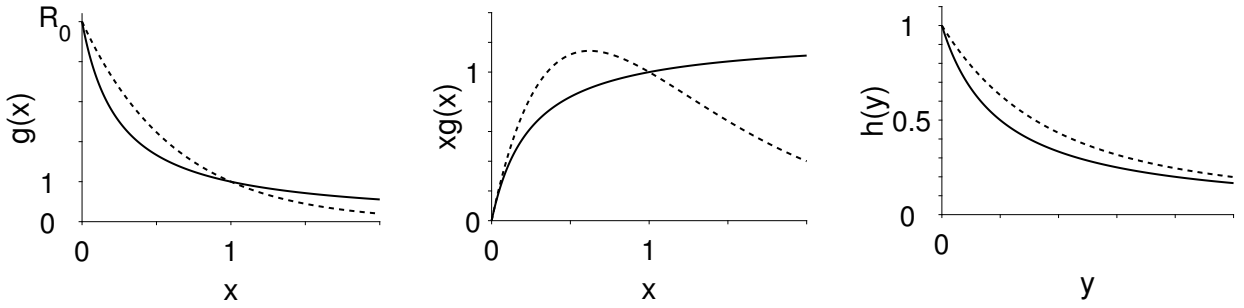

(a) Host per-capita-recruitment (b) Host recruitment (c) Parasitism

Figure 2.2: These figures illustrate the behavior of $g(x)$, $xg(x)$, and $h(y)$ for functions used in our models. Fractional forms of $g(x)$ and $h(y)$ from equations (2.14) and (2.16) are shown with solid lines. Exponential forms of $g(x)$ and $h(y)$ from equations (2.15) and (2.17) are shown with dashed lines. Both functions for $g(x)$ are monotonically decreasing from R_0. Recruitment, $xg(x)$, is non-monotonic for the exponential form, while it is monotonic for the fractional form. Both fractional and exponential forms of $h(y)$ are positive and monotonically decreasing. The dashed curve remains above the solid curve as y increases.

for $\kappa \to \infty$. For both cases, to get $h(y_t)$ from $H(P_t)$, it is necessary to divide by a and then substitute $y_t = aP_t$. We will refer to (2.16) as *fractional parasitism* and (2.17) as *exponential parasitism.*

In all that follows, we assume $R_0 \geq 1$ ($r \geq 0$), since we choose to consider cases where the host species can persist in the absence of the parasitoid species. For $R_0 > 1$ ($r > 0$), the per-capita recruitment, $g(x_t)$, is a positive, monotonically decreasing function that starts from $R_0 = \ln(r)$ at $x_t = 0$ and crosses 1 at $x_t = 1$. Similarly, $h(y_t)$ is positive and monotonically decreasing, with $h(0) = 1$. Sample plots of $g(x)$, $xg(x)$, and $h(y)$ are shown in Figure 2.2.

To find the equilibria of system (2.11), we set $x_{t+1} = x_t = x^*$ and $y_{t+1} = y_t = y^*$. The

equilibria occur at (0,0), (1,0), and at solutions of the system

$$1 = u(x^*, y^*) = g(x^*)[1 - y^* h(y^*)], \tag{2.18a}$$

$$1 = v(x^*, y^*) = bx^* g(x^*) h(y^*). \tag{2.18b}$$

For each of our models, it can be shown that $b > 1$ is a necessary and sufficient condition for the existence of a *unique* positive solution to system (2.18). For the fourth model, there is a region below $b = 1$ for which two positive solutions to system (2.18) exist.

To determine the stability of the equilibria, we form the Jacobian matrix of partial derivatives for system (2.11),

$$J(x, y) = \begin{pmatrix} xu_x + u & xu_y \\ yv_x & yv_y + v \end{pmatrix}, \tag{2.19}$$

where we drop the t subscripts for notational simplicity. After evaluating the partial derivatives, the Jacobian may be rewritten

$$J(x, y) = \begin{pmatrix} [xg'(x) + g(x)][1 - yh(y)] & -xg(x)[yh'(y) + h(y)] \\ byh(y)[xg'(x) + g(x)] & bxg(x)[yh'(y) + h(y)] \end{pmatrix}, \tag{2.20}$$

where we factor to separate the x and y dependencies. We will use the Jacobian evaluated at each of equilibria of system (2.11) to determine stability.

2.3.1 Host-only system summary

In the absence of the parasitoid, system (2.11) reduces to

$$x_{t+1} = x_t g(x_t). \tag{2.21}$$

For fractional recruitment, the host population goes extinct if $R_0 < 1$. All values of x are neutrally stable equilibria if $R_0 = 1$. For $R_0 > 1$, the host density will approach the asymptotically stable equilibrium, $x = 1$.

For exponential recruitment, the host population will die out if $r < 0$. Similarly to the fractional recruitment case, all values of x are neutrally stable equilibria if $r = 0$. The host population will persist if $r > 0$. If $0 < r < 2$, the point $x = 1$ is an asymptotically stable equilibrium. At $r = 2$, a supercritical flip (period-doubling) bifurcation occurs. The attractor in the system becomes a two-cycle, which persists as r continues to increase, until another period-doubling occurs, and there is a stable four-cycle. Period doubling continues as r increases, until the system becomes chaotic.

The dynamics of this system are particularly relevant as we now consider the extinction and exclusion equilibria of system (2.11). Understanding the period-doubling route to chaos in the host-only system with exponential recruitment is also useful when interpreting the dynamics of the host–parasitoid system with exponential recruitment, especially in Section 2.5.

2.3.2 Extinction equilibrium

At the *extinction point* $(0, 0)$, the Jacobian,

$$J(0,0) = \begin{pmatrix} g(0) & 0 \\ 0 & 0 \end{pmatrix} = \begin{pmatrix} R_0 & 0 \\ 0 & 0 \end{pmatrix}, \tag{2.22}$$

has eigenvalues R_0 and 0. Note that we used $g(0) = R_0$, which was mentioned previously. The extinction equilibrium is unstable for $R_0 > 1$. The zero eigenvalue indicates that for initial conditions with $x = 0,\ y > 0$, the system will collapse to the $(0, 0)$ fixed point at the next generation due to the lack of hosts.

2.3.3 Exclusion equilibrium

The equilibrium point (1,0) is known as an *exclusion point* [7, 42, 43]. Here, the host population persists at carrying capacity, while the parasitoid population is extinct. The

Jacobian for this system is

$$J(1,0) = \begin{pmatrix} g'(1)+g(1) & -h(0) \\ \\ 0 & bh(0) \end{pmatrix} = \begin{pmatrix} g'(1)+1 & -1 \\ \\ 0 & b \end{pmatrix}, \tag{2.23}$$

since $h(0) = 1$ for equation (2.16) and $\lim_{y\to 0} h(y) = 1$ for equation (2.17). The eigenvalues for this triangular system are thus

$$\lambda_1 = g'(1) + 1, \quad \lambda_2 = b. \tag{2.24}$$

Recall that $g'(1)$ is negative since $g(x)$ is monotone decreasing for $R_0 > 1$ ($r > 0$). Based on the eigenvalues in (2.24), we conclude that the exclusion equilibrium will be asymptotically stable if

$$-2 < g'(1) < 0 \tag{2.25}$$

and $b < 1$. The second inequality in condition (2.25) is satisfied, so we will check the first inequality for both forms of the host per-capita-recruitment, $g(x)$.

For equation (2.14),

$$g'(1) = \frac{(1-R_0)}{R_0}, \tag{2.26}$$

and the first inequality in (2.25) becomes

$$-2R_0 < 1 - R_0, \tag{2.27}$$

which simplifies to $-1 < R_0$. Since the net reproductive rate, R_0, is positive, this inequality is true, and the stability of the exclusion equilibrium point hinges on the value of b for our models that use fractional recruitment. For $b < 1$, the equilibrium is asymptotically stable, and for $b > 1$, the equilibrium is unstable.

For equation (2.15),

$$g'(1) = -r. \tag{2.28}$$

Thus, $|\lambda_1| < 1$ if and only if $-2 < -r < 0$. For our models that use exponential recruitment, $b < 1$ is not sufficient for asymptotic stability of the exclusion equilibrium. If both $b < 1$ and $0 < r < 2$, then the exclusion equilibrium will be asymptotically stable.

Recall that $R_0 \geq 1$ ($r \geq 0$) is necessary for the host to persist when alone. For the host-only system with fractional recruitment, the equilibrium $x = 1$ is asymptotically stable for $R_0 > 1$. For the host-only system with exponential recruitment, $x = 1$ is asymptotically stable if $r > 0$ *and* $r < 2$. For the host–parasitoid system with either fractional or exponential recruitment, when $b < 1$, a small parasitoid population is unable to increase when the host is at $x = 1$.

2.3.4 Coexistence equilibria

The *coexistence equilibria* are the solutions to system (2.18). Biologically, coexistence occurs when both x^* and y^* are positive. These equilibria can be explicitly determined for models using fractional parasitism, but not for exponential parasitism. Nevertheless, the coexistence equilibria can be approximated numerically for all cases.

We evaluate Jacobian matrix (2.19) at the coexistence equilibrium, (x^*, y^*), and use equations (2.18a) and (2.18b), which are satisfied at coexistence equilibria, to simplify. We obtain

$$J(x^*, y^*) = \begin{pmatrix} x^* u_x + 1 & x^* u_y \\ y^* v_x & y^* v_y + 1 \end{pmatrix}. \tag{2.29}$$

To avoid unnecessarily complicated algebra, we will not proceed from eigenvalues.

We will instead determine sufficient conditions for asymptotic stability of the coexistence equilibria by applying the Jury conditions [40] to each model. The Jury conditions are

necessary and sufficient conditions for asymptotic stability in the linearized system. As such, they provide sufficient conditions for asymptotic stability in the nonlinear system. The Jury conditions can be written

$$1 - \tau + \Delta > 0, \tag{2.30}$$

$$1 + \tau + \Delta > 0, \tag{2.31}$$

$$\Delta < 1, \tag{2.32}$$

where τ is the trace and Δ is the determinant of the Jacobian matrix evaluated at the implicit or explicit coexistence equilibrium. In τ–Δ space, the intersection of the regions defined by the Jury conditions is a triangle, shown in [4] and [20] and described by [99], where both eigenvalues are less than one in modulus.

Recall that the stability of a hyperbolic equilibrium is accurately determined by analyzing its stability in the linearized system. For our system with R_0 (or r) and b parameters such that (τ, Δ) is inside or outside the triangle, the coexistence fixed point is hyperbolic. Outside the triangle, at least one eigenvalue exceeds one in magnitude, so the fixed point is unstable in the nonlinear system.

On the boundary of the triangle, we cannot use the linearized system to determine the stability of the coexistence fixed point in the nonlinear system. At least one eigenvalue is exactly one in magnitude on the triangle boundaries, meaning that the fixed point is non-hyperbolic, and nonlinear terms are needed to determine stability. However, we will not concern ourselves with stability of non-hyperbolic points since they generally coincide with bifurcations in our models.

Losing stability by violating the first Jury condition, inequality (2.30), corresponds to the dominant eigenvalue leaving the unit circle through positive one. If the system instead loses stability when inequality (2.31) is first violated, the dominant eigenvalue leaves the unit circle through negative one, causing a flip bifurcation. In both of these cases, the non-dominant eigenvalue remains within the unit circle when the bifurcation occurs. If both

the first and second Jury conditions are satisfied and stability is lost through violating the third Jury condition, the eigenvalues are a complex-conjugate pair that leave the unit circle simultaneously.

For a system with τ and Δ that violate two of the three Jury conditions, both eigenvalues will be larger than one in magnitude (or equal to one in magnitude on the corners of the triangle). For further details on the Jury conditions and bifurcations, see Kuznetsov [50] and Whitley [99], though the Jury conditions are not referenced by name in these sources.

For matrix (2.29),

$$\tau = 2 + x^* u_x + y^* v_y, \tag{2.33}$$

and

$$\Delta = 1 + x^* u_x + y^* v_y + x^* y^* (u_x v_y - u_y v_x). \tag{2.34}$$

Using these expressions, the first Jury condition, inequality (2.30), simplifies to

$$x^* y^* (u_x v_y - u_y v_x) > 0. \tag{2.35}$$

The first Jury condition will be violated for parameter values such that $x^* = 0$ or $y^* = 0$. For a true coexistence equilibrium point with positive x^* and y^* values, inequality (2.35) requires

$$u_x v_y - u_y v_x > 0. \tag{2.36}$$

We now consider the second Jury condition, inequality (2.31). After we write the inequality in terms of u, v, x^*, and y^*, the condition simplifies to

$$4 + 2x^* u_x + 2y^* v_y + x^* y^* (u_x v_y - u_y v_x) > 0. \tag{2.37}$$

Finally, the third Jury condition, inequality (2.32), can be expressed as

$$1 + x^* u_x + y^* v_y + x^* y^* (u_x v_y - u_y v_x) < 1. \tag{2.38}$$

These three Jury conditions, inequalities (2.35), (2.37), and (2.38), will be used for each specific model to determine the requirements on parameters b and R_0 (or r) to ensure that the coexistence equilibrium is stable.

2.4 *Model 1: Compensatory host density-dependence and fractional parasitism*

The first model we consider uses fractional per-capita-recruitment (2.14) and fractional parasitism (2.16). The model is thus

$$x_{t+1} = \left[\frac{R_0 x_t}{1+(R_0-1)x_t}\right]\left(\frac{1}{1+y_t}\right), \tag{2.39a}$$

$$y_{t+1} = b\left[\frac{R_0 x_t}{1+(R_0-1)x_t}\right]\left(\frac{y_t}{1+y_t}\right). \tag{2.39b}$$

The coexistence equilibrium for this system is

$$(x^*, y^*) = \left(\frac{1}{b}, \frac{R_0}{1+(R_0-1)\left(\frac{1}{b}\right)} - 1\right). \tag{2.40}$$

As shown in Appendix 2.10.1, for $R_0 > 1$, this equilibrium is in the interior of the first quadrant if and only if $b > 1$. For $b = 1$, the equilibrium given by equation (2.40) is the exclusion equilibrium, $(1, 0)$. For $R_0 = 1$, system (2.39) has a line of equilibria on the x-axis, and (2.40) reduces to $(1/b, 0)$.

2.4.1 Stability region

Compensatory (fractional) host recruitment, $xg(x)$, and fractional parasitism are both rational functions, which correspond to a low κ index in the parameterized families of common recruitment and parasitism functions (see Livadiotis et al. [55]). When we use fractional per-capita-recruitment for $g(x)$ and fractional parasitism for $h(y)$, the model has a large stability region as seen in Figure 2.3a. All three Jury conditions are satisfied for the region in parameter space defined by $b > 1$, $R_0 > 1$. The first Jury condition is violated for $b = 1$.

Crossing this line corresponds to a transcritical bifurcation. Both the first and third Jury conditions are violated for $R_0 = 1$. Details are given in Appendix 2.10.2–2.10.4. Satisfying the three Jury conditions ensures that the coexistence equilibrium is asymptotically stable.

2.5 *Model 2: Overcompensatory host density-dependence and fractional parasitism*

Our second model also uses fractional parasitism, but it incorporates the exponential per-capita-recruitment from equation (2.15). As seen in Figure 2.2b, exponential recruitment is nonmonotonic, so we have introduced stronger nonlinearity in the density-dependence term. These choices yield the model

$$x_{t+1} = x_t e^{r(1-x_t)} \left(\frac{1}{1+y_t} \right), \tag{2.41a}$$

$$y_{t+1} = b x_t e^{r(1-x_t)} \left(\frac{y_t}{1+y_t} \right). \tag{2.41b}$$

The coexistence equilibrium for this system,

$$(x^*, y^*) = \left(\frac{1}{b}, e^{r(1-1/b)} - 1 \right), \tag{2.42}$$

is again in the interior of the first quadrant if $r > 0$, $b > 1$. This is shown in Appendix 2.11.1. For $b = 1$, the equilibrium given by equation (2.42) is the exclusion equilibrium, $(1, 0)$. For $r = 0$, system (2.41) has a line of equilibria on the x-axis, and (2.42) reduces to $(1/b, 0)$.

2.5.1 Stability region

As was true for Model 1, the first Jury condition is satisfied for $b > 1$, $r > 0$ ($R_0 > 1$), and the third Jury condition is satisfied for $r > 0$ ($R_0 > 1$). Substituting the exponential form of density dependence in place of the fractional form from Model 1 introduces an additional stability criterion for the coexistence equilibrium for Model 2. The second Jury condition is now satisfied above the curve defined, for $3/2 < \omega < 2$, by

$$r = \omega - \ln(2\omega - 3), \quad b = 1 - \frac{1}{\omega} \ln(2\omega - 3). \tag{2.43}$$

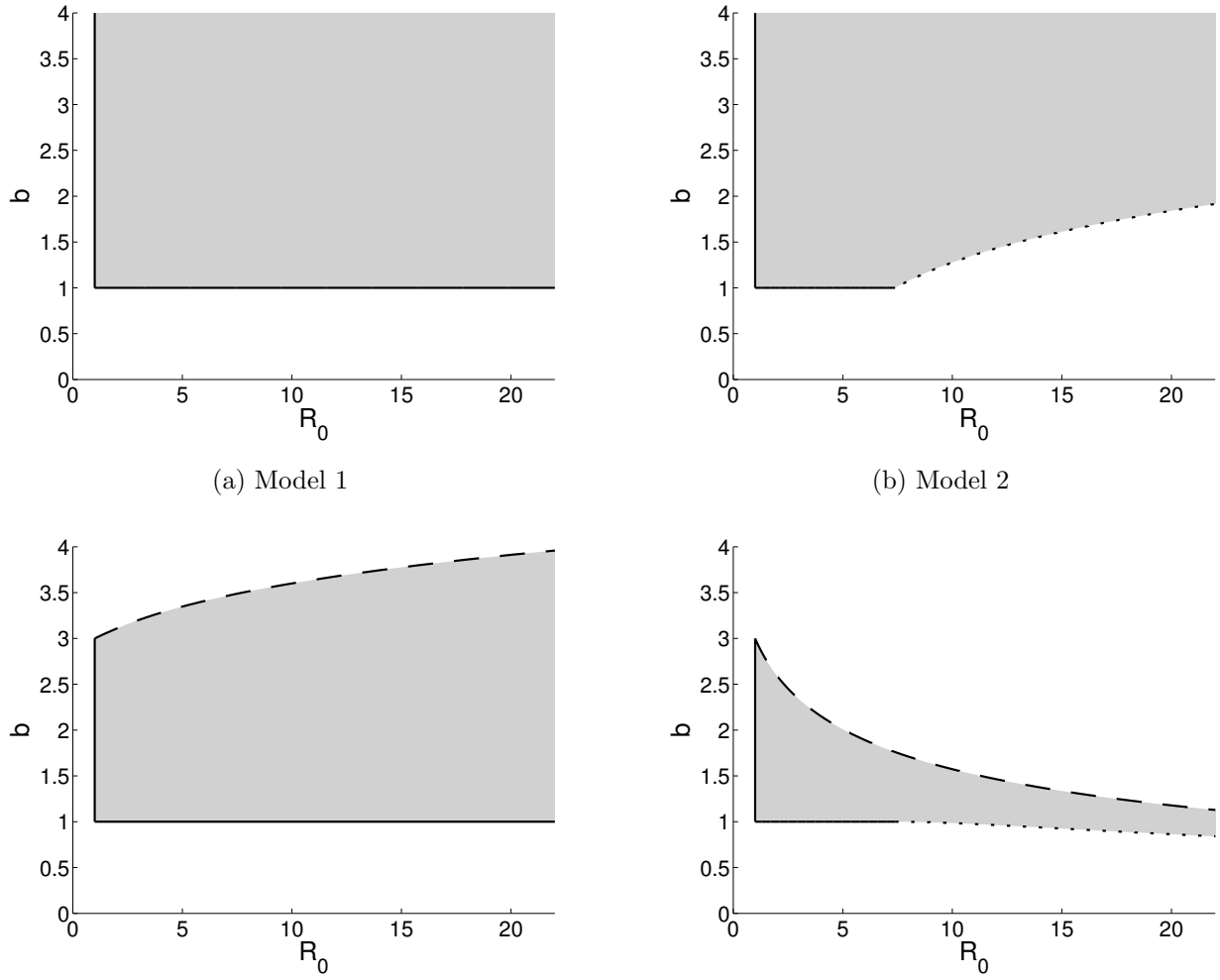

(a) Model 1

(b) Model 2

(c) Model 3

(d) Model 4

Figure 2.3: Stability regions for the positive coexistence equilibrium for Models 1–4. For $R_0 > 1$, the condition $b > 1$ ensures that the coexistence equilibrium is in the interior of the first quadrant for Models 1–3. For Model 4, the system has a unique positive coexistence equilibrium for $b > 1$. For $R_0 > e^2$, there is a region below $b = 1$ for which there are two positive coexistence equilibria. The coexistence equilibrium with the larger y coordinate is asymptotically stable in the shaded region below $b = 1$. The vertical solid lines are boundary curves where *both* the first and third Jury conditions are violated. The horizontal solid lines are boundary curves where the first Jury condition is violated. The dotted curves are the boundaries where the second Jury condition is first violated. The dashed curves are the boundaries where the third Jury condition is first violated.

The derivation of these stability criteria is shown in Sections 2.11.2–2.11.4.

The stability region for the coexistence equilibrium is shown in Figure 2.3b. Crossing the line segment, $b = 1$, $1 < R_0 < e^2$ violates the first Jury condition, resulting in a transcritical bifurcation. Crossing the line $R_0 = 1$ violates both the first and third Jury conditions. Crossing the dotted curve from the left in Figure 2.3b means that one of the real eigenvalues exceeds -1 in magnitude. This corresponds to a period-doubling or flip bifurcation. However, the stability analysis holds only in a neighborhood of the equilibrium point. We discuss below the existence of other stable phenomena for this model, including 2-cycles, 4-cycles, and invariant circles.

2.5.2 Bifurcations and attractors

For a fixed value of b as r increases, another attractor emerges. For certain values of b, there is a range of r values for which bistability is observed. We describe the behavior for various fixed b as r is increased in the specified range noting that $R_0 = \exp(r)$. This is illustrated in Figure 2.4.

- $b = 1.004, 1.1, 1.2$

  For $r < 2$, the coexistence equilibrium is stable. As r increases beyond $r = 2$, the system initially has a stable interior equilibrium, an unstable equilibrium at $(1, 0)$, and an unstable 2-cycle on the x-axis. (The alternating x values of the 2-cycle are shown for changing r values as dashed lines in Figure 2.4a with $y = 0$ as seen in Figure 2.4b). The extinction equilibrium and the two-cycle on the axis are unstable because y can increase when rare, such that the system goes to the interior equilibrium. As r increases further, the interior equilibrium undergoes a supercritical flip bifurcation giving rise to a stable 2-cycle. As r continues to increase, the 2-cycle moves towards the x-axis (the values of y go towards 0) before colliding with the unstable 2-cycle and exchanging stability as it passes into the fourth quadrant.

To summarize, for r somewhat greater than 2, the host-only system has a cycle with period 2 that the parasitoid can invade, stabilizing host dynamics. Increasing r eventually causes the host and parasitoid dynamics to become periodic, but further increasing r decreases the parasitoid density until it cannot persist. After this, the system goes back to the host-only dynamics (a 2-cycle), which are now stable. In this case and the two below, the dashed lines at the left of the x plots that become solid when crossing into the gray shaded region represent the dynamics of the host when it is alone (see Figures 2.4a, 2.4c, and 2.4e).

- $b = 1.3, 1.4$

  For r sufficiently high, the system has a stable interior equilibrium, an unstable equilibrium at $(1, 0)$, and an unstable 2-cycle on the x-axis. As r increases further, a stable 2-cycle emerges with an accompanying unstable 2-cycle in a saddle-node bifurcation of the second iterate of the mapping. Shortly thereafter, the interior equilibrium undergoes a subcritical flip bifurcation when the unstable 2-cycle in the first quadrant collides with it, and the equilibrium loses stability. For further discussion of subcritical flip bifurcations, see [68] and [99]. As r continues to increase, the stable 2-cycle moves towards the x-axis before colliding with the unstable 2-cycle on the x-axis and exchanging stability as it passes into the fourth quadrant.

- $b = 1.5$

  For r sufficiently high, the system has a stable interior equilibrium, an unstable equilibrium at $(1, 0)$, and an unstable 2-cycle on the x-axis. As r increases further, we first observe that the unstable two-cycle on the x-axis period doubles into a four-cycle. Then, a stable 2-cycle emerges in the interior of the first quadrant with an accompanying unstable 2-cycle in a saddle-node bifurcation of the second iterate of the mapping. Then, the stable 2-cycle undergoes a period doubling bifurcation such that a stable

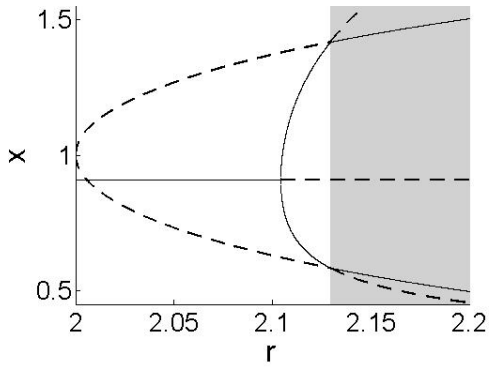

(a) $b = 1.1$

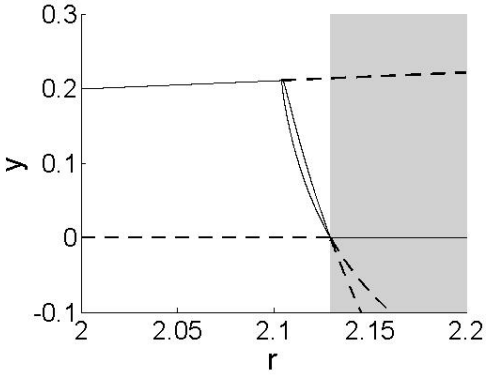

(b) $b = 1.1$

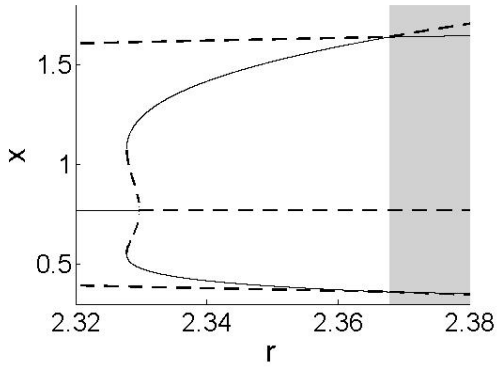

(c) $b = 1.3$

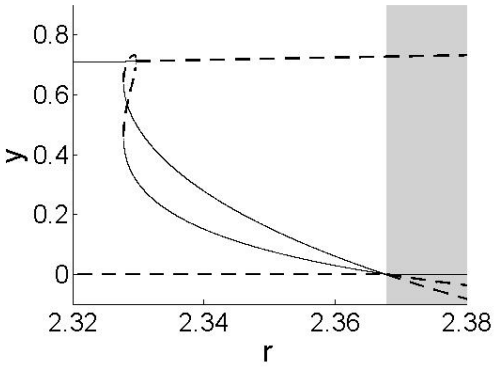

(d) $b = 1.3$

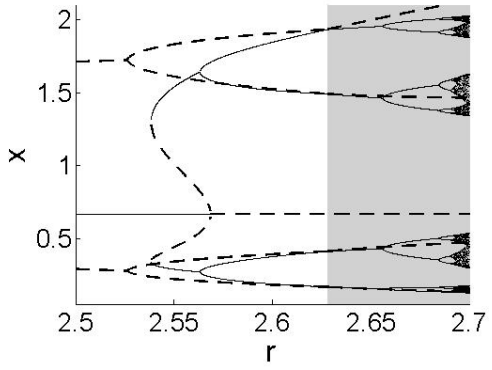

(e) $b = 1.5$

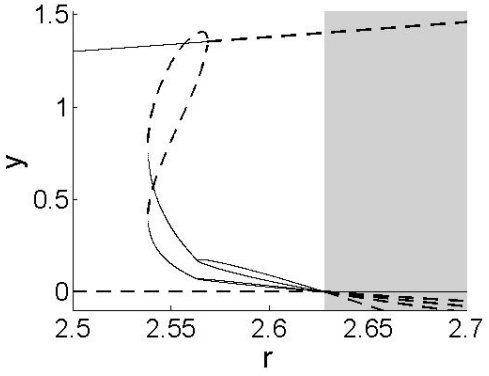

(f) $b = 1.5$

Figure 2.4: Bifurcation diagrams for Model 2 for fixed b as r increases. Figures on the left show x coordinates of stable (solid) and unstable (dashed) fixed points and cycles as r increases. Figures on the right show y coordinates of stable (solid) and unstable (dashed) fixed points and cycles as r increases. Detailed descriptions of the dynamics and bifurcations are given in the text.

4-cycle emerges. Shortly thereafter, the interior equilibrium undergoes a subcritical flip bifurcation when the unstable 2-cycle in the interior of the quadrant collides with it. After this bifurcation, the coexistence equilibrium is unstable. As r continues to increase, the stable 4-cycle moves towards the x-axis before colliding with the unstable 4-cycle and exchanging stability as it passes into the fourth quadrant.

It is evident that for higher values of b, the bifurcations associated with increasing r are more complicated. Indeed, for $b = 1.9$, $r = 2.92$, the system has an attractor with fractal dimension. A small increase in r to $r = 2.9205$ results in an attractor made up of four circles such that the union of the four circles is an invariant attractor. In both cases, the equilibrium point is locally stable with its own basin of attraction. These two cases are shown in Figure 2.5. Further increases in r result in a 4-cycle, which then period doubles into an 8-cycle.

2.6 *Model 3: Compensatory host density-dependence and exponential parasitism*

For the third model under consideration, we return to fractional recruitment, equation (2.14), and now incorporate a stronger parasitism term. That is, we now take the limit as $\kappa \to \infty$ in equation (2.8), which results in exponential parasitism seen in equation (2.10). Biologically, higher κ corresponds to lower parasitoid aggregation, detailed in [60].

The third model is

$$x_{t+1} = \left[\frac{R_0 x_t}{1 + (R_0 - 1)x_t}\right] e^{-y_t}, \tag{2.44a}$$

$$y_{t+1} = b\left[\frac{R_0 x_t}{1 + (R_0 - 1)x_t}\right] \left(1 - e^{-y_t}\right). \tag{2.44b}$$

As with the other models, the coexistence equilibrium is in the interior of the first quadrant for $R_0 > 1$, $b > 1$. This is shown in Appendix 2.12.1. For $b = 1$, the coexistence equilibrium has collided with the exclusion equilibrium at $(1, 0)$. For $R_0 = 1$, system (2.44) has a line

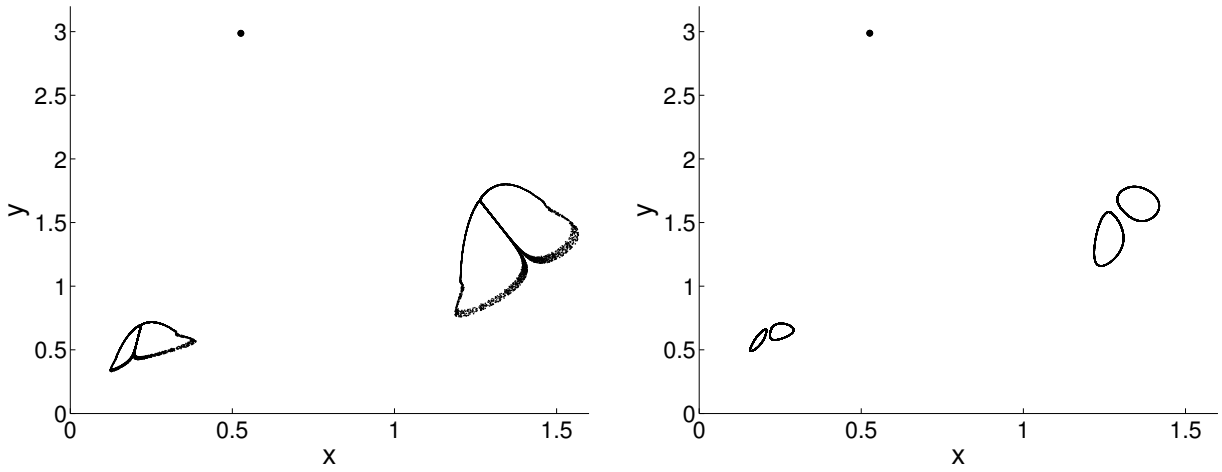

Figure 2.5: Illustration of bistability between the equilibrium and another attractor for Model 2. The parameters for the left figure are $b = 1.9,\ r = 2.92$. For the right figure, $b = 1.9,\ r = 2.9205$. For the figure on the left, the attractor is a region with fractal dimension. The attractor on the right consists of four circles such that the union of the circles is an invariant attracting set. If we continue to increase r past $r = 2.9205$, we see a 4-cycle that then period doubles to an 8-cycle. Initial conditions for both figures were $(0.8, 0.7)$ for the equilibrium and $(0.3, 0.4)$ for the other attractor. For clarity of the attractors, we ran $100,000$ iterations and plotted $30,000$ points for the attractors.

of equilibria on the x-axis. As mentioned in Section 2.3.4, we cannot derive an explicit expression for the coexistence equilibrium for models with exponential parasitism.

2.6.1 Stability region

Even without an explicit expression for the coexistence equilibrium, we can determine the stability criteria. The first Jury condition is satisfied for $R_0 > 1$, $b > 1$. Satisfying the first Jury condition is a sufficient condition for satisfying the second Jury condition. The third Jury condition, in turn, is satisfied in the R_0–b plane below the curve

$$R_0 = \frac{ye^{2y}}{e^y - 1}, \quad b = \frac{y^2e^{2y} - ye^y + y}{(e^y - 1)(ye^y - e^y + 1)}, \tag{2.45}$$

for positive y.

We determined the parametric boundary curve for the third Jury condition, inequality (2.32), by solving the three equations

$$\Delta = 1, \tag{2.46}$$

$$u(x, y) = g(x)[1 - yh(y)] = 1, \tag{2.47}$$

$$v(x, y) = bxg(x)h(y) = 1, \tag{2.48}$$

to eliminate x and write b and R_0 as functions of y. Equations (2.47) and (2.48) are the equations for the host and parasitoid nullclines given in system (2.18).

Points that satisfy equations (2.47) and (2.48) are coexistence equilibria and are technically denoted (x^*, y^*). However, when we find parametric boundary curve (2.45), the variable y functions as a parameter such that the curve is traced out in R_0–b space for a range of y values greater than zero. The resulting curve does not require actually solving for any of the coexistence equilibrium points that correspond to the (R_0, b) values on this curve. Hence, we do not use x^* or y^* notation here.

Caution is required with the method used to determine parametric curve (2.45). A curve that satisfies equations (2.46)–(2.48) is not necessarily a true boundary of the stability region;

it could be the case that $\Delta < 1$ on both sides of the curve or $\Delta > 1$ on both sides of the curve. After finding the parametric expression for the candidate boundary curve, equations (2.45), we verified numerically that the third Jury condition is satisfied below the curve and violated above the curve. Details for all three Jury conditions are given in Sections 2.12.2–2.12.4.

As shown in the stability region in Figure 2.3c, the Jury 3 condition is the interesting feature of the stability region for Model 3. Crossing the dashed curve in parameter space from below corresponds to violating the third Jury condition such that both eigenvalues leave the unit disc in the complex plane. For our model, this yields a supercritical Neimark–Sacker bifurcation [100], where the equilibrium loses stability and is replaced by a stable, quasiperiodic attractor that is topologically similar to a circle. These attractors are commonly referred to as invariant circles. The bifurcation itself is sometimes referred to as a discrete Hopf bifurcation. Crossing the line $b = 1$ violates the first Jury condition and results in a transcritical bifurcation. Crossing the line $R_0 = 1$ violates both the first and third Jury conditions.

2.6.2 Bifurcations and attractors

In order to illustrate the bifurcations and types of attractors for different parameter choices, we fix $R_0 = 2$ and increase b. Figure 2.6 shows the attractors for increasing b values. For b values below the Jury 3 curve in Figure 2.3c, the coexistence point is stable. After the Neimark–Sacker bifurcation, the complex eigenvalues of the fixed point are larger than one in magnitude, and the attractor is either a quasiperiodic invariant circle or a periodic n-cycle, increasing in size as b increases.

To verify that our system exhibits a Neimark–Sacker bifurcation when the third Jury condition is violated, we numerically computed the arguments of the eigenvalues of the system for R_0 and b parameters on the Jury 3 curve for $R_0 > 1$. In doing so, we verified that the eigenvalues do not pass through the k-th roots of unity for $k = 1, 2, 3, 4$. To guarantee

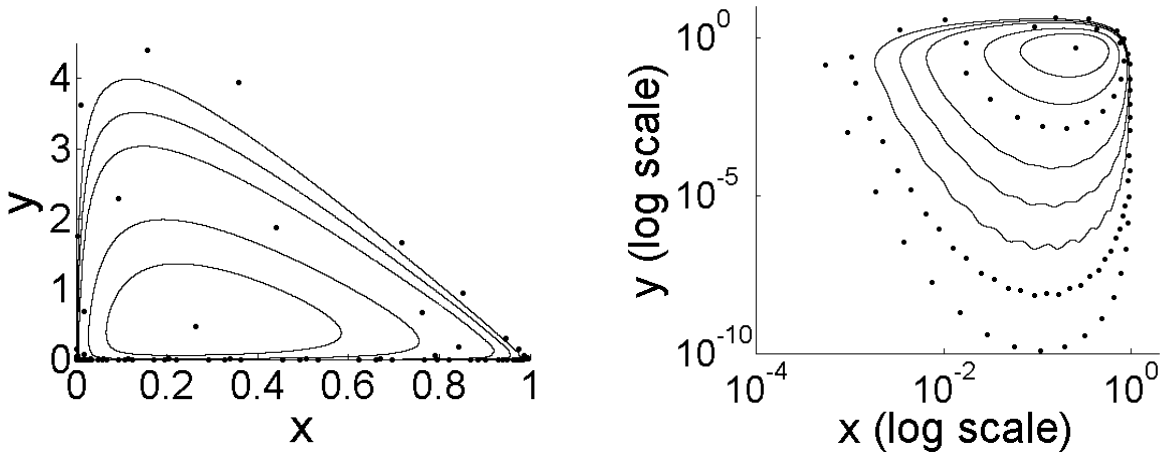

Figure 2.6: To investigate the interior attractor for Model 3, we fix $R_0 = 2$ and increase b. The value of b that produces the stable equilibrium in these figures is $b = 3$. Moving outward from this equilibrium point, the invariant circles and phase-locked cycles correspond to $b = 3.5, 4, 4.41, 5, 5.5, 6, 6.5, 7$. Crossing the boundary of the stability region results in a Neimark–Sacker bifurcation such that an invariant circle becomes the stable attractor. The invariant circle grows and undergoes phase-locking alternating with invariant circles as b continues to increase. As b increases, the lower portion of the attractor approaches the x-axis.

that an invariant circle does appear when the third Jury condition is violated, eigenvalues cannot pass through any of the first four roots of unity [99, 100].

We will now qualitatively describe the behavior of the system after the eigenvalues pass through the unit circle. For some values of b just above the Jury 3 curve, the system has a stable invariant circle. For other values of b also just above the Jury 3 curve, there is a pair of periodic orbits on the invariant circle, one stable and one unstable. When the rotation number of the periodic orbits is p/q, the system has a p/q resonance, and the stable and unstable orbits have period q [6]. The numerator of the rotation number, p, is the number of revolutions around the invariant circle that it takes for the orbit to return to the starting point of the cycle. The set of parameter values for which the system has a periodic orbit with rational rotation number p/q is known as an Arnold tongue [100].

Alternately, Arnold tongues or resonance horns may describe a cusped region in the complex plane (rather than in parameter space) where eigenvalues within the horn correspond to the existence of a stable periodic orbit with rational rotation number [6, 50, 51]. The eigenvalue will typically intersect an infinite number of these resonance horns near the unit circle [99]. In our case, as b continues to increase, the eigenvalues of the coexistence point pass in and out of resonance horns or Arnold tongues. When the eigenvalues are within a resonance horn, the system is phase-locked, and we observe a stable n-cycle in the x–y plane.

As the eigenvalues continue to grow in magnitude, the Arnold tongues are wider, and there are broader windows of phase-locking in the bifurcation diagram as the parameter b increases. Within these windows, the system may undergo period-doubling or period-halving of the cycle as the eigenvalues enter and exit overlapping resonance horns where p and q simultaneously double or are halved. For other cases with eigenvalues in overlapping resonance horns, we may expect to observe coexistence of multiple n-cycles with differing rational rotation numbers. Note that certain n-cycles may not be visible in practice if a different n-cycle dominates the system [5, 38]. Further, it is also possible in general for

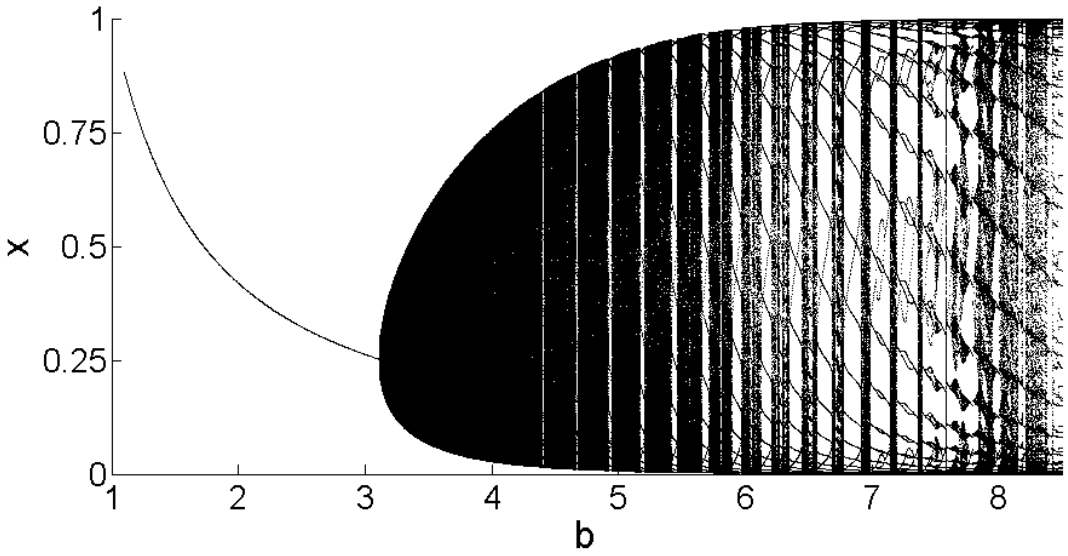

Figure 2.7: Model 3 bifurcation diagram illustrating the x coordinates of the stable attractor for $R_0 = 2$ and varying b. Note the Neimark–Sacker bifurcation that occurs when the equilibrium loses stability and an invariant circle becomes the attractor, corresponding to multiple x values for a single value of b. (Bifurcation diagram for y not shown here.)

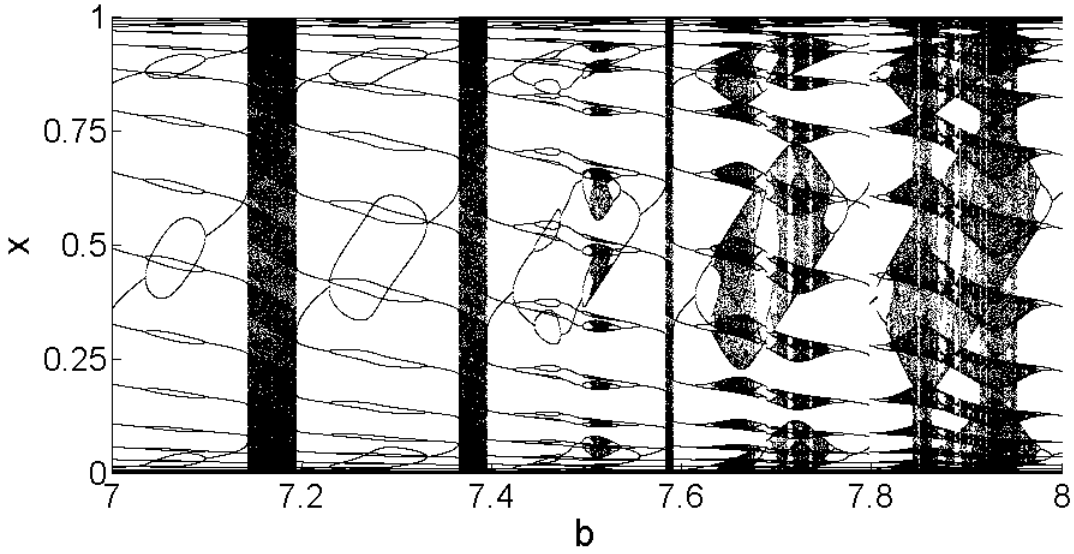

Figure 2.8: Model 3 bifurcation diagram with a narrower range of b values. As b increases, phase locking occurs along with period doubling and halving, interspersed with regions of invariant circles corresponding to a dense set of x coordinates of the attractor. These phenomena occur as the eigenvalues pass through the resonance horns corresponding to phase-locked n-cycles.

bistability to exist between a periodic cycle and some chaotic attractor as eigenvalues move further away from the unit circle. Aronson et al. [6] provide conditions for when a rotation number in a system is unique, as well as complications that may arise when there are multiple rotation numbers.

The behavior of system (2.44) as eigenvalues increase in magnitude is visible in Figures 2.7 and 2.8. These figures show bifurcation diagrams of the x coordinates of the attractors to illustrate the changes in the system as b increases for fixed $R_0 = 2$.

Returning to Figure 2.6, we note that as b increases, the stable attractor in the system grows, and the lower portion approaches the x-axis. While the interior of the first quadrant is invariant for system (2.44), numerical simulations of the system for values of b much past $b = 8.5$ cause rounding of small positive values of y down to identically 0. Thus, numerical simulations are limited in their ability to demonstrate the behavior of the system for even finite parameter values. It is ecologically likely, however, that for sufficiently small values of y, stochastic events would wipe out the parasitoid population, and the host would go to the stable equilibrium of the host-only system. However, since the host-only equilibrium can be destabilized by the introduction of parasitoids in this parameter range, an immigrating parasitoid population could invade and return the system to the complicated dynamics until another stochastic extinction event occurs.

2.7 *Model 4: Overcompensatory host density-dependence and exponential parasitism*

The fourth model uses an exponential form for both density dependence and parasitism. This corresponds to equations (2.15) and (2.17). The model is thus

$$x_{t+1} = x_t e^{r(1-x_t)} e^{-y_t}, \tag{2.49a}$$

$$y_{t+1} = b x_t e^{r(1-x_t)} \left(1 - e^{-y_t}\right). \tag{2.49b}$$

Because of the exponential parasitism term, there is not an explicit expression for the coexistence equilibria solutions to system (2.49).

Unlike the previous models, $b > 1$ is not necessary for the occurrence of a coexistence equilibrium in the interior of the first quadrant. As shown in Figure 2.3d, there is a region above $r = 2$ and below $b = 1$ for which there are two coexistence equilibria, only one of which may be stable. For $0 < r < 2$, when $b = 1$, the single coexistence equilibrium has collided with the exclusion equilibrium at $(1, 0)$. For $r = 0$ ($R_0 = 1$), system (2.49) has a line of equilibria on the x-axis.

This model was previously studied by Kang et al. [41] in the context of a plant–herbivore system. However, our nondimensionalization and methods of analysis differ from theirs. In particular, Kang et al. [41] studied stability of the equilibria numerically, while we use analytic methods. This allows us to find a bifurcation that is missing from their analysis, discussed below.

2.7.1 Stability Region

This model uses exponential forms for both density-dependent recruitment and parasitism. The stronger nonlinearity in density dependence and the stronger form of parasitism result in both the second and third Jury conditions functioning as interesting boundaries of the stability region, seen in Figure 2.3d. The stability conditions are:

1. For $0 < r < 2$, Jury condition 1 is satisfied above $b = 1$; for $r > 2$, Jury condition 1 is satisfied above the curve

$$r = \frac{y^2 e^y}{1 + y e^y - e^y}, \quad b = \frac{y^2 e^y}{(e^y - 1)^2}, \tag{2.50}$$

2. Jury condition 2 is satisfied above the curve

$$r = \frac{e^y(y^2 + 2y + 2) - 2}{e^y(y + 1) - 1}, \quad b = \frac{2y(e^y - 1) + y^2 e^y(2 + y)}{(2 + y)e^{2y} - 4e^y - y + 2}, \tag{2.51}$$

where $r \geq 2$,

3. Jury condition 3 is satisfied for $r > 0$ ($R_0 > 1$) and below the curve

$$r = \frac{e^y(y^2 + y - 1) + 1}{ye^y}, \quad b = \frac{e^y(y^3 + y^2 - y) + y}{(e^y - 1)(ye^y - e^y + 1)}. \tag{2.52}$$

The parametric curves (2.50), (2.51), and (2.52) are all defined for positive y. When $b = 1$ and $0 < r < 2$, the first Jury condition is violated. When $r = 0$ ($R_0 = 1$), the first and third Jury conditions are violated.

Details for determining all three conditions are given in Appendix 2.13.1–2.13.3. For each parametrically-defined curve, we used the equations for the host and parasitoid nullclines, equations (2.18a) and (2.18b), with either $1 - \tau + \Delta = 0$, $1 + \tau + \Delta = 0$, or $\Delta = 1$ to eliminate x and write b and r as functions of y. This process gave us candidate bifurcation curves. We then verified numerically that the relevant Jury condition is satisfied on one side of the curve and violated on the other side. Note also that we use y rather than y^*, since y functions as a parameter used to trace out a curve in r–b space.

Note that curve (2.50) is entirely below curve (2.51) (not shown). Curves (2.50) and (2.51) are visibly indistinguishable at the scale used in Figure 2.3d. For a given $r > 2$, the value of b must be above curve (2.51) for stability. The dynamics of the system for parameters between curves (2.50) and (2.51) are discussed in Section 2.7.2 below.

Returning to Figure 2.3d, we consider the bifurcations that occur when the Jury conditions are violated. Crossing the dotted curve from above violates the second Jury condition, and the system undergoes a subcritical period-doubling bifurcation. Crossing the dashed curve from below corresponds to a supercritical Neimark–Sacker bifurcation [100], where the equilibrium loses stability and is replaced by a stable, invariant circle. Crossing the solid horizontal line, $b = 1$, $0 < r < 2$ from above corresponds to a transcritical bifurcation where the unique coexistence equilibrium collides with the exclusion equilibrium on the x-axis.

While Kang et al. [41] use a different nondimensionalization, their parameter a is the same as our parameter b, the product of searching efficiency, parasitoid clutch size, and the host carrying-capacity. Thus, it holds from their work that for $b > 1$, system (2.49) has a unique coexistence equilibrium. For $r > 2$, our results indicate that above the first Jury condition curve, (2.50), and below $b = 1$, there are two coexistence equilibria. For the region above the second Jury condition curve, (2.51), below both $b = 1$ and the third Jury condition curve, (2.52), the equilibrium point with the larger y value is stable. This region extends infinitely in the r direction since the third Jury condition curve, (2.52), remains above the second Jury condition curve, (2.51), even after the curve (2.52) is below $b = 1$. See Figure 2.3d and details in Sections 2.13.1–2.13.3. The second Jury condition curve, (2.51), is the one that was missed by Kang et al. [41].

2.7.2 Bifurcations and Attractors

In order to clearly illustrate the bifurcations and dynamics of the system, we fix $r = 2.5$ ($R_0 \approx 12.18$) and increase b. We have chosen a value of r for which the second Jury condition curve is the lower boundary of the stability region, seen in Figure 2.3d. The host and parasitoid nullclines are shown in Figure 2.9 with stable and unstable equilibria and other attractors for selected values of b. A bifurcation diagram for increasing b values is shown in Figure 2.10.

For $r = 2.5$ and b below the first Jury condition curve, equation (2.50), there are no coexistence equilibria. When we increase b to the first Jury condition curve, the host and parasitoid nullclines are tangent, seen in Figure 2.9a. For slightly higher values of b, both coexistence equilibria are unstable. This differs from the claim made in Kang et al. [41] that one equilibrium is stable after the saddle-node bifurcation. However, the instability of both coexistence equilibria occurs for a tiny range of b values, from $0.959 < b < 0.961$. The upper of the two equilibria undergoes a subcritical period-doubling bifurcation and gains stability

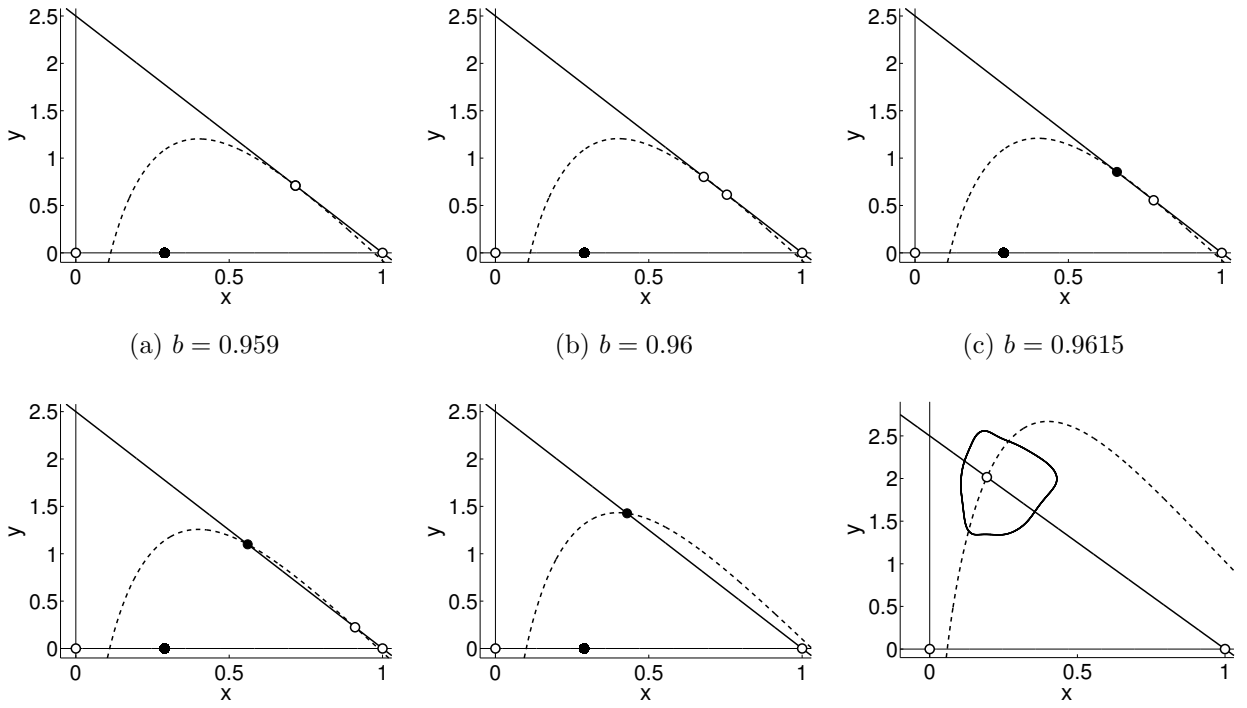

(a) $b = 0.959$ (b) $b = 0.96$ (c) $b = 0.9615$

(d) $b = 0.98$ (e) $b = 1.05$ (f) $b = 1.6$

Figure 2.9: Phase portraits for $r = 2.5$ ($R_0 \approx 12.18$) as b increases. The host nullcline is shown with the solid line. As b increases, the parasitoid nullcline, shown with a dotted line, changes shape. Attractors are shown with filled circles, while unstable equilibria are shown with open circles. (Note that the solid circle on the x-axis is one of two points that form a stable two-cycle on the axis.) At $b \approx 0.959$, a saddle-node bifurcation occurs. Note the tangency between the nullclines. This condition is equivalent to the condition for the first Jury condition to be satisfied. Both coexistence equilibria are initially unstable, but after the subcritical period-doubling bifurcation seen in Figure 2.11, the upper of the two equilibria is stable. The lower coexistence equilibrium moves towards the x-axis and collides with the exclusion equilibrium at $b = 1$. For $b > 1$, the coexistence equilibrium is unique. When the third Jury condition is violated, the coexistence equilibrium undergoes a supercritical Neimark–Sacker bifurcation. A stable quasiperiodic invariant circle becomes the attractor.

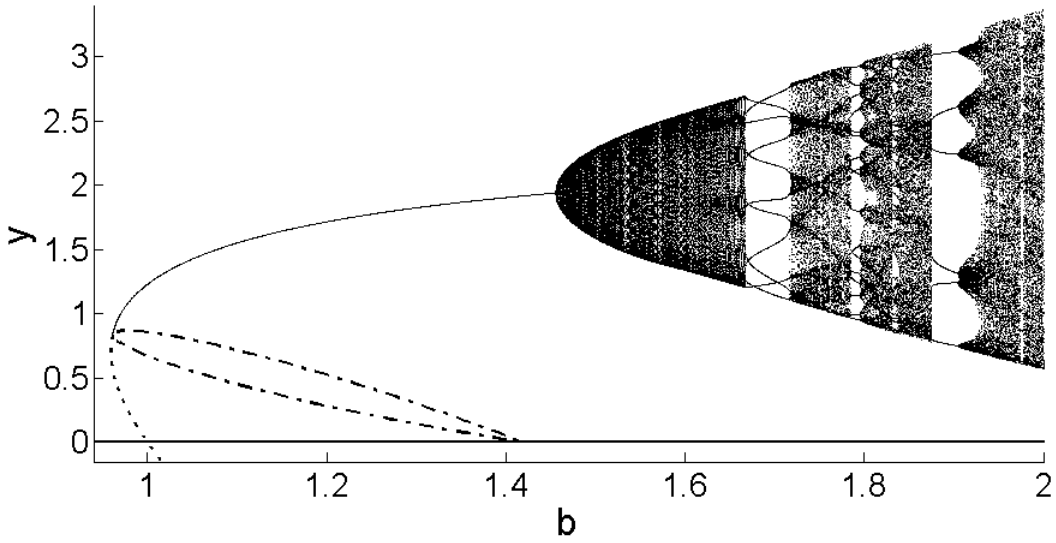

Figure 2.10: Model 4 bifurcation diagram illustrating the y coordinates of the stable attractor for $r = 2.5$ ($R_0 \approx 12.18$) and varying b. The fixed points emerge in a saddle-node bifurcation as b crosses the first Jury condition curve (2.50). The upper of the two equilibria undergoes a subcritical period-doubling bifurcation in which it becomes stable. The resulting unstable two cycle is shown with the dash-dot line. The dotted line is the unstable equilibrium, which crashes through exclusion equilibrium on the x-axis at $b = 1$. The unstable two-cycle also crashes through the x-axis. The stable equilibrium loses stability through a Neimark–Sacker bifurcation, and an invariant circle becomes the attractor, corresponding to multiple y values for a single value of b. (Bifurcation diagram for x not shown here.)

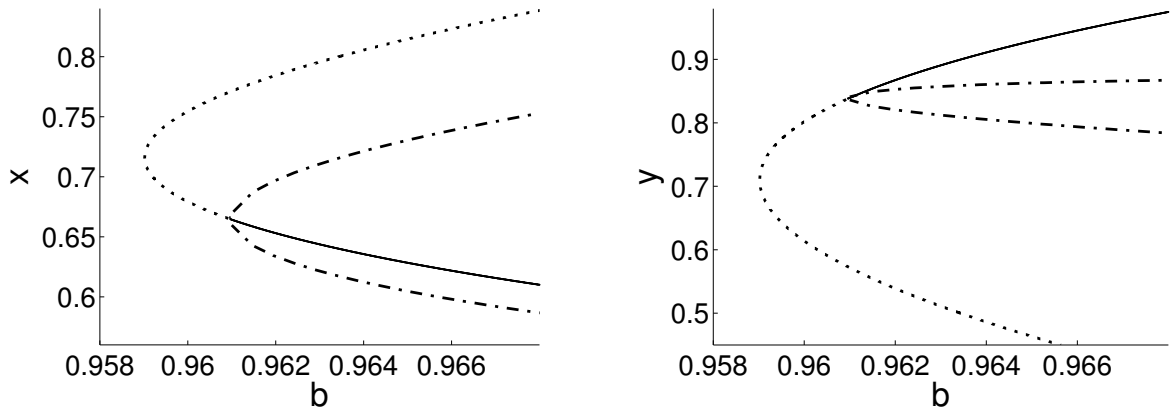

Figure 2.11: Model 4 bifurcation diagram with a much narrower range of b values, again for $r = 2.5$ ($R_0 \approx 12.18$). Here, the saddle-node bifurcation is clearly visible such that both equilibria are unstable at the lowest b values for which they exist. The left figure shows the x coordinates and the right figure shows the y coordinates for the same range of b values. Dotted lines correspond to unstable equilibria. As b increases, the equilibrium with the larger y value undergoes a subcritical period-doubling bifurcation and gains stability as an unstable two cycle is born, shown with a dash-dot line. This behavior was missed in the numerical investigations by Kang et al. [41] but can be found analytically from equations (2.50) and (2.51). The solid line corresponds to where the equilibrium with the larger y value is stable.

as b crosses the dotted curve shown in Figure 2.3d, the second Jury condition curve. The resulting unstable two-cycle was found numerically and is shown in Figures 2.10 and 2.11.

We continue with the bifurcations as b increases past $b = 1$. Returning to Figure 2.9, we see that at $b = 1$, the lower of the coexistence equilibria collides with the exclusion equilibrium as it passes into the fourth quadrant. As b continues to increase, the unstable two-cycle in the interior of the first quadrant eventually crashes through the x-axis, passing into the fourth quadrant. For sufficiently low values of b, the two-cycle on the axis is a competing stable attractor. When b crosses the third Jury condition curve, a Neimark–Sacker bifurcation results and a quasiperiodic stable invariant circle is born. As seen in Figure 2.10, the complex eigenvalues of the coexistence equilibrium point again pass in and out of Arnold tongues, resulting in phase-locking and stable n-cycles. A detailed discussion of this phenomena is in Section 2.6.2.

We note that for this model, we also see the development of a chaotic strange attractor. The collapse of the strange attractor in a crisis bifurcation is discussed by Kang et al. [41], as well as cases of more complicated bistability between boundary attractors and interior attractors. Hence, we do not discuss details here. One of the strange attractors is shown in Figure 2.12. Due to the use of a stronger nonlinearity in density dependence and stronger parasitism in Model 4, we see the greatest variability in dynamics and bifurcations in this system compared to Models 1, 2, and 3.

2.8 Discussion

We have developed a framework for investigating host–parasitoid systems where density dependence precedes parasitism in the life cycle of the host. Recall that these models have the form given in system (2.5). Our analysis addresses all combinations of the most frequently used functions for host density-dependence and parasitism. The methods used in this chapter can also be extended to models using other functional forms for recruitment and parasitism,

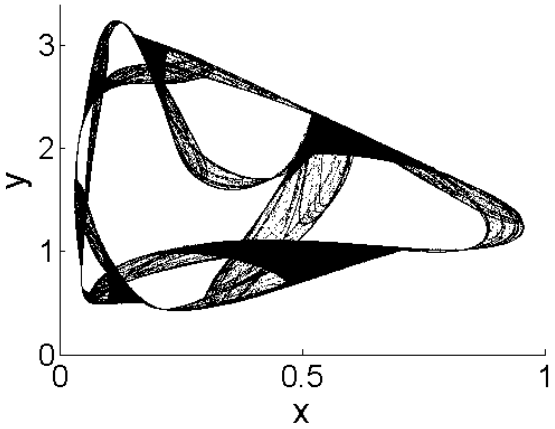

Figure 2.12: A strange attractor for Model 4 with $r = 2.3$, $b = 2.2$. Parameters chosen for aesthetic appeal of the strange attractor.

including cases where there may not be an explicit expression for the coexistence equilibria. With our analytical approach, we were able to more fully categorize the dynamics of system (2.49), Model 4, which previously had been analyzed using numerical techniques [41]. Our systematic approach allows for direct comparison of four foundational models, each based on specific biological characteristics of host and parasitoid species.

Each model resulted in different dynamics. Through systematic comparison of the models, we identified the effects of stronger parasitism (corresponding to higher κ and lower parasitoid aggregation). We then contrasted these effects with the effects of stronger nonlinearity in the density-dependence term. As expected, fractional recruitment and parasitism yield stable dynamics. Stronger parasitism in the model leads to a restricted stability region for the coexistence equilibrium, seen in Figures 2.3c and 2.3d. Both Models 3 and 4 include Neimark–Sacker bifurcations where the coexistence equilibrium is replaced with invariant circles. On the other hand, stronger nonlinearity in the density-dependence term produces period-doubling bifurcations and the potential for bistability. In the case of Model 2, the

period doubling may be supercritical or subcritical, depending on the value of b. The period-doubling bifurcation observed in Model 4 is subcritical and only occurs for sufficiently large values of r.

For models with stronger parasitism resulting from lower parasitoid aggregation (Models 3 and 4), stability of the equilibrium is lost as b increases. Since b is proportional to host carrying-capacity, K, an increase in host carrying-capacity can result in loss of stability of the equilibrium for these models, consistent with the paradox of biological enrichment [83]. For the invariant circles and n-cycles that arise after the Neimark–Sacker bifurcation, the host population remains below the carrying capacity throughout the population cycles. On the other hand, the loss of stability through increased r in Model 2 yields drastic swings in host population size above and below carrying capacity, K, with relatively short period (2, 4, etc.). In these cases, the introduction of a parasitoid species could increase the host population size above its natural carrying capacity during some years of the population cycles. In agricultural scenarios, these host outbreaks could have devastating consequences.

Future work for the models presented in this chapter requires comparison with data from host–parasitoid systems and consideration of what range of parameters are observed biologically. While we have provided a mathematical characterization of these systems, the biological implications need to be experimentally verified. As noted above, the period and amplitude of oscillations differ for the case of invariant circles arising in models with higher parasitism and the case of 2-cycles or 4-cycles arising in models with overcompensatory density-dependent effects. It would be beneficial to compare these models with data to determine if overcompensation does, in fact, lead to shorter-period, higher-amplitude oscillations in host population size in experimental systems.

In comparing with data, it is important to acknowledge environmental and demographic stochasticity, which will impact the ways that mathematically predicted n-cycles and quasi-periodic fluctuations in population size manifest in real populations. It is also important to

consider whether the models presented here can be used for prediction in specific management scenarios or whether their use is more suited to development of biological control theory. Barlow [8] provides a survey of biological control models for specific real-world systems and emphasizes the value of models in understanding specific case studies, whether or not the models are used for practical management decisions.

As discussed in Section 2.1, the sequence of events in the host life-cycle also has important impacts on the population dynamics. The models investigated in this chapter assume that density dependence precedes parasitism, which is an appropriate assumption for some species. For example, houseflies (*Musca* spp.) are attacked by pupal parasitoids such as *Spalangia* spp. and *Muscidifurax* spp. after significant density dependence in the early larval stages [61]. However, in other species, density dependence acts on the survivors of parasitism, which leads to the model

$$N_{t+1} = N_t[1 - P_t H(P_t)]G\Big(N_t[1 - P_t H(P_t)]\Big), \tag{2.53a}$$

$$P_{t+1} = cN_t P_t H(P_t). \tag{2.53b}$$

Note that this model assumes not only that parasitism occurs first in the host life-cycle, but also that the parasitized hosts are functionally dead and unable to compete. For the fractional form for recruitment and the negative binomial form for parasitism, this model can lead to stable equilibria with hosts at a higher level than their carrying capacity in the absence of parasitoids [61, 62].

Systems (2.53) and (2.5) represent the scenarios where parasitism occurs either before or after density-dependent effects on the host, and May et al. [61] compared some specific models in these frameworks. However, more complicated parasitoid phenologies exist in nature. Cobbold et al. [19] explicitly consider koinobiont parasitoids, which do not kill their host immediately. This means that there is a period of time when parasitized hosts are competing with nonparasitized hosts, which cannot be accounted for with either system (2.53) or system (2.5). Cobbold et al. [19] found that the delayed mortality of parasitized

hosts may have implications for biological control. Differences in the timing of interaction between parasitoids and hosts lead to different predicted population dynamics. Thus, model formulation requires care and awareness of biological assumptions that are inherent to the structure of a model.

Host–parasitoid models have numerous avenues for the inclusion of additional biological complexities such as spatial heterogeneity, Allee effects, and multiple parasitoid species. In building towards these more biologically realistic models, it is important to understand the dynamics of simpler models, such as those analyzed and compared here. Hassell [32, 33] has done excellent work in bridging the gap between simple mechanistic models for host–parasitoid systems and models for more complex and biologically realistic systems. Extending simple mechanistic models to investigate more complicated scenarios can only occur when the simple foundational models are well-understood and presented with explicit acknowledgment of biological assumptions.

Biological differences between models may be critical to communicate well with ecologists and experimentalists. We therefore urge researchers to exercise caution in formulation of models and underlying biological assumptions in order to promote communication and broader understanding of mathematical and theoretical findings.

2.9 Appendix A: Partial Derivatives for Jury Conditions

We begin by evaluating the partial derivatives that appear in the Jury conditions. From the definitions of $u(x, y)$ and $v(x, y)$, equations (2.12) and (2.13), we obtain the partial derivatives

$$u_x = g'(x)[1 - yh(y)], \tag{2.54}$$

$$u_y = g(x)[1 - yh(y)]', \tag{2.55}$$

$$v_x = b[g(x) + xg'(x)]h(y), \tag{2.56}$$

$$v_y = bxg(x)h'(y). \tag{2.57}$$

For Models 1 and 2, with fractional parasitism (2.16), we use

$$h(y) = \frac{1}{1+y} = 1 - yh(y). \tag{2.58}$$

Recall that Models 3 and 4 have exponential parasitism, given by equation (2.17). Furthermore, Models 1 and 3 use fractional per-capita-recruitment, with $g(x)$ defined in equation (2.14), while Models 2 and 4 use exponential per-capita-recruitment, with $g(x)$ defined in equation (2.15). To simplify expressions for the partial derivatives for each model using the corresponding functions for $g(x)$ and $h(y)$, we also use the nullcline equations, $u(x^*, y^*) = 1$ and $v(x^*, y^*) = 1$. The resulting expressions for the partial derivatives are given in Table 2.1.

2.10 Appendix B: Model 1 stability calculations

2.10.1 Requirements for existence of coexistence equilibrium in the first quadrant

We now determine the conditions that ensure an equilibrium in the interior of the first quadrant. For this model, we can explicitly solve system (2.18) for the coexistence equilibrium,

$$(x^*, y^*) = \left(\frac{1}{b}, g\left(\frac{1}{b}\right) - 1\right). \tag{2.59}$$

The x coordinate is positive for all positive b. The y coordinate is positive when

$$g\left(\frac{1}{b}\right) - 1 = \frac{R_0}{1 + (R_0 - 1)\left(\frac{1}{b}\right)} - 1 > 0, \tag{2.60}$$

which simplifies to $b > 1$ since we assume $R_0 > 1$. Thus, the coexistence equilibrium exists and is in the first quadrant when $R_0 > 1, b > 1$.

2.10.2 First Jury condition

For $b > 1$, $R_0 > 1$, the x and y coordinates of the coexistence equilibrium are positive. We thus use partial derivatives from Table 2.1 to write inequality (2.36), as

$$u_x v_y - u_y v_x = \left(\frac{R_0 - 1}{R_0}\right) g(x^*)h(y^*) + h(y^*)\left[\frac{1}{R_0 x^*} g(x^*)\right] > 0. \tag{2.61}$$

Table 2.1: Partial derivatives used to apply the Jury conditions to the coexistence equilibrium point(s) for each model.

	Model 1	Model 2	Model 3	Model 4
u_x	$\frac{(1-R_0)}{R_0}g(x^*)$	$-r$	$\frac{(1-R_0)}{R_0}g(x^*)$	$-r$
u_y	$-h(y^*)$	$-h(y^*)$	-1	-1
v_x	$\frac{1}{R_0x^*}g(x^*)$	$\frac{1}{x^*}-r$	$\frac{1}{R_0x^*}g(x^*)$	$\frac{1}{x^*}-r$
v_y	$-h(y^*)$	$-h(y^*)$	$\frac{1}{y^*h(y^*)}[1-y^*h(y^*)-h(y^*)]$	$\frac{1}{y^*h(y^*)}[1-y^*h(y^*)-h(y^*)]$

We now substitute in the expression for $g(x^*)$ from equation (2.14) and simplify on the left-hand side to get

$$\frac{h(y^*)}{x^*} > 0. \tag{2.62}$$

Since $h(y^*)$ is positive, the first Jury condition is satisfied whenever the coexistence equilibrium is in the first quadrant.

When $b = 1$, the y-coefficient from equation (2.59) is $y^* = 0$, and the first Jury condition, inequality (2.35) is violated. When $R_0 = 1$, equation (2.59) again gives us $y^* = 0$, regardless of the value of b, such that the x-axis is a line of equilibrium points. For $R_0 = 1$, the first Jury condition, inequality (2.35) is again violated.

2.10.3 Second Jury condition

Recall that the second Jury condition, inequality (2.31), is

$$1 + \tau + \Delta > 0. \tag{2.63}$$

For this model, we will not show this directly. Instead, note that if $\tau > 0$ and $1 - \tau + \Delta > 0$, which is the first Jury condition, then $1 + \tau + \Delta > 1 - \tau + \Delta > 0$. This means $\tau > 0$ and the satisfaction of the first Jury condition are sufficient criteria for the second Jury condition.

The first Jury condition is satisfied for $b > 1, R_0 > 1$. We will show that in this case, the second Jury condition will also be satisfied. We proceed by showing that $\tau > 0$ at the equilibrium. As seen in equation (2.33), $\tau = 2 + x^* u_x + y^* v_y$. We use the expressions for u_x and v_y from Table 2.1 and the definitions of $g(x)$ and $h(y)$ from equations (2.14) and (2.16) to express the trace,

$$\tau = 2 - \frac{R_0 - 1}{R_0} x^* g(x^*) - y^* h(y^*) = 2 - \left[\frac{(R_0 - 1)x^*}{1 + (R_0 - 1)x^*} + \frac{y^*}{1 + y^*} \right]. \tag{2.64}$$

We thus seek to show that

$$2 > \frac{(R_0 - 1)x^*}{1 + (R_0 - 1)x^*} + \frac{y^*}{1 + y^*} \tag{2.65}$$

for $x^*, y^* > 0$, $R_0 > 1$.

Both of the terms on the right-hand side of inequality (2.65) are of the form $z(1+z)^{-1}$, where z is positive. Each term individually is less than one because $z < 1+z$, which indicates that $z(1+z)^{-1} < 1$ for positive z. Therefore,

$$\tau = 2 - \left[\frac{(R_0-1)x^*}{1+(R_0-1)x^*} + \frac{y^*}{1+y^*}\right] > 0. \tag{2.66}$$

It follows that the first Jury condition is a sufficient condition for the second Jury condition for Model 1.

For either $b = 1$ or $R_0 = 1$, we can directly calculate the terms in the second Jury condition, inequality (2.31). Direct calculation verifies that the second Jury condition is satisfied.

2.10.4 Third Jury condition

Recall that the third Jury condition is $\Delta < 1$. The determinant is given in terms of the partial derivatives in equation (2.34). Using the expressions for u_x, u_y, v_x, and v_y from Table 2.1, the third Jury condition simplifies to

$$1 + \frac{(1-R_0)}{R_0} x^* g(x^*) < 1. \tag{2.67}$$

When we use equation (2.14) for $g(x^*)$, the condition can be expressed as

$$1 - \frac{(R_0-1)x^*}{1+(R_0-1)x^*} < 1, \tag{2.68}$$

which simplifies to

$$1 + (R_0-1)x^* > 1. \tag{2.69}$$

This is true for $R_0 > 1$ for the equilibrium in the interior of the first quadrant. Thus, the third Jury condition is satisfied for $R_0 > 1$. For $R_0 = 1$, the third Jury condition is violated.

2.11 Appendix C: Model 2 stability calculations

2.11.1 Requirements for existence of coexistence equilibrium in the first quadrant

For this model, we can again explicitly solve system (2.18) for the coexistence equilibrium for Model 2,

$$(x^*, y^*) = \left(\frac{1}{b}, e^{r(1-1/b)} - 1\right). \tag{2.70}$$

When $b = 1$, this equilibrium point is on the x-axis at $(x^*, y^*) = (1, 0)$, which is the exclusion equilibrium. For the coexistence equilibrium to be in the interior of the first quadrant, it is necessary that

$$y^* = e^{r(1-1/b)} - 1 > 0. \tag{2.71}$$

For $r > 0$, this requires $b > 1$. Note that we will not consider the case $r < 0$, $b < 1$ since we are interested in cases where the host species persists in the absence of the parasitoid.

2.11.2 First Jury condition: slopes of zero-growth isoclines

Using partial derivatives from Table 2.1, the first Jury condition, inequality (2.35), is

$$x^* y^* \left[r h(y^*) + h(y^*) \left(\frac{1}{x^*} - r \right) \right] = y^* h(y^*) > 0. \tag{2.72}$$

Because $y^* h(y^*)$ is positive for the coexistence equilibrium, this inequality holds for the equilibrium in the interior of the first quadrant. When $b = 1$, $y^* h(y^*) = 0$, and the first Jury condition is violated. For $r = 0$, the x-axis is a line of equilibrium points, and the first Jury condition is again violated.

2.11.3 Second Jury Condition

Again using partial derivatives from Table 2.1, the second Jury condition, inequality (2.37) simplifies to

$$4 - 2x^* r - y^* h(y^*) = 4 - 2xr - \frac{y^*}{1 + y^*} > 0. \tag{2.73}$$

The coordinates of the coexistence equilibrium point are given by equation (2.70). Using these values, the stability condition is

$$3 - \frac{2}{b}r + e^{\left(\frac{r}{b} - r\right)} > 0. \tag{2.74}$$

We now consider the transcendental equation,

$$3 - \frac{2}{b}r + e^{\left(\frac{r}{b} - r\right)} = 0, \tag{2.75}$$

and introduce the parameter $\omega = r/b$ so that

$$3 - 2\omega + e^{\omega - r} = 0. \tag{2.76}$$

We solve for r as a function of ω,

$$r = \omega - \ln\left(2\omega - 3\right), \tag{2.77}$$

and can then also write b as a function of ω,

$$b = \frac{r}{\omega} = 1 - \frac{1}{\omega}\ln\left(2\omega - 3\right). \tag{2.78}$$

For $\omega > 3/2$, equations (2.77) and (2.78) express the boundary of the region in parameter space where the coexistence equilibrium satisfies the second Jury condition. The point $(r, b) = (2, 1)$ is where the Jury 2 curve intersects the $b = 1$ line, seen in Figure 2.3b. The portion of the curve shown in Figure 2.3b corresponds to $3/2 < \omega < 2$. We numerically verified that the second Jury condition is satisfied above this curve and violated directly below it. (The portion of the curve defined by $\omega > 2$ corresponds to $b < 1$, such that there is no coexistence equilibrium in the interior of the first quadrant.) For $b = 1$, inequality (2.74) requires $r < 2$.

2.11.4 Third Jury Condition

The expression for the determinant from equation (2.34) for this model simplies significantly to

$$\Delta = 1 - rx^*, \tag{2.79}$$

using the partial derivatives in Table 2.1. Since $x^* = 1/b$, the third Jury condition is

$$1 - \frac{r}{b} < 1. \tag{2.80}$$

Since $b > 0$ and we assumed $r \geq 0$, this inequality is satisfied for $r > 0$. When $r = 0$, the third Jury condition is violated.

2.12 Appendix D: Model 3 stability calculations

2.12.1 Requirements for existence of coexistence equilibrium in first quadrant

As was true in Section 2.10.1, we seek to determine the conditions that ensure that an equilibrium exists in the interior of the first quadrant, this time for Model 3, system (2.44). The coexistence equilibrium cannot be solved for explicitly in this case, so we instead consider the nullclines.

Equation (2.18a) is the host nullcline with intercepts $(0, \ln R_0)$ and $(1, 0)$. To obtain the slope of this nullcline in the x–y plane, we first differentiate $u(x, y) = 1$ with respect to x and get

$$u_x + u_y \frac{dy}{dx} = 0. \tag{2.81}$$

The slope of the host nullcline is

$$\frac{dy}{dx} = -\frac{u_x}{u_y} = \frac{1 - R_0}{R_0} g(x), \tag{2.82}$$

using the expressions for u_x and u_y from Table 2.1. Since $g(x) > 0$ and we assume $R_0 > 1$, the host nullcline is monotone decreasing in the first quadrant from $(0, \ln R_0)$ to $(1, 0)$.

We now consider the parasitoid nullcline, equation (2.18b). To find the slope in the x-y plane, we differentiate $v(x, y) = 1$ with respect to x to get

$$v_x + v_y \frac{dy}{dx} = 0. \tag{2.83}$$

The slope for the parasitoid nullcline is thus

$$\frac{dy}{dx} = \frac{-v_x}{v_y} = -\frac{g(x)}{R_0 x v_y}. \tag{2.84}$$

Since $g(x) > 0$, the sign of v_y will determine the sign of the slope of the parasitoid nullcline. Negative v_y will indicate that the slope of the nullcline is positive.

We substitute $h(y)$ from equation (2.17) into v_y for Model 3, such that

$$v_y = \frac{1}{1-e^{-y}}\left[e^{-y} - \frac{1}{y}\left(1-e^{-y}\right)\right] = \frac{1}{y\left(1-e^{-y}\right)}\left(ye^{-y} - 1 + e^{-y}\right). \tag{2.85}$$

The denominator is positive for $y > 0$, so we consider the numerator. For $y > 0$,

$$1 + y < e^y, \tag{2.86a}$$

$$(1+y)e^{-y} < 1, \tag{2.86b}$$

$$e^{-y} + ye^{-y} - 1 < 0. \tag{2.86c}$$

Thus, we conclude that $v_y < 0$ for $y > 0$. This means that the slope of the parasitoid nullcline is positive in the first quadrant. If there is an intersection of the host and parasitoid nullclines in the first-quadrant, it is unique.

To determine existence of the equilibrium, we examine the the x- and y-intercepts of the parasitoid nullcline,

$$1 = \frac{bxR_0h(y)}{1 + (R_0 - 1)x}. \tag{2.87}$$

After solving for x, we obtain

$$x = \frac{1}{bR_0h(y) + (1 - R_0)}, \tag{2.88}$$

where

$$h(y) = \frac{1}{y}\left(1 - e^{-y}\right). \tag{2.89}$$

To examine equation (2.88), we consider the limiting behavior of $h(y)$ as $y \to -\infty$,

$$\lim_{y\to-\infty} h(y) = \lim_{z\to\infty} h(-z) = \lim_{z\to\infty} \frac{-1}{z}\left(1 - e^{z}\right) = \infty. \tag{2.90}$$

Thus, if we consider the limit as $y \to -\infty$ in equation (2.88), $x \to 0^+$. This nullcline does not have a y-intercept because as $x \to 0^+$, $y \to -\infty$.

Since we know that in the first quadrant, the parasitoid nullcline is monotone increasing and the host nullcline has x-intercept at $x = 1$, we need to find the conditions for which the parasitoid nullcline's x-intercept lies between 0 and 1. For these conditions, there exists exactly one intersection of the parasitoid and host nullclines in the interior of the first quadrant. The x-intercept of the parasitoid nullcline is the solution to

$$1 = bxg(x)h(0) = \frac{bxR_0}{1 + (R_0 - 1)x}, \tag{2.91}$$

which is

$$x_{\text{int}} = \frac{1}{R_0(b-1) + 1}. \tag{2.92}$$

We seek the conditions for which

$$0 < \frac{1}{R_0(b-1) + 1} < 1. \tag{2.93}$$

This translates into the following two criteria,

$$R_0(b-1) + 1 > 0, \tag{2.94}$$

and

$$R_0(b-1) + 1 > 1, \tag{2.95}$$

which can be consolidated as

$$\begin{aligned} R_0(b-1) + 1 &> 1, \\ R_0(b-1) &> 0. \end{aligned} \tag{2.96}$$

This is true when $b > 1$. So the x-intercept of the parasitoid nullcline occurs between 0 and 1 if and only if $b > 1$.

We conclude that there is exactly one equilibrium point in the interior of the first quadrant if and only if $b > 1$. When $b > 1$, we can then determine if the coexistence equilibrium is stable. For $b = 1$, the equilibrium point is on the boundary of the first quadrant, at $(1, 0)$. For $R_0 > 1$, $b < 1$, there are no equilibria points in the interior of the first quadrant.

2.12.2 First Jury condition

For $b > 1$, $R_0 > 1$, the x and y coordinates of the coexistence equilibrium are positive. We thus use partial derivatives from Table 2.1 to write the first Jury condition, inequality (2.35), as

$$x^*y^*(u_xv_y - u_yv_x) = x^*y^*\left[\frac{1 - R_0}{R_0}g(x^*)v_y + \frac{1}{R_0x^*}g(x^*)\right] > 0, \tag{2.97}$$

which simplifies to

$$\frac{1}{R_0x^*}g(x^*) > \frac{R_0 - 1}{R_0}g(x^*)v_y. \tag{2.98}$$

The left-hand side of inequality (2.98) is positive, while the right-hand side is negative for $R_0 > 1$, since v_y was shown to be negative in Section 2.12.1. Thus, this inequality holds for the positive coexistence equilibrium.

When $b = 1$, the coexistence equilibrium has collided with the exclusion equilibrium at $(1, 0)$. Since the y coordinate is 0, the first Jury condition, inequality (2.35), is violated. When $R_0 = 1$, any point on the x-axis is a solution to system (2.44). Since these equilibria points have $y = 0$, the first Jury condition is violated for this line of equilibrium points.

2.12.3 Second Jury condition

We will use the technique from Section 2.10.3 to show that the first Jury condition is a sufficient condition for the second Jury condition. To do this, we must show that $\tau > 0$ at the interior equilibrium. As seen in equation (2.33), $\tau = 2 + x^*u_x + y^*v_y$. We use the

expressions for u_x and v_y from Table 2.1 and the definitions of $g(x)$ and $h(y)$ from equations (2.14) and (2.17) to get

$$\tau = 1 - \left[\frac{(R_0 - 1)x^*}{1 + (R_0 - 1)x^*}\right] + \frac{y^* e^{-y^*}}{1 - e^{-y^*}}, \tag{2.99}$$

after simplification.

For positive y^*, the last term is positive. Similarly to Section 2.10.3, the middle term is of the form $z(1+z)^{-1}$, where z is positive. For $R_0 > 1$, this term individually is less than one because $z < 1 + z$, which indicates that $z(1 + z)^{-1} < 1$ for positive z. Since the coordinates of the coexistence equilibrium are positive for $b > 1$, $R_0 > 1$, we conclude that $\tau > 0$ for $b > 1$ and $R_0 > 1$. It follows that the first Jury condition is a sufficient condition for the second Jury condition.

For either $b = 1$ or $R_0 = 1$, we can directly calculate the terms in the second Jury condition, inequality (2.31). Direct calculation verifies that the second Jury condition is satisfied in these cases.

2.12.4 Third Jury condition

The third Jury condition is $\Delta < 1$. The determinant is given in terms of the partial derivatives in equation (2.34). Using the expressions for u_x, u_y, v_x, and v_y from Table 2.1 and much algebraic simplification, the third Jury condition is

$$\Delta = \frac{g(x^*)}{R_0 h(y^*)} < 1. \tag{2.100}$$

We want to write the condition solely in terms of the parameters, R_0 and b, and find the curve in the R_0–b plane where stability changes. Because of the transcendental nature of the inequality, we will express this curve parametrically with R_0 and b as functions of y. (As explained in Section 2.6.1, we do not use x^* and y^* here since y will function as a parameter, rather than the y-coordinate value of a particular coexistence equilibrium.)

We first consider

$$1 = \frac{g(x)}{R_0 h(y)} = \frac{1}{h(y)\left[1 + (R_0 - 1)x\right]}, \tag{2.101}$$

and solve for x,

$$x = \left(\frac{1}{R_0 - 1}\right)\left[\frac{1 - h(y)}{h(y)}\right]. \tag{2.102}$$

We now incorporate the host nullcline, equation (2.18a), which is valid at the equilibrium point. Using $g(x) = R_0 h(y)$ from equation (2.101), we get

$$1 = g(x)[1 - yh(y)] = R_0 h(y)[1 - yh(y)]. \tag{2.103}$$

Solving for R_0 as a function of y yields

$$R_0 = \frac{1}{h(y)[1 - yh(y)]}. \tag{2.104}$$

Next, we need an expression for b as a function of y. To do this, we incorporate the parasitoid nullcline, equation (2.18b), which is valid at the equilibrium point. Starting with equation (2.18b), we replace x with the expression from (2.102) and also substitute $R_0 h(y)$ for $g(x)$, using the determinant condition (2.101). This gives us the equation,

$$1 = bxg(x)h(y) = \frac{b}{R_0 - 1}\left[\frac{1 - h(y)}{h(y)}\right] R_0 h(y)h(y). \tag{2.105}$$

We solve for b to get

$$b = \left(\frac{R_0 - 1}{R_0}\right)\frac{1}{h(y)\left[1 - h(y)\right]}. \tag{2.106}$$

We then eliminate the dependence on R_0 from the equation for b. This gives us b as a function of y,

$$b = \frac{1 - h(y)[1 - yh(y)]}{h(y)[1 - h(y)]}, \tag{2.107}$$

which does not simplify in a meaningful way. This equation combined with equation (2.104) expresses the boundary of the region in parameter space where the coexistence equilibrium

satisfies the third Jury condition. We numerically verified that the third Jury condition is satisfied above this curve and violated below the curve.

When $R_0 = 1$, the x-axis is a line of equilibrium points, as stated in Section 2.12.2. Under these conditions, the expression for the determinant simplifies to $\Delta = 1$, and so the third Jury condition is also violated for $R_0 = 1$.

2.13 Appendix E: Model 4 stability calculations

From Section 2.7, recall that there may be one or two coexistence equilibria, depending on the parameter values. In the case of two coexistence equilibria, only the point with the larger y value may be stable, as discussed in Section 2.7.1. The analysis here pertains to the stability of the single unique coexistence equilibrium or the coexistence equilibrium point with the larger y value.

As Kang et al. [41] proved, for $b > 1$, system (2.49) has a unique positive equilibrium. For $b = 1$, $0 < r < 2$, the point $(1, 0)$ is an equilibrium point, and there is no coexistence equilibrium in the interior of the first quadrant. For $r > 2$ and b just less than 1, the system has both a stable coexistence equilibrium point and an unstable coexistence equilibrium point, as seen in Figure 2.9d. For $r > 2$ and $b = 1$, the unstable coexistence point collides with the exclusion equilibrium, $(1, 0)$. This is all consistent with the analysis in Kang et al. [41]. However, for $r > 2$, there is also a narrow range of b for which the system has two unstable coexistence equilibria, as in Figure 2.9b.

2.13.1 First Jury condition

For $b > 1$, $r > 0$, the x and y coordinates of the coexistence equilibrium are positive. Using partial derivatives from Table 2.1, the first Jury condition, inequality (2.35), is

$$x^* y^* \left\{ -r \left[\frac{1}{y^* h(y^*)} \right] [1 - y^* h(y^*) - h(y^*)] + \frac{1}{x^*} - r \right\} > 0, \tag{2.108}$$

which simplifies to

$$r\left(\frac{e^{y^*}-1-y^*e^{y^*}}{y^*e^{y^*}-y^*}\right)+\frac{1}{x^*}>0, \tag{2.109}$$

using equation (2.17) for $h(y^*)$. We want to write the condition solely in terms of the parameters, r and b, and find the curve in the r-b plane where stability changes. Because of the transcendental nature of the inequality, we will write this curve parametrically with r and b as functions of y. To do so, we first consider

$$r\left(\frac{e^{y}-1-ye^{y}}{ye^{y}-y}\right)+\frac{1}{x}=0, \tag{2.110}$$

where we use x and y rather than x^* and y^* as in Appendix 2.12.4.

We now incorporate the host and parasitoid nullclines, equations (2.18a) and (2.18b). For Model 4, these equations simplify to

$$r-rx-y=0, \tag{2.111}$$

and

$$bxe^{r-rx}\,\frac{1}{y}\left(1-e^{-y}\right)=1. \tag{2.112}$$

Using equation (2.111), we now eliminate x from equation (2.110) and write r as a function of y, which simplifies to

$$r=\frac{y^2e^{y}}{1+ye^{y}-e^{y}}. \tag{2.113}$$

We now return to equation (2.112) and again eliminate x. We can then write b as a function of y, using equation (2.113) to eliminate r. After algebraic simplification, we obtain

$$b=\frac{y^2e^{y}}{(e^{y}-1)^2}. \tag{2.114}$$

Equations (2.113) and (2.114) give the boundary of the region in parameter space where the coexistence equilibrium satisfies the first Jury condition. We numerically verified that the

first Jury condition is satisfied above this curve and violated below it. Since this curve is just barely below the curve for the second Jury condition found in Section 2.13.2, this curve does not contribute to the stability region shown in Figure 2.3d.

Now consider $b = 1$ with $0 < r < 2$. As discussed previously, there is no equilibrium in the interior of the first quadrant for this case because the coexistence equilibrium has collided with the exclusion equilibrium point at $(1, 0)$. Since $y = 0$, the first Jury condition is violated for $b = 1$, $0 < r < 2$. Note also that when we take the limit as $y \to 0$ for equations (2.113) and (2.114), we obtain $(r, b) = (2, 1)$. This means that the first Jury condition curve described by equations (2.113) and (2.114) connects to the first Jury condition curve given by $b = 1$, $0 < r < 2$. Finally, when $r = 0$, system (2.49) has a line of equilibria on the x-axis. Since each of these equilibrium points has $y = 0$, the first Jury curve is violated for $r = 0$.

2.13.2 Second Jury Condition

We use partial derivatives from Table 2.1 and equation (2.17) to write the second Jury condition, inequality (2.37), as

$$4 - 2rx^* + 2y^* \left[\frac{y^* - e^{y^*} + 1}{y^*(e^{y^*} - 1)}\right] + x^*y^* \left[\frac{-r(y^* - e^{y^*} + 1)}{y^*(e^{y^*} - 1)}\right] - x^*y^* \left[-1\left(\frac{1}{x^*} - r\right)\right] > 0. \tag{2.115}$$

Our goal is now to determine a curve in parameter space where stability changes. We re-write inequality (2.115) as a equality and eliminate x using the expression from the host nullcline given in equation (2.111). When we simplify and solve for r, we obtain

$$r = \frac{2e^y - 2 + 2ye^y + y^2e^y}{e^y - 1 + ye^y}, \tag{2.116}$$

where $y > 0$ functions as a parameter.

To get b as a function of y, we first use equation (2.111) to eliminate x from the parasitoid nullcline, equation (2.112). Then, we use equation (2.116) to eliminate r. We solve for b and

obtain

$$b = \frac{2y(e^y - 1) + y^2 e^y (2 + y)}{(2 + y)e^{2y} - 4e^y + 2 - y}, \tag{2.117}$$

where $y > 0$.

Equations (2.116) and (2.117) give the boundary of the region in parameter space where the coexistence equilibrium satisfies the second Jury condition. Note that when we take the limit as $y \to 0$ for equations (2.116) and (2.117), we obtain $(r, b) = (2, 1)$. For $b = 1$, inequality (2.115) requires $r < 2$. The point $(r, b) = (2, 1)$ is where the Jury 2 curve intersects the $b = 1$ line. Thus, at the point $(r, b) = (2, 1)$, the second Jury curve given parametrically by equations (2.116) and (2.117) intersects the first Jury curve, which is described in section 2.13.1. We again used numerical tests to verify that the second Jury condition is satisfied above the curve given by equations (2.116) and (2.117) and violated below it.

2.13.3 Third Jury Condition

We use partial derivatives from Table 2.1 to write the third Jury condition, inequality (2.38), as

$$1 - rx^* + \frac{y^*}{y^* h(y^*)}[1 - y^* h(y^*) - h(y^*)] - \frac{rx^* y^*}{y^* h(y^*)}[1 - y^* h(y^*) - h(y^*)] + x^* y^* \left(\frac{1}{x^*} - r\right) < 1. \tag{2.118}$$

This simplifies to

$$\frac{y^* e^{y^*}}{e^{y^*} - 1}(1 - x^* r) < 1, \tag{2.119}$$

where we use equation (2.17) for $h(y)$.

To find the curve where stability of the equilibrium changes, we again consider an equation instead of the inequality. After eliminating x using equation (2.111) from the host isocline, we solve for r as a function of y,

$$r = \frac{ye^y + y^2 e^y - e^y + 1}{ye^y}. \tag{2.120}$$

As was done in Section 2.13.2, we use the parasitoid nullcline, equation (2.112), with equation (2.120) to write b as a function of y,

$$b = \frac{y^3 e^y + y^2 e^y - y e^y + y}{(e^y - 1)(y e^y - e^y + 1)}, \tag{2.121}$$

noting again that y functions as a parameter used to trace out a curve in r–b space.

Equations (2.120) and (2.121) give the boundary of the region in parameter space where the coexistence equilibrium satisfies the third Jury condition. We numerically verified that the third Jury condition is satisfied above the curve and violated below it.

Additionally, when $r = 0$, the x-axis is a line of equilibrium points, as stated in Section 2.13.1. Under these conditions, the expression for the determinant simplifies to $\Delta = 1$, and so the third Jury condition is also violated for $r = 0$ ($R_0 = 1$).

Chapter 3

HOST–PARASITOID DYNAMICS AND CLIMATE-DRIVEN RANGE SHIFTS

3.1 Introduction

The earth is currently experiencing an unprecedented global rate of species extinction [14]. Extinction is driven by numerous factors, including pollution, spread of invasive species, natural resource extraction, habitat fragmentation and other changes due to anthropogenic land use. One of main drivers of extinction is climate change, and it has been shown that extinction will continue to accelerate with increased global warming [14, 93].

As a response to climate changes, suitable habitat ranges are shifting latitudinally and upwards in elevation [14, 17, 72, 73]. Local extirpation and eventual global extinction of a species will result if populations of a species are unable to move with their shifting habitat. To better understand and predict the conditions that determine whether or not a species can persist as its range shifts, ecologists are using quantitative tools and mathematical models.

Since the early 2000s, researchers have been incorporating climate change velocity into mechanistic mathematical models that describe the growth and dispersal of biological populations. Potapov and Lewis [75], Berestycki et al. [11], and Leroux et al. [52] each incorporated a moving habitat into continuous-time reaction–diffusion models. These models inherently assume that growth and dispersal occur simultaneously. To better model distributions for species that have distinct growth and dispersal stages, Zhou and Kot [105, 106] introduced climate-driven range shifts in a discrete-time integrodifference-equation (IDE) model. IDE models also have the advantage of being able to incorporate a vast range of dispersal kernels to more accurately model species spread.

Zhou and Kot's [105, 106] IDE model for a shifting habitat is

$$n_{t+1}(x) = \int_{-L/2+ct}^{L/2+ct} k(x,y) f[n_t(y)] dy. \tag{3.1}$$

This model includes two discrete stages to map the population density at generation t, $n_t(x)$, to the population density at generation $t+1$.

In the first stage, which is sedentary, individuals within the habitat patch, $[-L/2 + ct, L/2 + ct]$ undergo local processes, such as reproduction, death, birth, and growth. The growth or recruitment function f is chosen for a specific species or category of species to describe biological processes that happen in place.

In the second stage, individuals disperse. For plants, dispersal occurs for seeds, while dispersers of other species like insects are adults. For each source, y, function $k(x,y)$ is a nonnegative probability density function in x, describing the movement of the dispersers from y. All locations $y \in [-L/2 + ct, L/2 + ct]$ contribute individuals that move to location x, according to probabilities determined by the dispersal kernel. The density at location x after dispersal is determined by integrating over source contributions. Individuals may be inside or outside the patch at the end of the second stage, but only individuals within the shifted patch will reproduce at the start of the next cycle.

Biotic interactions are also important to consider when modeling species distributions in the context of climate change [94]. Rinnan [80] recently used an IDE model to consider the possible outcomes for two competing species on a moving habitat, and Harsch et al. [30] stated the need for further consideration of biotic interactions in IDE models.

In this chapter, I describe and analyze an IDE model for the dynamics of a host–parasitoid system subject to climate change. For individual species and competing species on a moving habitat, there is a critical speed, c^*, beyond which a population cannot keep up with the movement of its habitat [31, 74, 80, 105, 106]. However, the mathematical tools appropriate for single-species models are not sufficient for an IDE system with multiple species. I therefore explain a reduction from the spatially-explicit IDE model to a spatially-implicit system of

difference equations. I then compare approximation methods for determining critical speed for persistence and conclude that an approximation known as geometric symmetrization is the best method for estimating the critical speed for parasitoid persistence. Using geometric symmetrization, I explore how different biological parameters, including assumptions about habitat patches, impact host–parasitoid dynamics and persistence criteria.

In Section 3.2, I describe the three models considered in this chapter, including biological assumptions. The assumptions in Case 1 describe an ideal scenario for the parasitoid, such that the host density is at its carrying capacity everywhere. In Case 2, the host and parasitoid have the same suitable habitat-patch, while the host's habitat patch is larger than the parasitoid's patch in Case 3.

Methods of analysis for the Case 1 system, which reduces to a single-species IDE, are explained in Section 3.3. Section 3.4 gives a brief summary of the impact of biological parameters on the critical speed for the Case 1 model. I then explain methods of analysis for the Case 2 model in Section 3.5. In Section 3.6, I compare the different approximation methods and use geometric symmetrization to explore how biological parameters impact critical speed. Similar methods and results for the Case 3 system are presented in Sections 3.7 and 3.8. I conclude with a discussion of the benefits and limitations of using spatially-implicit difference equations to analyze IDE systems and the potentially surprising accuracy of geometric symmetrization and iterated geometric symmetrization.

3.2 Model formulation

Consider interacting host and parasitoid populations on a one-dimensional habitat where there are discrete growth and dispersal stages, described by the IDE system

$$N_{t+1}(x) = \int_{\Omega_n} k_n(x,y) F_n[N_t(y), P_t(y)]dy, \tag{3.2a}$$

$$P_{t+1}(x) = \int_{\Omega_p} k_p(x,y) F_p[N_t(y), P_t(y)]dy. \tag{3.2b}$$

For this model, let $N_t(x)$ be the density of reproducing host adults in generation t at location x, and let $P_t(x)$ be the density of adult female parasitoids in generation t at location x. Further, let Ω_i be the patch of habitat that is suitable for species i. If an individual is outside the patch, that individual does not reproduce.

The sedentary stage for hosts and parasitoids is captured by the functions F_n and F_p, which describe intraspecific competition and interspecific parasitism between individuals at location y. Dispersal occurs after competition and parasitism, when the new adults of each species move from location y to location x. The density of adults of each species after dispersal at location x is the sum of adults from all possible contributing locations y that are at x at the end of the dispersal stage. In this model, the dispersal kernel, $k_i(x, y)$, is the probability that an adult from location y disperses to location x.

A number of researchers have shown that population dynamics of hosts and parasitoids are impacted by the timing of density-dependent competition and parasitism in the life cycle of hosts [19, 61, 98]. To provide biological specificity for this analysis, I have chosen to focus on the scenario in which density dependence precedes parasitism in the life cycle of the host. The model for this situation is

$$N_{t+1}(x) = \int_{\Omega_n} k_n(x, y) N_t(y) G[N_t(y)]\{1 - P_t H[P_t(y)]\} dy, \tag{3.3a}$$

$$P_{t+1}(x) = \int_{\Omega_p} k_p(x, y) \tilde{c} N_t(y) G[N_t(y)] P_t(y) H[P_t(y)] dy, \tag{3.3b}$$

where $G[N_t(y)]$ is the host per-capita-recruitment and $H[P_t(y)]$ is the fraction of hosts that succumb to parasitism per adult female parasitoid. The clutch size, $\tilde{c}$, is the average number of female parasitoid eggs laid on or in a single host that emerge and successfully become reproducing adults.

Figure 3.1 shows host and parasitoid local population dynamics occurring prior to dispersal with density dependence preceding parasitism in the life cycle of the host, in accordance with system (3.3). For a system with a forest tent-caterpillar host and a generic parasitoid,

Cobbold et. al [18] describe how host adults disperse, reproduce, and lay eggs in midsummer, such that the host overwinters in the egg stage. On the other hand, parasitoids overwinter as pupae, and the adults disperse in spring to reproduce and lay eggs when they encounter and parasitize hosts. Cobbold et al. [18] also explain that parasitism of the forest tent caterpillar can occur "before, during, or after density-dependent host mortality, depending on the parasitoid species." The mathematical model analyzed by Cobbold et al. [18] assumes that parasitism precedes density dependence in the life cycle of the host and that parasitized hosts subsequently compete for resources. This differs from system (3.3) for which parasitism follows host density-dependent competition. See also Marcinko and Kot [59] for a more in-depth explanation of the local host and parasitoid interactions assumed in this chapter.

Common expressions for host density-dependent recruitment include the Beverton–Holt [12] growth function, which is compensatory, and the Ricker [78] growth function, which is overcompensatory. There is also a range of appropriate functions for parasitism, and it is common to represent the fraction of hosts that escape parasitism with the zero term of the negative binomial distribution,

$$f(P_t) = \left(1 + \frac{aP_t}{\kappa}\right)^{-\kappa}, \tag{3.4}$$

where a is parasitoid searching efficiency [19, 55, 61]. This equation can account for different levels of parasitoid aggregation by varying κ.

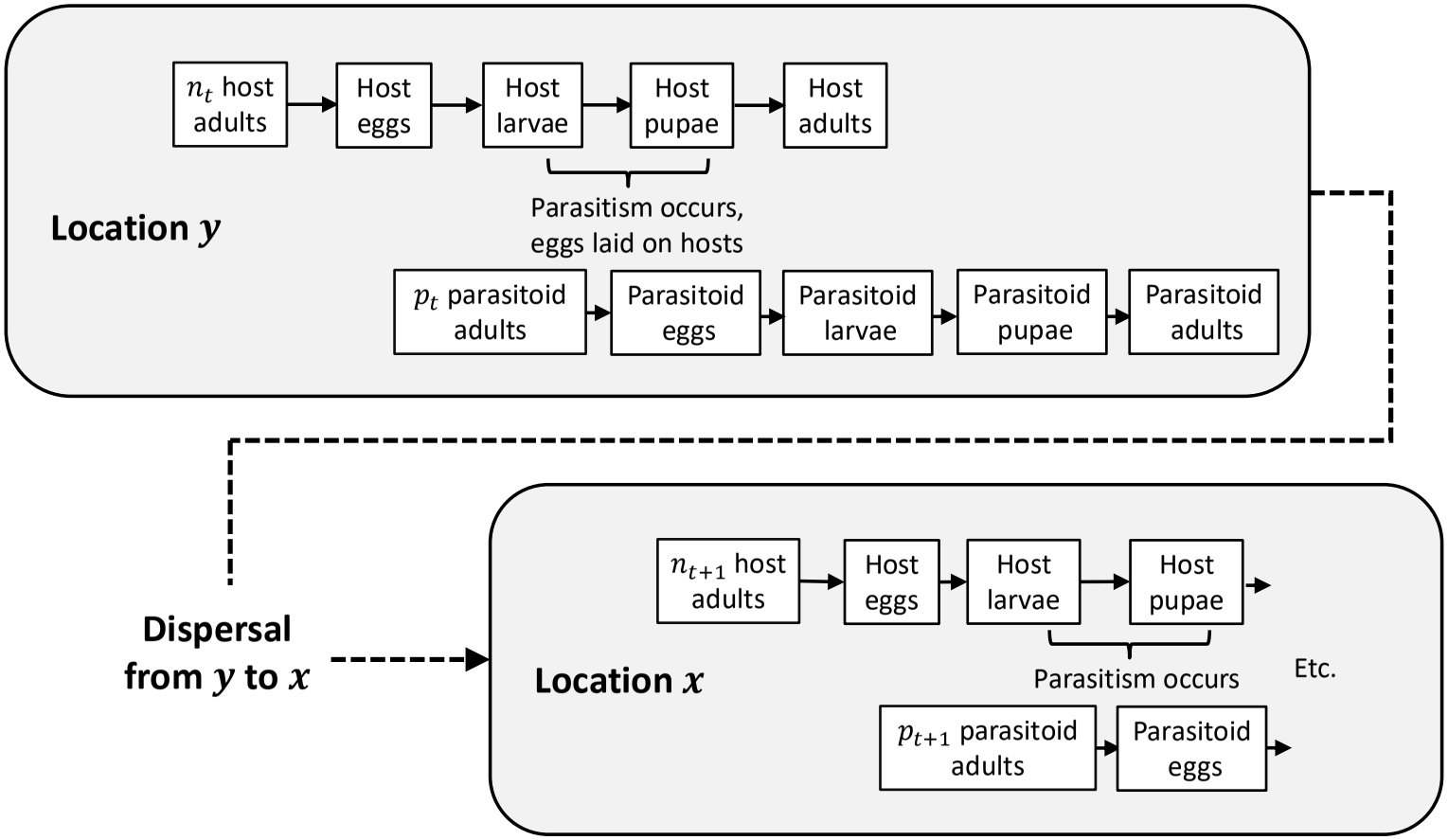

Figure 3.1: A life-cycle illustration for hosts and parasitoids demonstrating that local population dynamics occur prior to dispersal.

As shown in [59], the simplest dynamics for the non-spatial host–parasitoid system arise from the model that uses Beverton–Holt growth,

$$N_t G(N_t) = \frac{R_0 N_t}{1 + \frac{(R_0-1)}{K} N_t}, \tag{3.5}$$

and a fractional form of parasitism resulting from using $\kappa = 1$ in equation (3.4). For $\kappa = 1$, the fraction of hosts that succumb to parasitism per adult female parasitoid is

$$H(P_t) = \frac{a}{1 + aP_t}. \tag{3.6}$$

In these expressions, R_0 is the host net reproductive rate, K is the host carrying capacity, and a is the parasitoid searching efficiency.

For the purposes of this analysis, I use equation (3.5) for host density-dependent recruitment and equation (3.6) for parasitism. This choice will lead to an understanding of the basic persistence question and avoid systems in which pattern formation may occur.

To nondimensionalize, let $n_t(x) = N_t(x)/K$ and let $p_t(x) = aP_t(x)$. Define the nondimensionalized "clutch-size" as $b = a\tilde{c}K$. Then per-capita-recruitment is

$$g[n_t(x)] = \frac{R_0}{1 + (R_0 - 1)n_t(x)}, \tag{3.7}$$

and the fraction of hosts that succumb to parasitism, $p_t(y)h[p_t(y)]$, can be written with

$$h[p_t(y)] = \frac{1}{1 + p_t(y)}. \tag{3.8}$$

Following the same notation choices as in [59], system (3.3) can be rewritten as

$$n_{t+1}(x) = \int_{\Omega_n} k_n(x, y) n_t(y) u[n_t(y), p_t(y)] dy, \tag{3.9a}$$

$$p_{t+1}(x) = \int_{\Omega_p} k_p(x, y) p_t(y) v[n_t(y), p_t(y)] dy, \tag{3.9b}$$

where

$$u[n_t(y), p_t(y)] = g[n_t(y)]\{1 - p_t h[p_t(y)]\} \tag{3.10}$$

and

$$v[n_t(y), p_t(y)] = bn_t(y)g[n_t(y)]h[p_t(y)]. \tag{3.11}$$

Writing this system with functions u and v will simplify the analysis needed in Section 3.5.1.

To investigate the host–parasitoid system with a shifting habitat, I consider three versions of system (3.9). The first case reduces the problem to a single IDE such that traditional IDE methods can be used. In the second case, I assume that the host and the parasitoid exist on the same habitat patch that is moving rightwards at speed c. In the third case, I assume that the suitable habitat-patch for the parasitoid is smaller than the host's suitable patch and both are moving with the same climate velocity. Furthermore, for simplicity in this third case, I assume that the parasitoid patch is centered within the host patch.

3.2.1 Dispersal

Dispersal is an important area of study for both mathematical modeling and experimental understanding of species spread. Within the realm of possible dispersal kernels, the Laplace kernel has the benefit of being both mathematically elegant [47, 48, 49, 57, 77, 95] and ecologically relevant as a leptokurtic distribution [18, 47, 49]. Examples of analysis of insect dispersal data that exhibits leptokurtosis can be found in [2, 13, 15, 16, 24, 27, 34, 86, 87, 97, 101, 102, 103]. While experimental dispersal kernels tend to exhibit fatter tails than those of the Laplace kernel, kernels with exponentially decaying tails are still widely used [67].

The Laplace kernel is

$$k(x, y) = k(x - y) = \frac{1}{2\delta} e^{-|x-y|/\delta}, \tag{3.12}$$

where δ is the mean dispersal distance and variance is $\sigma^2 = 2\delta^2$. The Laplace kernel only depends on the distance between x and y, and is an example of a kernel that describes homogeneous and isotropic dispersal. For examples and specifics in this chapter, I assume

a Laplace kernel. However, most of the following work can be easily numerically replicated with other kernels, including those with fatter tails.

3.2.2 Parameters

This chapter seeks to consider parameter ranges that are biologically reasonable, but also broad enough to explore mathematical implications of the model. Hughes et al. [35] studied host–parasitoid systems with parameters based on Cobbold et al.'s data [19]. For the host net reproductive rate, R_0, Hughes et al. [35] used $R_0 = 1.5, 3, 5, 7$. For the nondimensionalized parasitoid's growth rate, b, Hughes et al. [35] used $b = 1, 5, 10, 30, 50$. For R_0 and b, "baseline parameter values" $R_0 = 2.61$ and $b = 8.06$ were based on Cobbold et al.'s data [19]. These values guide the ranges used for R_0 and b in this chapter, especially in Sections 3.4, 3.6, and 3.8.

Data on dispersal distances for insect hosts and parasitoids is limited, making it challenging to accurately estimate dispersal distance [18, 35]. For a study on population dynamics of a forest tent caterpillar and a generic parasitoid, Cobbold et al. [18] estimated that host dispersal variance is between $\sigma_n^2 = 0.241$ km^2 and $\sigma_n^2 = 0.377$ km^2 for a Laplace distribution and that parasitoid dispersal variance is between $\sigma_p^2 = 0.060$ km^2 and $\sigma_p^2 = 0.241$ km^2. These parameters are based on data from Roland and Taylor [81, 82]. For a slightly wider range of values, I will consider average host dispersal-distances from $\delta_n = 1/30$ km to $\delta_n = 1/2$ km and average parasitoid dispersal-distances from $\delta_p = 1/70$ km to $\delta_p = 1/5$ km.

As described by Cobbold et al. [18], space in an IDE model with a finite patch length can be scaled with respect to the patch length, L_0, such that the scaled habitat-patch length is $L = 1$ and the scaled average dispersal-distance is given by $\delta = \delta_0/L_0$. I will primarily use $L = 1$ in the following sections, except when the host and parasitoid reside on patches with different lengths. If the system has a true patch-length of $L_0 = 1$ km, scaled average dispersal-distances δ_n and δ_p are in km. Otherwise, the spatial parameters are effectively

nondimensionalized by the use of $L = 1$.

3.2.3 Case 1: Best possible scenario for parasitoid

First consider a scenario in which a parasitoid population exists on a finite one-dimensional patch of habitat with length L that is moving at speed c. Suppose also that the corresponding host population exists on a patch that is large enough to be approximated as infinite in comparison to the parasitoid habitat-patch. Additionally, assume that the host has a large enough net reproductive rate, R_0, that its density is at its carrying capacity throughout its infinite habitat. In some sense, this scenario represents an ideal set of circumstances for the parasitoid species since the host species exists at carrying capacity wherever the parasitoid encounters the host. As is common with IDE population models, I also assume that dispersal is homogeneous and isotropic so that dispersal depends on the distance between locations x and y.

The corresponding IDE system is thus

$$n_{t+1}(x) = 1, \tag{3.13a}$$

$$p_{t+1}(x) = \int_{-L/2+ct}^{L/2+ct} k_p(x-y) b n_t(x) g[n_t(x)] p_t(y) h[p_t(y)] dy, \tag{3.13b}$$

where $n_t(x)$ is the nondimensionalized host density at location x and $p_t(x)$ is the nondimensionalized parasitoid density at location x. With Beverton–Holt recruitment, $g(1) = 1$, so equation (3.13b) is

$$p_{t+1}(x) = \int_{-L/2+ct}^{L/2+ct} k_p(x-y) b \frac{p_t(y)}{1+p_t(y)} dy, \tag{3.14}$$

with $h[p_t(y)]$ from equation (3.8).

Since the habitat is assumed to be moving with constant speed, c, I look for a traveling pulse,

$$p_t(x) = \hat{p}_t(x - ct). \tag{3.15}$$

Then substitute this into the convolution equation (3.14) so that

$$\hat{p}_{t+1}[x - c(t+1)] = \int_{-L/2+ct}^{L/2+ct} k_p(x-y) b \frac{\hat{p}_t(y-ct)}{1+\hat{p}_t(y-ct)} dy. \tag{3.16}$$

Now, change variables such that $\hat{x} = x - ct$ and $\hat{y} = y - ct$,

$$\hat{p}_{t+1}(\hat{x} - c) = \int_{-L/2}^{L/2} k_p[\hat{x} + ct - (\hat{y} + ct)] b \frac{\hat{p}_t(\hat{y})}{1+\hat{p}_t(\hat{y})} d\hat{y}. \tag{3.17}$$

Then shift $\hat{x}$ by c, to get

$$\hat{p}_{t+1}(\hat{x}) = \int_{-L/2}^{L/2} k_p(\hat{x} + c - \hat{y}) b \frac{\hat{p}_t(\hat{y})}{1+\hat{p}_t(\hat{y})} d\hat{y}. \tag{3.18}$$

After dropping the hats for notational convenience, this equation is

$$p_{t+1}(x) = \int_{-L/2}^{L/2} k_p(x + c - y) b \frac{p_t(y)}{1+p_t(y)} dy. \tag{3.19}$$

Because this case reduces to a single IDE, I will analyze the persistence of the parasitoid population using techniques from [105] in Section 3.3.

3.2.4 Case 2: Host and parasitoid share a patch

The second model assumes that both the parasitoid and host populations exist on a finite one-dimensional patch of habitat with length L that is moving at speed c. The IDE system for this case is

$$n_{t+1}(x) = \int_{-L/2+ct}^{L/2+ct} k_n(x-y) n_t(y) u[n_t(y), p_t(y)] dy, \tag{3.20a}$$

$$p_{t+1}(x) = \int_{-L/2+ct}^{L/2+ct} k_p(x-y) p_t(y) v[n_t(y), p_t(y)] dy, \tag{3.20b}$$

where I again assume homogeneous and isotropic dispersal.

Similarly to Case 1, look for solutions of the form

$$n_t(x) = \hat{n}_t(x - ct), \tag{3.21a}$$

$$p_t(x) = \hat{p}_t(x - ct). \tag{3.21b}$$

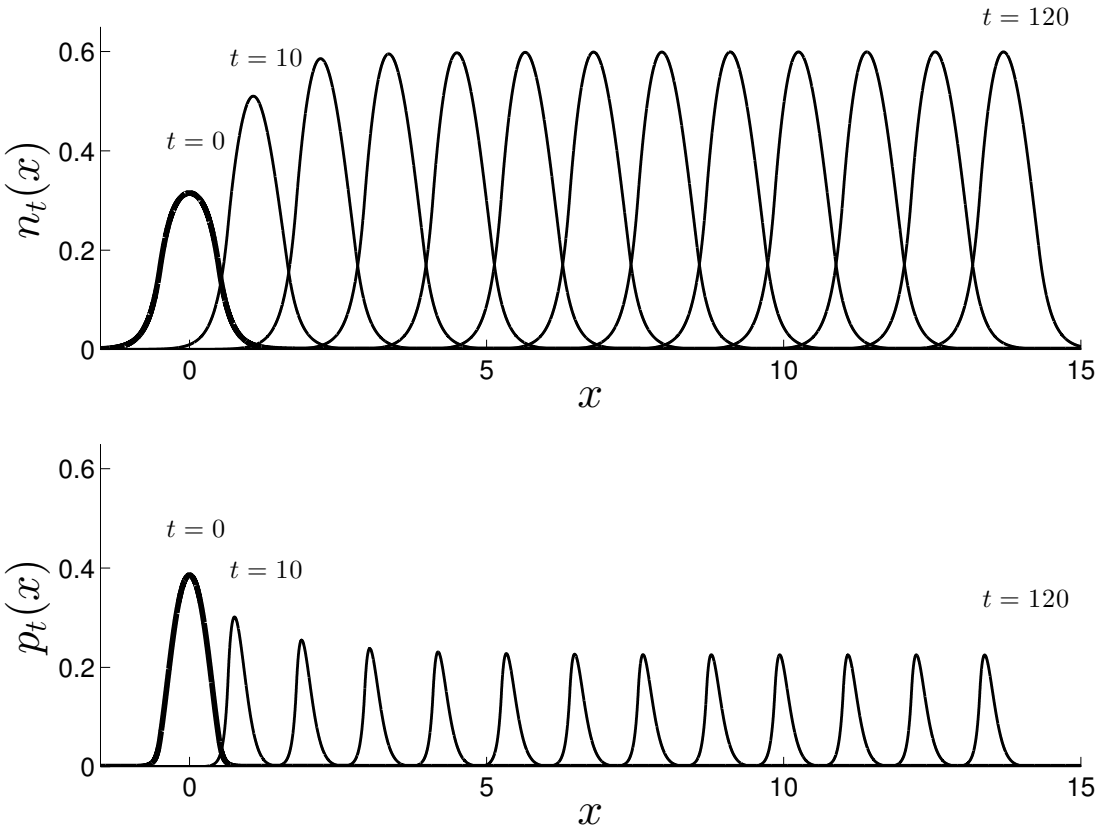

Figure 3.2: A simulation of the population distributions from Case 2 where the host and parasitoid occupy the same habitat that is moving to the right at speed c. For these simulations, $L = 1$, $R_0 = 2$, $b = 3$, $\delta_n = 1/5$, $\delta_p = 1/15$, and $c = 0.115$. The distributions at $t = 0$ are shown with a thicker line, centered around $x = 0$. The $t = 0$ distributions were obtained by iterating system (3.20) with $c = 0$ for 120 generations starting from an initial condition with both populations having a uniform distribution in the patch. The density for the host's uniform initial condition was 50, and the density for the parasitoid's uniform initial condition was 6. The $t = 0$ distributions in the figure represent the steady-state population distributions with no habitat movement. The population distributions for the moving habitat are shown every 10 generations. Note that the distributions shown are the adults after dispersal, but only those within the habitat patch $\Omega = [-L/2 + ct, L/2 + ct]$ reproduce at the next step. The parasitoid population decreases to a new steady-state distribution on the moving patch, while the lower population of parasitoids allows the host population to increase to a new steady-state distribution on the moving patch. If speed is sufficiently increased, the parasitoid population will die out. The convolutions at each iteration were computed using `MATLAB`'s built-in '`conv`' function with $dx = 2^{-10}$.

Substituting these into system (3.20) gives

$$\hat{n}_{t+1}(x-ct-c) = \int_{-L/2+ct}^{L/2+ct} k_n(x-y)\hat{n}_t(y-ct)u\left[\hat{n}_t(y-ct),\hat{p}_t(y-ct)\right]dy, \tag{3.22a}$$

$$\hat{p}_{t+1}(x-ct-c) = \int_{-L/2+ct}^{L/2+ct} k_p(x-y)\hat{p}_t(y-ct)v[\hat{n}_t(y-ct),\hat{p}_t(y-ct)]dy. \tag{3.22b}$$

Now use the change of variables $\hat{x} = x - ct - c$ and $\hat{y} = y - ct$, so the system is

$$\hat{n}_{t+1}(\hat{x}) = \int_{-L/2}^{L/2} k_n(\hat{x}+c-\hat{y})\hat{n}_t(\hat{y})u\left[\hat{n}_t(\hat{y}),\hat{p}_t(\hat{y})\right]d\hat{y}, \tag{3.23a}$$

$$\hat{p}_{t+1}(\hat{x}) = \int_{-L/2}^{L/2} k_p(\hat{x}+c-\hat{y})\hat{p}_t(\hat{y})v\left[\hat{n}_t(\hat{y}),\hat{p}_t(\hat{y})\right]d\hat{y}. \tag{3.23b}$$

Again dropping the hats for notational convenience, this system becomes

$$n_{t+1}(x) = \int_{-L/2}^{L/2} k_n(x+c-y)n_t(y)u\left[n_t(y),p_t(y)\right]dy, \tag{3.24a}$$

$$p_{t+1}(x) = \int_{-L/2}^{L/2} k_p(x+c-y)p_t(y)v\left[n_t(y),p_t(y)\right]dy. \tag{3.24b}$$

Numerical simulations of this host–parasitoid system can either use system (3.20) or system (3.24). The first shows the population distributions from the observer's perspective, while the second shows changes in the population distribution from the moving-habitat frame of reference. In either case, a shifting habitat leads to a decrease in the total parasitoid population and an increase in the total host population as it experiences an ecological release from the parasitoid species. The qualitative shape of the population distribution on the habitat patch changes for both species, becoming narrower. The parasitoid population distribution skews towards the back end of the patch, as seen in Figure 3.2.

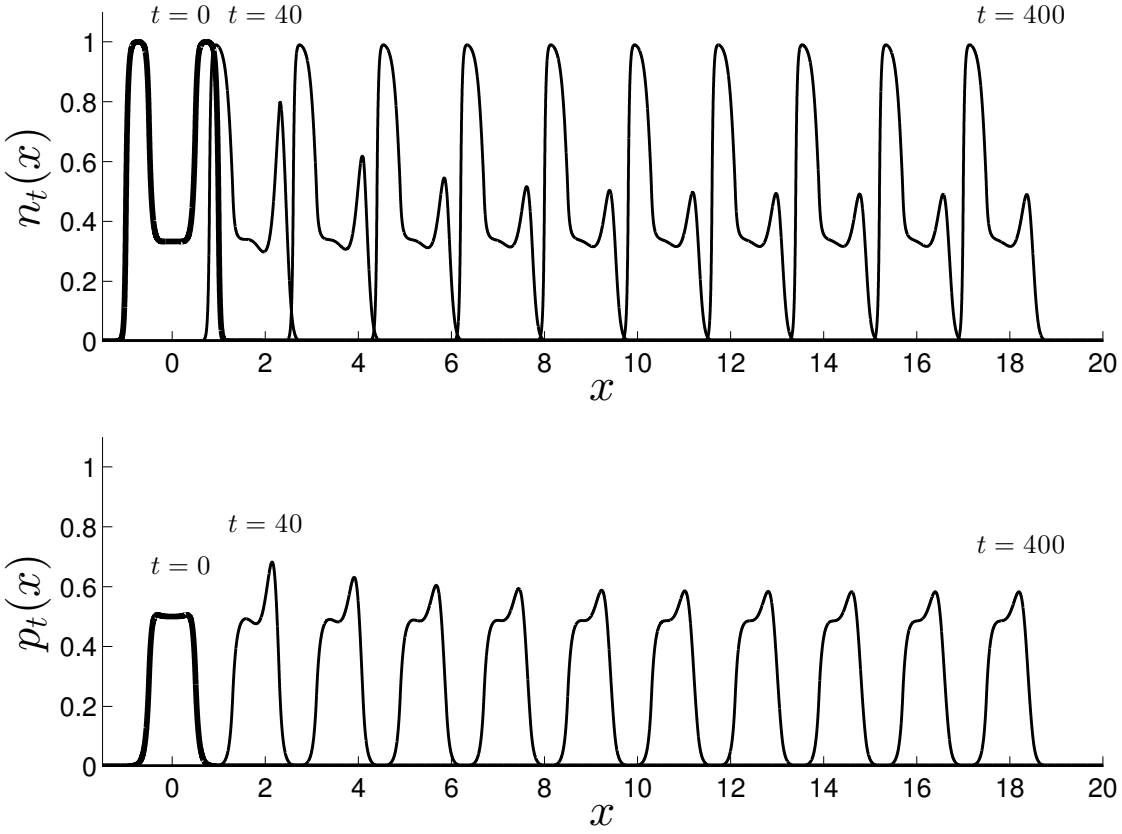

Figure 3.3: A simulation of the population distributions from Case 3. The host occupies a patch of habitat with length $L_n = 2$, and the parasitoid occupies a patch centered within the host habitat with length $L_p = 1$. Both patches move to the right at speed c. For these simulations, $R_0 = 2$, $b = 3$, $\delta_n = 1/40$, $\delta_p = 1/15$, and $c = 0.045$. The distributions at $t = 0$ are shown with a thicker line, centered around $x = 0$. The $t = 0$ distributions were obtained by iterating system (3.25) with $c = 0$ for 120 generations starting from an initial condition with both populations having a uniform distribution in their patches. The density for the host's uniform initial condition was 50, and the density for the parasitoid's uniform initial condition was 6. The $t = 0$ distributions in the figure represent the steady-state population distributions with no habitat movement. The population distributions for the moving habitat are shown every 40 generations. The convolutions at each iteration were computed using `MATLAB`'s built-in '`conv`' function with $dx = 2^{-10}$.

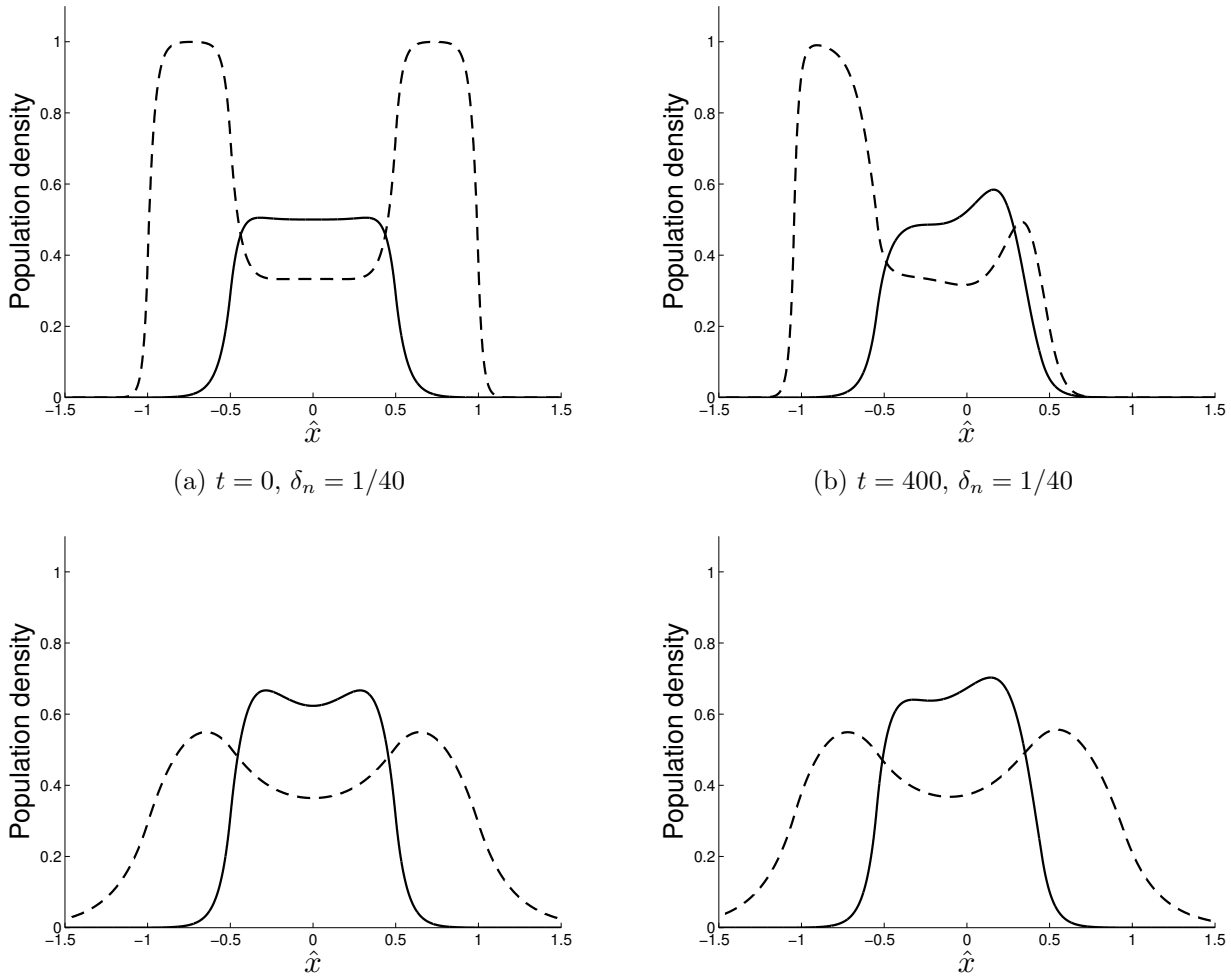

(a) $t = 0$, $\delta_n = 1/40$

(b) $t = 400$, $\delta_n = 1/40$

(c) $t = 0$, $\delta_n = 1/5$

(d) $t = 400$, $\delta_n = 1/5$

Figure 3.4: Population distributions for Case 3. Subfigures 3.4a and 3.4c show the host density (dashed) and the parasitoid density (solid) with no habitat movement for two different values of host average dispersal-distance, δ_n. Notice that the distributions are symmetric about $\hat{x} = 0$. Subfigures 3.4b and 3.4d show the host density (dashed) and the parasitoid density (solid) with respect to the moving habitat coordinates after 400 iterations, again for two different values of average host dispersal-distance. Habitat speed for these simulations was $c = 0.045$. For a smaller host dispersal-distance, δ_n, the shape of the population distributions of both host and parasitoid change more in the moving habitat compared to the stationary patch (subfigures 3.4a and 3.4b), and the host loses the refuge habitat at the front edge of the patch (subfigure 3.4b). For the case with larger host average dispersal-distance, the shapes of the host and parasitoid distributions are less affected by the moving habitat (subfigures 3.4c and 3.4d). Other parameters for all figures are $L_n = 2$, $L_p = 1$, $R_0 = 2$, $b = 3$, $\delta_p = 1/15$.

3.2.5 Case 3: Host patch exceeds parasitoid patch

For Case 3, begin with host–parasitoid IDE system (3.9) and now define $\Omega_n = [-L_n/2 + ct, L_n/2 + ct]$ and $\Omega_p = [-L_p/2 + ct, L_p/2 + ct]$ where $L_p < L_n$ and

$$n_{t+1}(x) = \int_{-L_n/2+ct}^{L_n/2+ct} k_n(x-y)n_t(y)u[n_t(y), p_t(y)]dy, \tag{3.25a}$$

$$p_{t+1}(x) = \int_{-L_p/2+ct}^{L_p/2+ct} k_p(x-y)p_t(y)v[n_t(y), p_t(y)]dy. \tag{3.25b}$$

This is the setup where the parasitoid has a smaller habitat than the host and the parasitoid's habitat is centered within the host's habitat patch.

After following steps akin to those in Section 3.2.4 the system is

$$n_{t+1}(x) = \int_{-L_n/2}^{L_n/2} k_n(x+c-y)n_t(y)u\left[n_t(y), p_t(y)\right] dy, \tag{3.26a}$$

$$p_{t+1}(x) = \int_{-L_p/2}^{L_p/2} k_p(x+c-y)p_t(y)v\left[n_t(y), p_t(y)\right] dy. \tag{3.26b}$$

I have again dropped the hats for notational convenience. The equation for the host dynamics, (3.26a), can also be written as

$$n_{t+1}(x) = \begin{cases} \displaystyle\int_{-L_n/2}^{-L_p/2} k_n(x+c-y)n_t(y)u\left[n_t(y), 0\right] dy \\ \quad + \displaystyle\int_{-L_p/2}^{L_p/2} k_n(x+c-y)n_t(y)u\left[n_t(y), p_t(y)\right] dy \\ \quad + \displaystyle\int_{L_p/2}^{L_n/2} k_n(x+c-y)n_t(y)u\left[n_t(y), 0\right] dy, \end{cases} \tag{3.27}$$

since the parasitoid population cannot reproduce outside its own patch.

As is true for Case 2, numerical simulations for Case 3 can be based on the observer's perspective or the moving-habitat frame of reference. Figure 3.3 shows a simulation of Case 3 from the observer's perspective, using system (3.25). The initial distributions in the figure represent the steady-state population distributions with no habitat movement. The

population distributions for the moving habitat are shown every 40 generations. Note that the distributions shown are the adults after dispersal, but only those within the habitat patch $\Omega = [-L_i/2 + ct, L_i/2 + ct]$ reproduce. While the peak population density for the parasitoid is higher for the moving habitat than the stationary habitat, the total parasitoid population decreases to a new steady state when the patch is moving. The lower population of parasitoids allows the host population to increase to a new steady-state distribution on the moving patch. If speed is sufficiently increased, the parasitoid population will die out.

Case 3 yields a broader range of possible population distribution shapes than Case 1 or Case 2, due to the host having a refuge habitat both in front of and behind the parasitoid population. Using system (3.26), it is possible to plot initial and final distributions for hosts and parasitoids with respect to the moving habitat frame. See Figure 3.4 for examples of population distributions for Case 3. In general, the host population will be lower in the middle than on either side, because the front and back edges of the patch are refuge habitat for the host. However, when the patches move, the host population at the front of the patch decreases, and that region decreases in effectiveness as a refuge.

3.3 Case 1 methods

Zhou and Kot [105, 106] first developed methods for determining the critical speed from an IDE model for a single species on a moving habitat. Recall from Section 3.2.3 that the Case 1 model, system (3.13), reduces to the single IDE, equation (3.19). Therefore, the critical speed for parasitoid survival in optimal circumstances can be determined using methods from [105, 106].

Specifically, after assuming a traveling pulse and shifting to the moving-habitat frame, as was done in Section 3.2.3, I now linearize equation (3.19) around the trivial solution, $p_t(x) = 0$. Instability of the trivial solution will correspond to persistence of the parasitoid

population. The linearization is

$$p_{t+1}(x) = b \int_{-L/2}^{L/2} k_p(x + c - y) p_t(y) dy. \tag{3.28}$$

Next, I look for solutions of the form

$$p_t(x) = \lambda^t \xi(x). \tag{3.29}$$

Perturbations off the trivial solution are thus governed by

$$\lambda \xi(x) = b \int_{-L/2}^{L/2} k_p(x + c - y) \xi(y) dy, \tag{3.30}$$

where λ is an eigenvalue of the integral operator with corresponding eigenfunction $\xi(x)$. Equation (3.30) is a homogeneous Fredholm integral equation of the second kind.

While the general eigenvalue problem expressed in equation (3.30) is nasty, certain classes of kernels provide tractable solution methods. If we restrict the domain to $x \in [-L/2, L/2]$ and $y \in [-L/2, L/2]$ with finite L and use a continuous dispersal kernel with infinite support, then the linear integral operator is compact. In this case, the eigenvalues of equation (3.30) form a discrete set.

Furthermore, a positive kernel guarantees a simple, positive dominant eigenvalue, using Jentzch's theorem [39]. In this case, stability of the trivial solution will be lost as the dominant eigenvalue passes through $\lambda = 1$. The Laplace kernel satisfies the criteria for Jentzch's theorem. Thus, the critical speed for parasitoid persistence is the speed c^* for which the spectral radius of the integral operator is one. Kot and Phillips [48] give a nice overview of methods available for finding the critical speed under the previous assumptions.

3.3.1 Numerical approach

To find the critical speed for Case 1, I follow the numerical approach used by [48, 105, 106] in which I discretize equation (3.30), which yields a matrix eigenvalue problem.

Specifically, I use Nystrom's method [21, 57, 76] with the trapezoid rule to write

$$\lambda\xi(x_i) = b\frac{\Delta x}{2}\sum_{j=1}^{N-1}\left[k_p(x_i + c - y_j)\xi(y_j) + k_p(x_i + c - y_{j+1})\xi(y_{j+1})\right] \tag{3.31}$$

for $i = 1, 2, \cdots, N$ and $\Delta x = L/(N-1)$ with $N-1$ subintervals. Equation (3.30) reduces to the matrix system

$$\lambda\boldsymbol{\xi} = b\mathbf{K}\boldsymbol{\xi}, \tag{3.32}$$

where $\boldsymbol{\xi}$ is an $N \times 1$ vector of the densities and $\mathbf{K}$ is an $N \times N$ matrix defined by

$$k_{ij} = \begin{cases} \frac{1}{2}k(x_i + c - y_j)\Delta x, & j = 1, \\ k(x_i + c - y_j)\Delta x, & 2 \le j \le N-1, \\ \frac{1}{2}k(x_i + c - y)j)\Delta x, & j = N, \end{cases} \tag{3.33}$$

with k as the Laplace kernel, equation (3.12).

One can either use integral equation (3.30) or matrix system (3.32) to obtain the dominant eigenvalue, which depends continuously on the model parameters. For the results in Section 3.4, I used the method of bisection to find the critical speed, which is the speed, c^* such that the spectral radius of matrix $\mathbf{K}$, $\rho(\mathbf{K})$, equals 1. At each step of the algorithm, I used `MATLAB`'s built-in '`eigs`' function to find the dominant eigenvalue, and then adjusted c accordingly. Other variations on these numerical techniques are discussed in [31, 48, 74, 105, 106].

3.4 Case 1 results

Unsurprisingly, the critical speed for parasitoid persistence in Case 1 increases monotonically with increasing b. Note that this is a result previously shown by Zhou and Kot [106] for the Laplace dispersal kernel, where b in equation (3.28) is effectively the net reproduction rate for the parasitoid species. Biologically, higher rates of reproduction for the parasitoid increase its ability to survive as the habitat shifts.

Figure 3.5 shows the dependence of critical speed on average parasitoid dispersal-distance, δ_p, for eight different values of b ranging from $b = 2.2$ to $b = 3.6$. Initially, the critical speed increases as dispersal distance increases, as dispersers are better able to make use of newly available habitat in front of the previous generation's patch. However, if average dispersal-distance increases too much, the population suffers larger losses from both dispersers left behind as the habitat patch advances and dispersers that overdispersed in front of the new habitat. Eventually, too many dispersers are lost from longer distance dispersal, and the population cannot survive at all.

Figure 3.5 also shows that for larger average dispersal distances, increases in b have a larger impact on the critical speed for persistence. In all cases, the critical speed predicted by Case 1 will be an upper bound for the critical speed predicted by Cases 2 and 3, since Case 1 represents a set of host assumptions that are an unrealistic ideal for the parasitoid species.

3.5 Case 2 methods

For studies of a single-species IDE model with moving habitat, the standard approach for determining critical speed involves linearizing around the trivial equilibrium and using an ansatz to generate an eigenvalue problem [31, 48, 74, 79, 105, 106]. Persistence of the population then corresponds to instability of the trivial equilibrium, under various assumptions. However, instability of the trivial or extinction equilibrium of an IDE system with two species does not correspond to persistence of both species, due to the existence of a state or states where one of the species persists and the other dies out.

Cobbold et al. [18] analyzed a host–parasitoid IDE system with finite, stationary habitat by linearizing around the exclusion equilibrium, $(n^*(x), 0)$. They then used Van Kirk and Lewis' [95] average dispersal success approximation for the exclusion equilibrium to determine a critical patch size. In the same study, Cobbold et al. [18] also used a spatially-

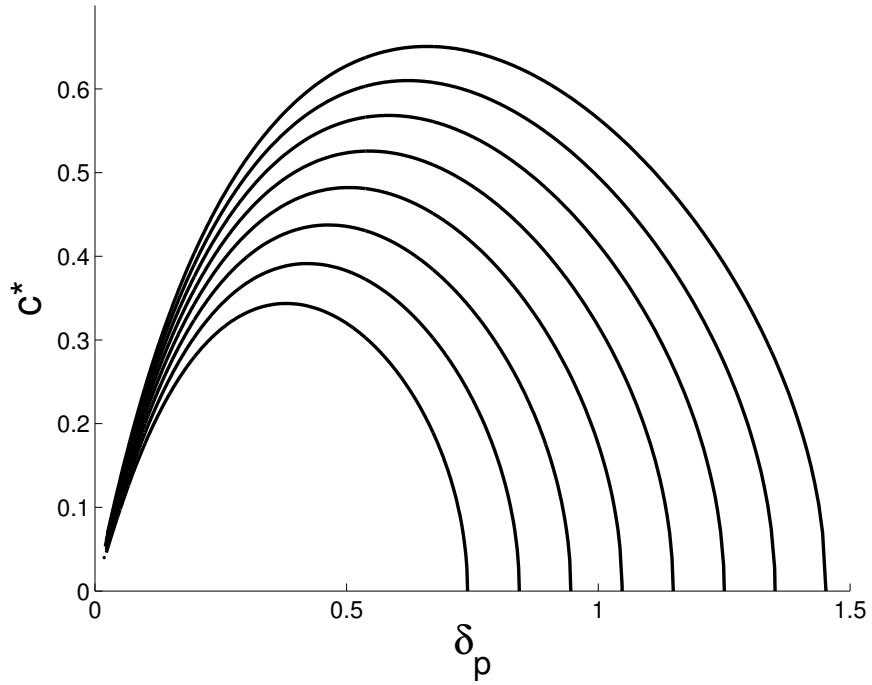

Figure 3.5: Numerically-computed critical speed for parasitoid persistence for Case 1. Each curve has a fixed b value and varying average dispersal-distance, δ_p. Values of b range from 2.2 to 3.6 in steps of 0.2 with the bottom curve corresponding to $b = 2.2$.

implicit system of difference equations to approximate the spatially-explicit host–parasitoid IDE model. This second approach is applicable for a broader range of kernels, and informs my methods of analysis for the shifting-habitat IDE model, system (3.24).

A spatially-implicit approximation to IDE system (3.24) requires an approximation for the probability that a disperser remains inside the patch during the dispersal phase. Alternately, one can think of this same expression as the proportion of the population that remains in the patch after the dispersal stage. For IDEs with stationary patches, this concept has been used in a number of ecological contexts with great success [18, 26, 35, 56, 58, 77, 95].

In Section 3.5.1, I apply a spatially implicit approximation approach to derive criteria for parasitoid persistence. Van Kirk and Lewis' [95] average dispersal success approximation has been shown to perform poorly in approximating IDEs with asymmetric kernels arising from a moving habitat [48, 79]. Therefore, I describe a number of possible approximations for the proportion of the population remaining in the patch after dispersal. In order to compare the usefulness of these approximations, I then explain how the parasitoid critical speed can be determined from simulations.

3.5.1 Approximation methods

Heuristically, the average host and parasitoid populations on the patch $[-L/2, L/2]$ in the moving-habitat frame of reference can be expressed as

$$\bar{n}_{t+1} = \Phi_n \bar{n}_t u(\bar{n}_t, \bar{p}_t), \tag{3.34a}$$

$$\bar{p}_{t+1} = \Phi_p \bar{p}_t v(\bar{n}_t, \bar{p}_t), \tag{3.34b}$$

where $\bar{n}_t$ and $\bar{p}_t$ are average host and parasitoid populations at generation t. Φ_n is the proportion of host dispersers that remain in the patch after dispersal, and Φ_p is the proportion of parasitoid dispersers that remain in the patch after dispersal.

One can also derive two difference equations with the same form as system (3.34). Begin

by denoting the averages of the two populations over the patch as

$$\bar{n}_t = \frac{1}{L}\int_{-L/2}^{L/2} n_t(x)dx \tag{3.35}$$

and

$$\bar{p}_t = \frac{1}{L}\int_{-L/2}^{L/2} p_t(x)dx, \tag{3.36}$$

following the approach in [26, 58, 79, 80]. Note that for this chapter, these averages refer to the average population for the patch in the moving-habitat frame of reference.

Next, compute the average of both sides of the equations for Case 2, system (3.24),

$$\bar{n}_{t+1} = \frac{1}{L}\int_{-L/2}^{L/2} n_{t+1}(x)dx = \frac{1}{L}\int_{-L/2}^{L/2}\int_{-L/2}^{L/2} k_n(x+c-y)n_t(y)u\left[n_t(y),p_t(y)\right]dydx, \tag{3.37a}$$

$$\bar{p}_{t+1} = \frac{1}{L}\int_{-L/2}^{L/2} p_{t+1}(x)dx = \frac{1}{L}\int_{-L/2}^{L/2}\int_{-L/2}^{L/2} k_p(x+c-y)p_t(y)v\left[n_t(y),p_t(y)\right]dydx. \tag{3.37b}$$

Linearizing around $(\bar{n}_t, \bar{p}_t)$ and dropping higher-order terms yields the system,

$$\bar{n}_{t+1} = \bar{n}_t u\left(\bar{n}_t,\bar{p}_t\right)\frac{1}{L}\int_{-L/2}^{L/2}\int_{-L/2}^{L/2} k_n(x+c-y)dydx, \tag{3.38a}$$

$$\bar{p}_{t+1} = \bar{p}_t v\left(\bar{n}_t,\bar{p}_t\right)\frac{1}{L}\int_{-L/2}^{L/2}\int_{-L/2}^{L/2} k_p(x+c-y)dydx. \tag{3.38b}$$

This system can also be expressed as

$$\bar{n}_{t+1} = S_n\bar{n}_t u(\bar{n}_t,\bar{p}_t), \tag{3.39a}$$

$$\bar{p}_{t+1} = S_p\bar{p}_t v(\bar{n}_t,\bar{p}_t), \tag{3.39b}$$

with

$$S_i = \frac{1}{L}\int_{-L/2}^{L/2}\int_{-L/2}^{L/2} k_i(x+c-y)dydx. \tag{3.40}$$

S_i is average dispersal success, as defined by Van Kirk and Lewis [95].

The difference equation approximation, system (3.38), is mathematically valid when the equilibrium population distributions for the host and parasitoid are close to the spatial average for all x. Even when the equilibrium distribution is not close to constant, the approximation tends to be relatively accurate [57, 95].

The complicating aspect of moving-habitat IDE models is that the kernel is not symmetric. Reimer et al. [77] showed that the average dispersal success approximation, equation (3.40), decreases in accuracy as the kernel becomes more asymmetric. Equation (3.40) has also been derived from analytic approximations to the single-species moving-habitat model IDE using Legendre polynomials [48, 106]. Use of this approximation provides decent estimates of critical speed for some parameter regimes, but yields increasingly poor approximations for scenarios with higher critical speeds [48].

In the context of a single-species IDE, average dispersal success, equation (3.40), is the Rayleigh-quotient approximation of the dominant eigenvalue of the integral operator

$$K_i : \quad \xi \mapsto \int_{-L/2}^{L/2} k_i(x,y)\xi(y)dy. \tag{3.41}$$

The validity of this approximation depends on the kernel being symmetric, as discussed by Kot and Phillips [48].

Because Case 2 IDE system (3.24) has asymmetric kernels, I compare a number of approximations to the dominant eigenvalue of the linear integral operator (3.41) with the Laplace kernel evaluated at $x+c-y$ to account for moving habitat. Spectral radii can either be determined using the integral operator in equation (3.41) or a matrix discretization of the integral operator, previously described in Section 3.3.1. The following approximation methods were all compared by Kot and Phillips [48] or Rinnan [79] for a single-species moving-habitat IDE, and have not previously been compared in the context of a two-species IDE moving-habitat model.

Analytic approximations include the average dispersal success approximation, S, Reimer et al.'s [77] modification to the average dispersal success approximation, $\hat{S}$, and the geometric

success function, G, from Rinnan [79, 80] and Kot and Phillips [48]. Numerical approximations begin with discretizing integral operator (3.41) to obtain a matrix $\mathbf{K}_i$, where I use the discretization given in Section 3.3.1. The dominant eigenvalues of $\mathbf{K}_n$ and $\mathbf{K}_p$ will be approximated with maximum and minimum row-sums, iterated row-sums from Yeh [104], and iterated geometric symmetrization from Kot and Phillips [48].

Fixed points and stability

For whichever approximation is used for proportion of the population that remains in the patch after dispersal, Φ_n and Φ_p, one can determine persistence criteria from difference equation system (3.34). Assume compensatory density-dependence and that parasitism has the fractional form of equation (3.8). Then host and parasitoid persistence can be determined from the fixed points and stability of

$$\bar{n}_{t+1} = \Phi_n \bar{n}_t u(\bar{n}_t, \bar{p}_t) = \Phi_n \left[\frac{R_0 \bar{n}_t}{1 + (R_0 - 1)\bar{n}_t}\right] \left(\frac{1}{1 + \bar{p}_t}\right), \tag{3.42a}$$

$$\bar{p}_{t+1} = \Phi_p \bar{p}_t v(\bar{n}_t, \bar{p}_t) = \Phi_p b \left[\frac{R_0 \bar{n}_t}{1 + (R_0 - 1)\bar{n}_t}\right] \left(\frac{\bar{p}_t}{1 + \bar{p}_t}\right). \tag{3.42b}$$

The three fixed points of system (3.42) are the extinction equilibrium, $(0, 0)$, the exclusion equilibrium,

$$(\bar{n}, \bar{p}) = \left(\frac{\Phi_n R_0 - 1}{R_0 - 1}, 0\right), \tag{3.43}$$

and the coexistence equilibrium,

$$(\bar{n}, \bar{p}) = \left(\frac{\Phi_n}{b\Phi_p}, \frac{bR_0\Phi_n\Phi_p - b\Phi_p + (1 - R_0)\Phi_n}{b\Phi_p + (R_0 - 1)\Phi_n}\right). \tag{3.44}$$

The dynamics of system (3.42) are determined by the parameters R_0, b, and the dispersal-survival proportions, Φ_n and Φ_p. The extinction equilibrium, (0,0), is asymptotically stable if $\Phi_n R_0 < 1$. The exclusion equilibrium, point (3.43), is asymptotically stable if $\Phi_n R_0 > 1$

and

$$b\Phi_p < \frac{\Phi_n(R_0-1)}{\Phi_n R_0 - 1}. \tag{3.45}$$

The coexistence equilibrium, point (3.44), is asymptotically stable if $\Phi_n R_0 > 1$ and

$$b\Phi_p > \frac{\Phi_n(R_0-1)}{\Phi_n R_0 - 1}. \tag{3.46}$$

Details for the stability analysis are given in Appendix 3.10. Based on the non-spatial difference equation previously studied in [59], I assume $R_0 > 1$ and $b > 1$. Additionally, note that $0 < \Phi_n < 1$ and $0 < \Phi_p < 1$ by definition.

Parasitoid extinction occurs when the coexistence equilibrium loses stability and the exclusion equilibrium gains stability. The host dies out when the exclusion equilibrium loses stability and the extinction equilibrium gains stability.

Note that Φ_n and Φ_p will depend on c, L, δ_n, and δ_p. To find the critical speed, c^*, for the parasitoid population, one can numerically solve

$$b\Phi_p = \frac{\Phi_n(R_0-1)}{\Phi_n R_0 - 1} \tag{3.47}$$

for fixed R_0, b, L, δ_n, and δ_p. For each approximation method for Φ_n and Φ_p, I compare the resulting parasitoid critical speed to the critical speed found from simulations in Section 3.6.1.

3.5.2 Dominant eigenvalue approximations

Average dispersal success

First, consider average dispersal success from equation (3.40), defined as

$$S = \frac{1}{L}\int_{-L/2}^{L/2}\int_{-L/2}^{L/2}\frac{1}{2\delta}e^{-|x+c-y|/\delta}dxdy \tag{3.48}$$

for the Laplace kernel. This evaluates as

$$S = \begin{cases} 1 - \frac{c}{L} - \frac{\delta}{L}\left[e^{-c/\delta} - e^{-L/\delta}\cosh(c/\delta)\right], & c < L \\ \frac{\delta}{L}e^{-c/\delta}\left[\cosh(L/\delta) - 1\right], & c \geq L \end{cases}. \tag{3.49}$$

Modified dispersal success approximation

Next consider the modified dispersal success approximation, $\hat{S}$, from Reimer et al. [77]. For an asymmetrical kernel,

$$\hat{S} = \frac{1}{|\Omega|}\frac{1}{S}\int_{\Omega} r(y)s(y)dy, \tag{3.50}$$

where S is average dispersal success, $r(y)$ is the redistribution function [58],

$$r(y) = \int_{\Omega} k(y,z)dz, \tag{3.51}$$

and $s(y)$ is the dispersal success function [95],

$$s(y) = \int_{\Omega} k(z,y)dz. \tag{3.52}$$

For the Laplace kernel with a habitat interval of length L centered at 0, the modified dispersal success approximation is

$$\hat{S} = \frac{1}{L}\frac{1}{S}\int_{-L/2}^{L/2}\left(\int_{-L/2}^{L/2}\frac{1}{2\delta}e^{-|y+c-x|/\delta}dx\right)\left(\int_{-L/2}^{L/2}\frac{1}{2\delta}e^{-|x+c-y|/\delta}dx\right)dy. \tag{3.53}$$

This is a piecewise function, depending on the relationship between c and L. For $c \geq L$,

$$\hat{S} = \frac{1}{4S}\left[e^{-(2c+L)/\delta}\left(e^{L/\delta} - 1\right)^2\right]. \tag{3.54}$$

For $c < 2c \leq L$,

$$\hat{S} = \frac{\delta}{4LS}\left[\begin{array}{c} e^{-L/\delta} - e^{-2L/\delta} - 4e^{-c/\delta} + 4e^{-(c+L)/\delta} + \frac{L}{\delta}e^{-(2c+L)/\delta} \\ -\left(3 + \frac{2c}{\delta}\right)e^{-2c/\delta} + \left(3 - \frac{2c}{\delta} + \frac{L}{\delta}\right)e^{(2c-L)/\delta} + \frac{4}{\delta}(L-2c) \end{array}\right]. \tag{3.55}$$

For $c < L < 2c$,

$$\hat{S} = \frac{\delta}{4LS}\left[\begin{array}{c} e^{-L/\delta} - e^{-2L/\delta} - 4e^{-c/\delta} + 4e^{-(c+L)/\delta} + \frac{L}{\delta}e^{-(2c+L)/\delta} \\ - \left(3 + \frac{2c}{\delta}\right)e^{-2c/\delta} + \left(3 + \frac{2c}{\delta} - \frac{L}{\delta}\right)e^{-(2c-L)/\delta} \end{array}\right]. \tag{3.56}$$

Geometric symmetrization

Following Kot and Phillips [48] and Rinnan [79, 80], I define geometric symmetrization of the average dispersal success as

$$G = \frac{1}{|\Omega|}\int_\Omega \int_\Omega \sqrt{k(x + c - y)k(y + c - x)}dxdy. \tag{3.57}$$

For short, I will refer to this simply as "geometric symmetrization."

For the Laplace kernel on a habitat interval of length L centered at 0, this is

$$G = \frac{1}{2\delta L}\int_{-L/2}^{L/2}\int_{-L/2}^{L/2} e^{-\frac{1}{2\delta}|x+c-y|}e^{-|y+c-x|/(2\delta)}dxdy. \tag{3.58}$$

The geometric symmetrization with the Laplace kernel evaluates as

$$G = \begin{cases} \frac{1}{L}e^{-c/\delta}\left[\frac{-1}{2\delta}c^2 + \left(\frac{L}{\delta} - 1\right)c + L - \delta\right] + \frac{\delta}{L}e^{-L/\delta}, & c < L \\ \frac{L}{2\delta}e^{-c/\delta}, & c \geq L \end{cases}. \tag{3.59}$$

The primary benefit of this approximation is that the kernel in equation (3.57) is symmetric and more robust to increased climate velocity. Kot and Philips [48] and Rinnan [79] showed that geometric symmetrization provides a relatively tight lower bound for the critical speed for a single-species moving-habitat IDE model. Lutscher [57] gives a heuristic explanation for why geometric symmetrization provides a good approximation to the dominant eigenvalue of the original IDE, but also notes that finding a rigorous connection between the original IDE problem and the geometric symmetrization is an open question.

Maximum and minimum row-sums

The simplest bounds on the spectral radius of nonnegative matrix $\mathbf{K}$ are based on the row sums of the matrix. Let r_i be the ith row sum of $\mathbf{K}$, defined as

$$r_i = \sum_{j=1}^{N} k_{ij}, \tag{3.60}$$

where $\mathbf{K} = (k_{ij})$. Then

$$\min_i r_i \leq \rho(\mathbf{K}) \leq \max_i r_i, \tag{3.61}$$

where $\rho(\mathbf{K})$ is the spectral radius of nonnegative matrix $\mathbf{K}$. This is a classic result from Frobenius [28].

The analytic equivalent of these bounds for the spectral radius of the original integral operator K from equation (3.41) with the habitat-shifted kernel is

$$\min_{x\in\Omega} r(x) = \min_{x\in\Omega} \int_\Omega k(x+c-y)dy \leq \rho(K) \leq \max_{x\in\Omega} \int_\Omega k(x+c-y)dy = \max_{x\in\Omega} r(x), \tag{3.62}$$

where $r(x)$ is the redistribution function, equation (3.51). The analytic version of this method has a computational advantage over the numeric version if the integrals can be computed analytically. However, the next method builds on the matrix version of maximum and minimum row-sums, so I use the numeric version described by (3.61) to build towards the iterated method discussed next.

Iterated maximum and minimum row-sums

One can also find increasingly tight bounds on the spectral radius of nonnegative $\mathbf{K}$ beginning with a result from Minc [63]. For a nonnegative matrix with nonzero row-sums,

$$\min_i r_i \leq \min_i \left(\frac{1}{r_i} \sum_{j=1}^{N} k_{ij} r_i \right) \leq \rho(\mathbf{K}) \leq \max_i \left(\frac{1}{r_i} \sum_{j=1}^{N} k_{ij} r_i \right) \leq \max_i r_i. \tag{3.63}$$

Yeh [104] built on result (3.63) to develop an iterative set of bounds on the spectral radius of $\mathbf{K}$. First, she defines $\mathbf{K}^{(0)} = \mathbf{K} = \left(k_{ij}^{(0)}\right)$. Then, let $\mathbf{D^{(0)}}$ be the diagonal matrix with the ith row sum of $\mathbf{K}$ as the ith element of the diagonal of $\mathbf{D}$. At each iteration for $m = 0, 1, 2, ...$, define

$$\mathbf{K}^{(m+1)} = \left[\mathbf{D}^{(m)}\right]^{-1} \mathbf{K}^{(m)}\mathbf{D}^{(m)} \equiv \left[k_{ij}^{(m+1)}\right], \tag{3.64}$$

where $\mathbf{D}^{(m)}$ is the diagonal matrix with the ith row sum of matrix $\mathbf{K}^{(m-1)}$ as the ith entry on the diagonal of $\mathbf{D}^{(m)}$. From this sequence of matrices, define the sequence

$$r_i^{(0)} = \sum_{j=1}^{N} k_{ij}^{(0)} = r_i, \tag{3.65a}$$

$$r_i^{(m+1)} \equiv \sum_{j=1}^{N} k_{ij}^{(m+1)} = \frac{1}{r_i^{(m)}} \sum_{j=1}^{N} k_{ij}^{(m)} r_j^{(m)}. \tag{3.65b}$$

Yeh [104] proved that for each m,

$$\min_i r_i^{(m)} \leq \min_i r_i^{(m+1)} \leq \rho(\mathbf{K}) \leq \max_i r_i^{(m+1)} \leq \max_i r_i^{(m)}, \tag{3.66}$$

such that the sequences $\{\min_i r_i^{(m)}\}$ and $\{\max_i r_i^{(m)}\}$ converge, providing tighter bounds on $\rho(\mathbf{K})$ as m increases.

Kot and Phillips [48] used Yeh's iterated row-sums with a numerical root finder to attain upper and lower bounds for the critical speed for the single-species moving-habitat IDE. For certain parameter values, several iterates of Yeh's method were needed to get reasonable bounds for the critical speed.

Iterated geometric symmetrization

The analytic expression for geometric symmetrization, equation (3.57) was originally based on geometric symmetrization of an asymmetric matrix [48]. For an asymmetric nonnegative matrix $\mathbf{K}$, Schwenk [84] defined the matrix $\mathbf{G}$ as the unique matrix such that

$$\mathbf{G} \circ \mathbf{G} = \mathbf{K} \circ \mathbf{K}^T, \tag{3.67}$$

where $\circ$ represents the elementwise-product of the two matrices (the Hadamard product) and $\mathbf{K}^T$ is the transpose of $\mathbf{K}$. Equivalently, the elements of $\mathbf{G}$ are

$$g_{ij} = \sqrt{k_{ij}k_{ji}}. \tag{3.68}$$

I will refer to $\mathbf{G}$ as the matrix geometric symmetrization. Importantly, $\mathbf{G}$ is symmetric and

$$\rho(\mathbf{G}) \leq \rho(\mathbf{K}). \tag{3.69}$$

While $\rho(\mathbf{G})$ provides a lower bound on the spectral radius of $\mathbf{K}$, the analytic geometric symmetrization expression from equation (3.57) is significantly computationally faster to compute for the Laplace kernel than $\rho(\mathbf{G})$.

Kolotilina [44] built on Schwenk's result and provided a sequence of increasingly tight lower bounds on $\rho(\mathbf{K})$, based on the Rayleigh quotient with vector $\mathbf{e} = (1, 1, ..., 1)^T$. This sequence is

$$\frac{\mathbf{e}^T\mathbf{G}\mathbf{e}}{N} \leq \left(\frac{\mathbf{e}^T\mathbf{G}_2\mathbf{e}}{N}\right)^{1/2} \leq \cdots \leq \left(\frac{\mathbf{e}^T\mathbf{G}_{2^m}\mathbf{e}}{N}\right)^{1/2^m} \leq \rho(\mathbf{K}), \tag{3.70}$$

where $\mathbf{G}_{2^m}$ is the geometric symmetrization of $\mathbf{K}^{2^m}$. As a note of caution, this expression is misstated in [48] as being based on powers of matrix $\mathbf{G}$. The correct expressions are in terms of the geometric symmetrization matrices of powers of $\mathbf{K}$, as written in [44, 79]. Rinnan [79] also provides a sequence of analytic geometric symmetrization expressions based on recursively-defined kernels with increasingly many nested integrals.

For the purposes of this chapter, I will compare the use of iterated geometric symmetrization, (3.70), in difference-equation system (3.42) with the previously mentioned approximations.

3.5.3 Simulations

The Case 2 IDE system can be numerically simulated using either system (3.20) from the observer's perspective or system (3.24) from the moving-habitat frame of reference. As c

increases for a given set of biological parameters, the total population of the parasitoid's steady state decreases. For some speeds, the steady state of the parasitoid distribution is very small. For slightly larger speeds, the parasitoid population slowly declines over time and asymptotically dies out. To determine the critical speed from simulations, it is necessary to distinguish between asymptotic survival at small values and asymptotic extinction.

To explore how many generations or iterations are necessary to determine whether the parasitoid population survives for a given c, I ran simulations for a range of c values and calculated the maximum parasitoid-density after 200 iterations up to 4000 iterations, in intervals of 200 iterations. The results for a set of biological parameters are shown in Figures 3.6 and 3.7.

Figure 3.6 shows that as c increases, the maximum parasitoid-density initially decreases slowly. For sufficiently small c, the maximum parasitoid-density after 200 iterations is indiscernible from the maximum parasitoid-density after 4000 iterations. As c continues to increase, the maximum parasitoid-density drops off sharply, and the maximum parasitoid-density after 200 iterations is very different from the maximum parasitoid-density after 4000 iterations.

Figure 3.7 zooms in on a range of c values near the sharp drop-off. Based on simulations like this one for various sets of parameters, one can reasonably conclude that if the maximum parasitoid-density is below 10^{-3} after 1000 iterations, then the population will die out asymptotically. Technically, this definition of critical speed is an upper bound on the critical speed from simulations, but it provides a significantly more precise metric than has been previously used [80].

For all critical speeds from simulations in Section 3.6, I used a bisection method to find the smallest c for which the maximum parasitoid-density was below 10^{-3} after 1000 iterations. Numerical simulations for these results used the moving-habitat frame, system (3.24), for simulations, which is much more computationally efficient than simulating with

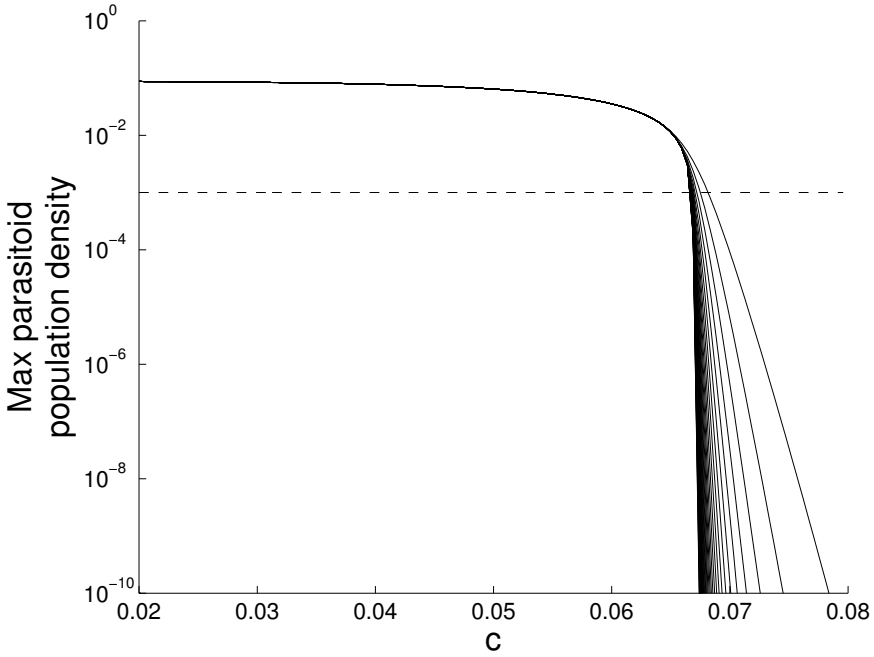

Figure 3.6: Maximum parasitoid population density with respect to c after a certain number of iterations. The number of iterations plotted here starts at 200 (upper right line) and increases to 4000 iterations (the lowest left line). Biological parameters were $L = 1$, $R_0 = 2$, $b = 3$, $\delta_n = 0.4$, $\delta_p = 1/15$. The horizontal dashed line is at 10^{-3} to indicate the cutoff used in this chapter to distinguish between persistence at small values and extinction.

the observer's frame of reference, system (3.20) . Numerically simulating with system (3.24) restricts the values of c to integer multiples of the grid spacing, dx. For the simulations in Section 3.6, I used $dx = 2^{-11} \approx 4.88 \times 10^{-4}$. The integrals at each iteration were computed using `MATLAB`'s built-in '`conv`' function. For additional discussion of numerical simulations of IDEs, see [57].

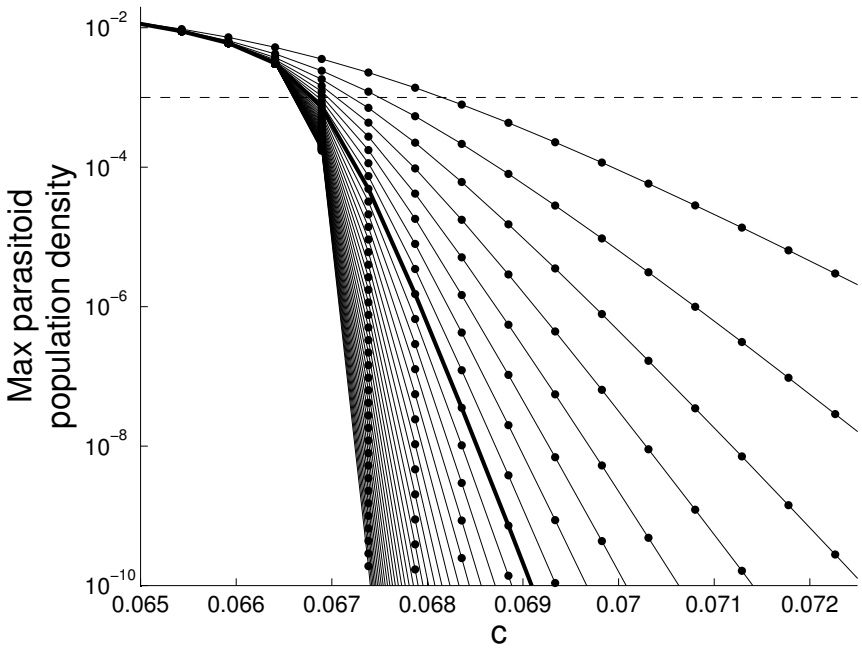

Figure 3.7: Maximum parasitoid population density with respect to c after a certain number of iterations. The number of iterations plotted here starts at 200 (upper right line) and increases to 4000 iterations (the lowest left line). Biological parameters were $L = 1$, $R_0 = 2$, $b = 3$, $\delta_n = 0.4$, $\delta_p = 1/15$. The horizontal dashed line is at 10^{-3} to indicate the cutoff used in this chapter to distinguish between persistence at small values and extinction. The thicker line is the maximum parasitoid population density after 1000 iterations. The critical speed for this chapter is defined as the first speed for which the maximum parasitoid population density is below 10^{-3} after 1000 iterations.

3.6 Case 2 results

In this section, I compare the parasitoid critical speeds from each of the methods discussed in Section 3.5. I also compare the critical speed predicted by Case 1 with the critical speed for Case 2. Finally, I discuss the impact of biological parameters on the parasitoid critical speed.

3.6.1 Critical speed for parasitoid survival: Compare approximations with simulations

In order to compare the methods presented in Section 3.5.2, I computed parasitoid critical speeds predicted by each method for numerous combinations of parameters. Critical speeds for some of these trials are shown in Figures 3.8, 3.9, and 3.10.

Each figure also shows the critical speeds from simulations with specific parameter values. Simulations are computationally intensive and also cannot run with a sufficiently small dx on a laptop with 16 GB of memory. Calculating critical speeds for 50 sets of parameters took over five hours on an external server.

All approximation methods were faster than determining critical speed from simulations. Recall from Section 3.5.2 that average dispersal success, S, Reimer et al.'s [77] modification, $\hat{S}$, and geometric symmetrization, G, can be computed directly for the Laplace kernel. This means that these three methods have a computational advantage over other methods, since critical speed can be easily and quickly computed on a laptop. For sufficient accuracy, numerically computed approximations including matrix row-sums, Yeh's [104] iterated row-sums, and iterated geometric symmetrization could not be computed on a laptop due to insufficient memory. Each of these methods nevertheless ran faster than simulations on an external server.

For complete disclosure, the integrals for the analytic version of the row-sum method from the inequalities in (3.62) can be evaluated for the Laplace kernel. Using those expressions to compute critical speed would have the same computational advantage as the other analytic

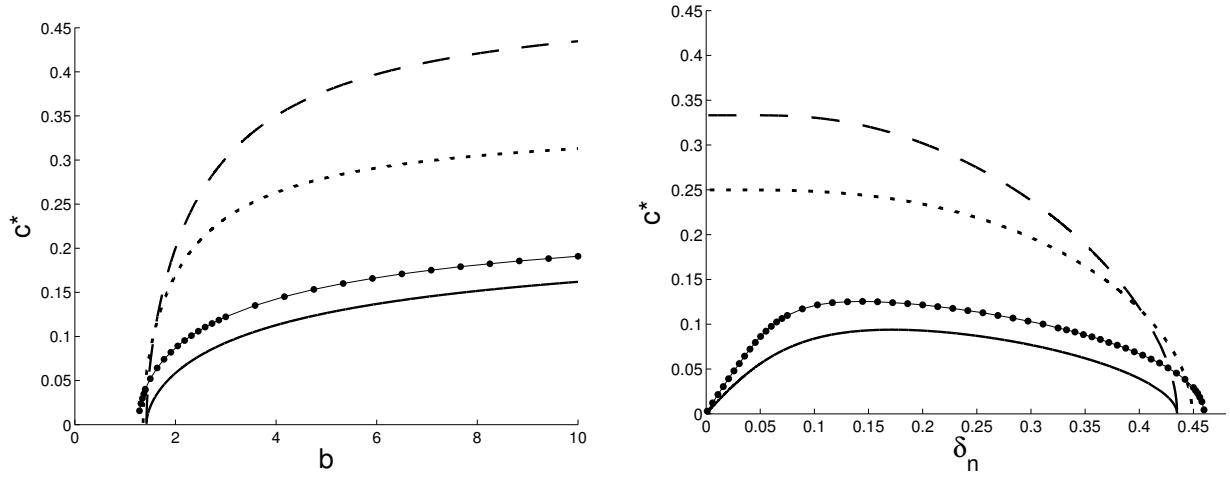

Figure 3.8: A comparison of the approximated critical speed from geometric symmetrization (solid), average dispersal success (dashed), and Reimer et al.'s modification to average dispersal success (dotted). The critical speed from simulations is shown with connected markers. Biological parameters were $L = 1$, $R_0 = 2$, and $\delta_p = 1/15$ for both figures, $\delta_n = 1/5$ for the left figure, and $b = 3$ for the right figure. Note that geometric symmetrization gives a lower bound for the critical speed. Both average dispersal success and Reimer et al.'s modification greatly overestimate the critical speed for most parameters, but underestimate for some parameters.

methods compared here.

For all parameter ranges, geometric symmetrization resulted in a lower bound for the parasitoid critical speed that qualitatively matched the critical speed from the simulation method as parameters were varied. The lower bound from geometric symmetrization is not particularly tight, but it is tight enough to be useful as a conservative estimate on the maximum climate velocity that a parasitoid population could withstand.

In Figure 3.8, I show some of the results from using average dispersal success, Reimer

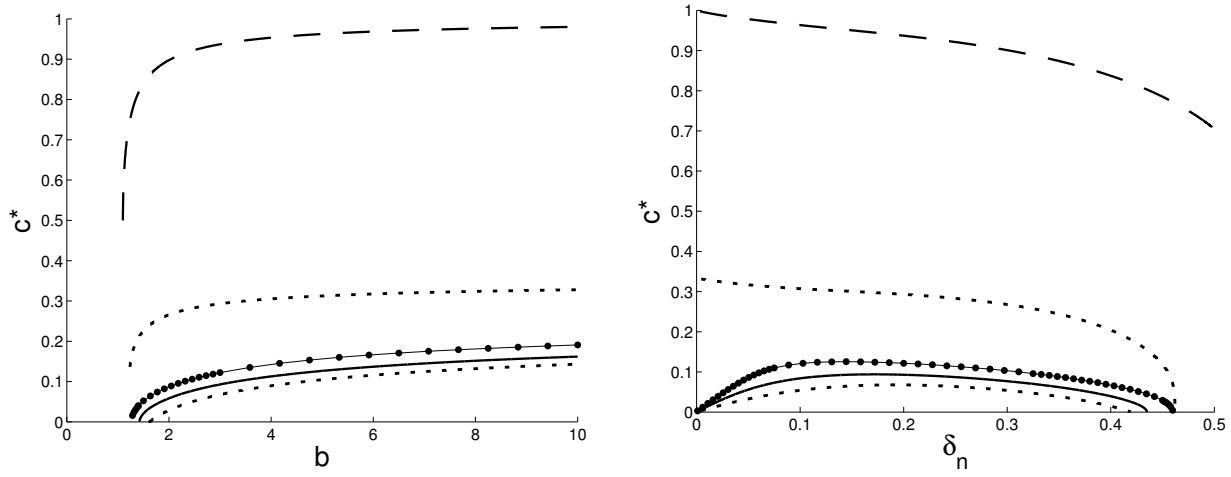

Figure 3.9: A comparison of the approximated critical speed from geometric symmetrization (solid), maximum row-sums (dashed), and two iterations of Yeh's iterated maximum and minimum row-sums (dotted). The critical speed from simulations is shown with connected markers. Biological parameters were $L = 1$, $R_0 = 2$, and $\delta_p = 1/15$ for both figures, $\delta_n = 1/5$ for the left figure, and $b = 3$ for the right figure. Note that geometric symmetrization gives a lower bound for the critical speed. The critical speed from the maximum row-sum method has huge error, but is an upper bound. Yeh's iterated maximum and minimum row-sums method gives an upper and lower bound, though the geometric-symmetrization method gives a tighter lower bound than two iterations of Yeh's iterated minimum row-sums.

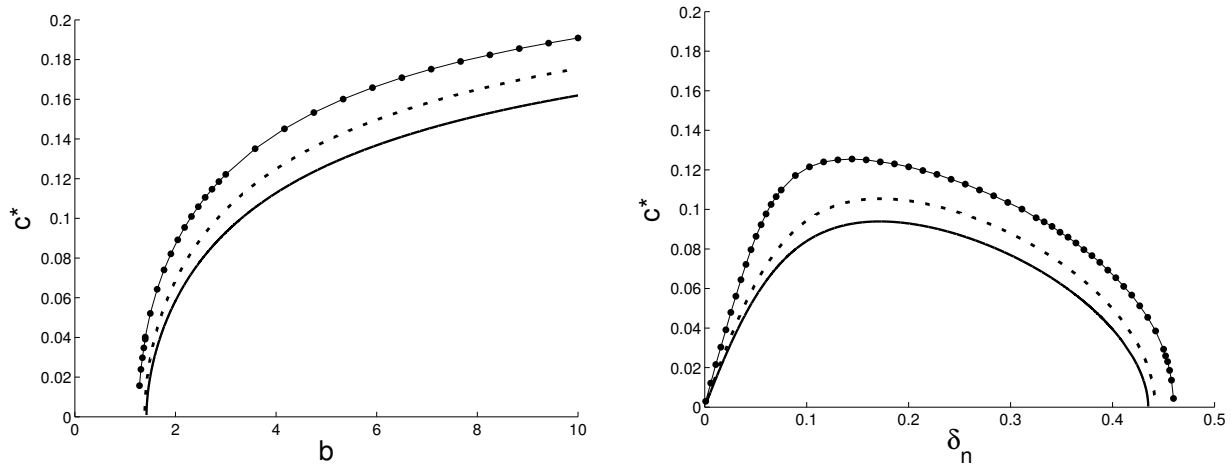

Figure 3.10: A comparison of the approximated critical speed from geometric symmetrization (solid) and one iteration of iterated geometric symmetrization (dotted). The critical speed from simulations is shown with connected markers. Biological parameters were $L = 1$, $R_0 = 2$, and $\delta_p = 1/15$ for both figures, $\delta_n = 1/5$ for the left figure, and $b = 3$ for the right figure. Both geometric symmetrization and iterated geometric symmetrization give lower bounds for the critical speed. Iterated geometric symmetrization is a tighter lower bound, but is more computationally and memory intensive.

et al.'s modification to average dispersal success, and geometric symmetrization. For most sets of parameters, both average dispersal success and Reimer et al.'s modification vastly overestimated the critical speed. For select parameter ranges with low b, low R_0, and/or high host and parasitoid average dispersal distances, δ_n and δ_p, average dispersal success and Reimer et al.'s modification decently estimated critical speed. Neither method always overestimated the critical speed, so neither method is an upper bound. For most sets of parameters, geometric symmetrization yields a better approximation to the critical speed from simulations. Of these three approximations, only geometric symmetrization qualitively captures the effect of each biological parameter on the critical speed.

Figure 3.9 compares the parasitoid critical speeds determined by using maximum matrix row-sums, two iterations of Yeh's iterated maximum and minimum row-sums, and geometric symmetrization. Approximating dominant eigenvalues with the minimum row-sum predicted parasitoid death for $c = 0$, so this method was useless. The maximum row-sum approximation always drastically overestimated parasitoid critical speed. The critical speeds resulting from two iterations of Yeh's iterated maximum and minimum row-sums provided upper and lower bounds on the critical speed. The lower bound from iterated minimum row-sums is tighter than the upper bound from maximum iterated row-sums. Geometric symmetrization produces a tighter bound than the lower bound from two iterations of Yeh's minimum iterated row-sums, so geometric symmetrization is still the preferable approximation method.

Finally, in Figure 3.10, I show some of the comparisons of geometric symmetrization and one iteration of iterated geometric symmetrization. Both approximations provide lower bounds on the parasitoid critical speed, and iterated geometric symmetrization gives a tighter bound. Iterated geometric symmetrization is based on the discretization from Section 3.3.1. For sufficiently small dx, the method cannot run on a laptop with 16 GB of memory. It is also much slower than determining critical speed using the analytic expression for geometric symmetrization for the Laplace kernel.

Overall, geometric symmetrization from equation (3.57) is the most useful approximation for Φ_n and Φ_p to determine the parasitoid critical speed. It provides a relatively tight lower bound and qualitatively matches the critical speed from simulations for varied parameters. For kernels that do not have an explicit expression for geometric symmetrization, iterated geometric symmetrization is the best option, providing a tighter lower bound on the parasitoid critical speed.

3.6.2 Critical speed for parasitoid survival: Compare Case 1 as an upper bound for Case 2

While geometric symmetrization and iterated geometric symmetrization provide nice lower bounds for the parasitoid critical speed, I am also interested in comparing a few upper bounds. In Figure 3.11, I compare critical speed from Case 1 with the critical speed from two iterations of Yeh's iterated maximum row-sums. Since Case 1 describes ideal circumstances for the parasitoid, the critical speed from Case 1 is an upper bound on the critical speed for Case 2. For context, I also include the predicted critical speeds from Reimer et al.'s modification and geometric symmetrization. For sufficiently small δ_p, Case 1 is the best upper bound for most sets of parameters, and it does especially well as R_0 increases. However, for even moderate values of parasitoid average dispersal-distance, δ_p, the Case 1 approximation vastly overestimates the critical speed.

3.6.3 Critical speed for parasitoid survival, coexistence: Using geometric symmetrization

Using geometric symmetrization and equation (3.47), one can study the impact of growth parameters R_0 and b and average dispersal distances δ_n and δ_p on the parasitoid's ability to persist in a moving climate. Figure 3.12 shows critical speeds for parasitoid persistence for a large range of parameter combinations.

Critical speed for parasitoid persistence increases monotonically for increasing R_0. Higher host net reproductive rate, R_0, means that the host population is better able to overcome

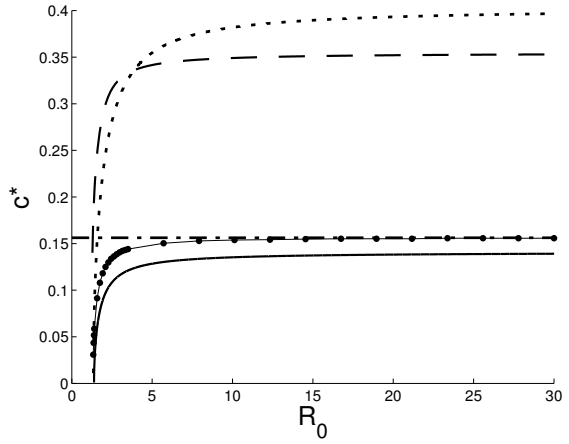

(a) Parasitoid critical speed with $b = 3$, $\delta_n = 1/5$, and $\delta_p = 1/15$,

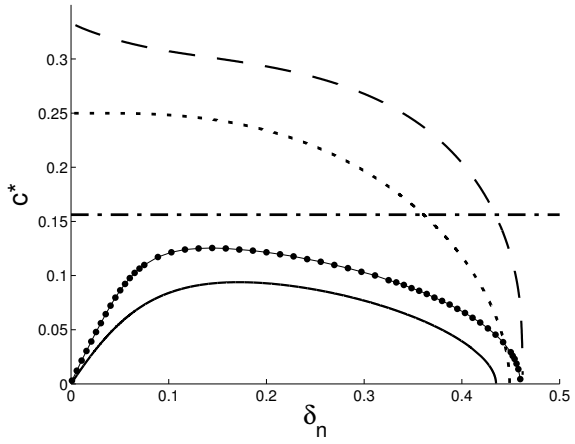

(b) Parasitoid critical speed with $R_0 = 2$, $b = 3$, and $\delta_p = 1/15$,

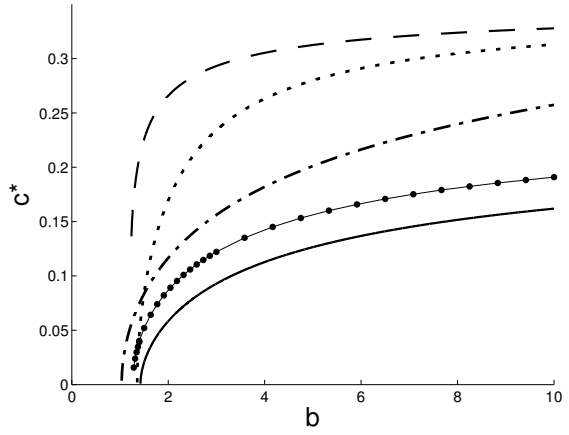

(c) Parasitoid critical speed with $R_0 = 2$, $\delta_n = 1/5$, and $\delta_p = 1/15$,

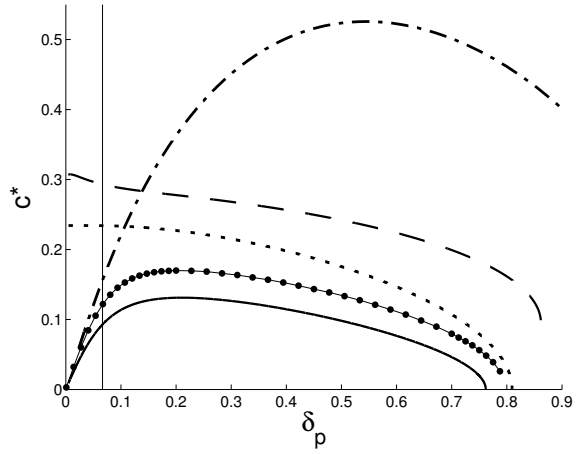

(d) Parasitoid critical speed with $R_0 = 2$, $b = 3$, and $\delta_n = 1/5$.

Figure 3.11: How does Case 1 do as an upper bound for Case 2 parasitoid critical speed? For each figure, the parameter values that are not varied are $L = 1$, $R_0 = 2$, $b = 3$, $\delta_n = 1/5$, and $\delta_p = 1/15$. In each figure, I compare the approximated critical speed from Case 1 (dash-dot line) with the approximated critical speed from Case 2 with geometric symmetrization (solid), Reimer et. al's modification to average dispersal success (dotted), and two iterations of Yeh's iterated maximum row-sums (dashed). The critical speed from the simulation is shown with connected markers. For the chosen fixed parameter values, Case 1 is a tight upper bound for large R_0 values and a decent upper bound for some ranges of δ_n and b. However, there is only a narrower range of δ_p values for which Case 1 is a nice upper bound. In the fourth figure, the vertical line at $\delta_p = 1/15$ shows the fixed value of δ_p that is used in the other figures.

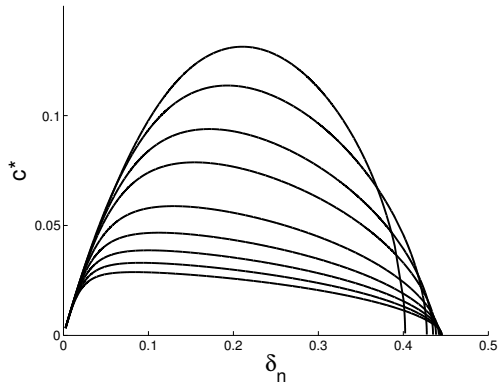

(a) Parasitoid critical speed with $R_0 = 2$, $b = 3$, $L = 1$. From bottom to top, parasitoid average dispersal-distance is $\delta_p = 1/70$, $1/60$, $1/50$, $1/40$, $1/30$, $1/20$, $1/15$, $1/10$, $1/5$.

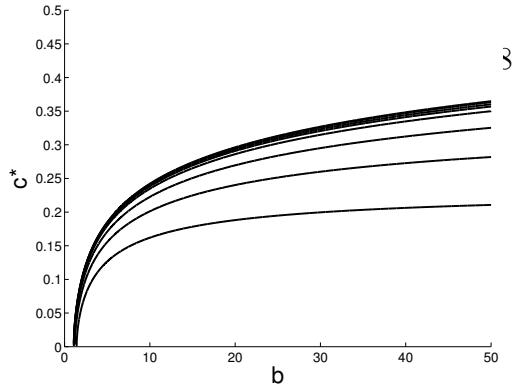

(b) Parasitoid critical speed with $\delta_n = 1/5$, $\delta_p = 1/15$, $L = 1$. From bottom to top, $R_0 = 1.1$, 2, 3, 5, 10, 15, 20, 30, 40.

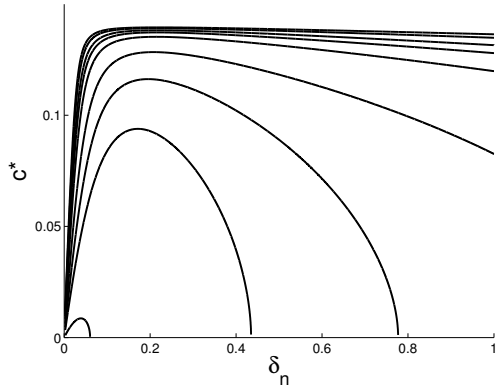

(c) Parasitoid critical speed with $b = 3$, $\delta_p = 1/15$, $L = 1$. From bottom to top, $R_0 = 1.1$, 2, 3, 5, 10, 15, 20, 30, 40.

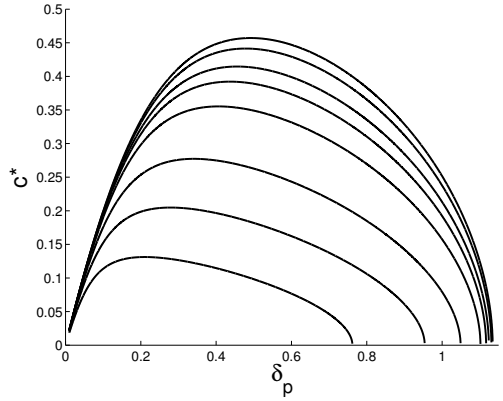

(d) Parasitoid critical speed with $b = 3$, $\delta_n = 1/5$, $L = 1$. From bottom to top, $R_0 = 1.1$, 2, 3, 5, 10, 15, 20, 30, 40.

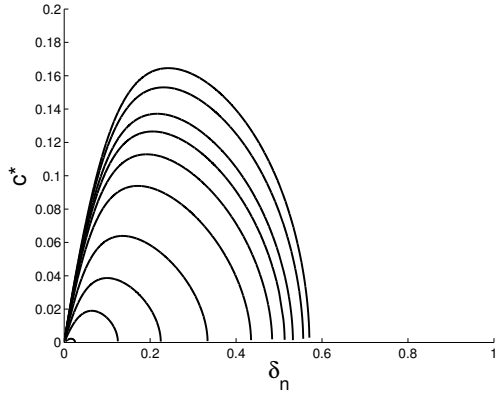

(e) Parasitoid critical speed with $R_0 = 2$, $\delta_p = 1/15$, $L = 1$. From bottom to top, $b = 1.1$, 1.25, 1.5, 2, 3, 4, 5, 6, 8, 10.

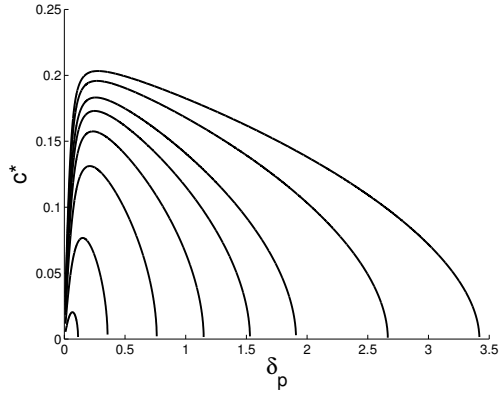

(f) Parasitoid critical speed with $R_0 = 2$, $\delta_n = 1/5$, $L = 1$. From bottom to top, $b = 1.1$, 1.25, 1.5, 2, 3, 4, 5, 6, 8, 10.

Figure 3.12: Parasitoid critical speeds for Case 2. For each set of parameters, I used bisection to find c^* that satisfies equation (3.47) with geometric symmetrization in place of Φ_n and Φ_p.

increasing losses corresponding to increasing climate velocity because more individuals are produced within the patch. Higher host density in the patch provides increased oviposition opportunities for the parasitoid, directly resulting in higher numbers of parasitoid offspring and increasing the parasitoid population's ability to overcome losses due to higher climate velocity. From Figures 3.12b, 3.12c, and 3.12d, it does appear that the benefits of higher R_0 are capped, which makes sense in comparison to Figure 3.11a where Case 1 provides a horizontal line as an upper bound for parasitoid critical speed, independent of the value of R_0.

Critical speed for parasitoid persistence also increases monotonically for increasing b. Recall from Section 3.2 that while b is effectively a parasitoid growth-rate parameter, it is defined as the product of parasitoid searching efficiency, parasitoid clutch size, and host carrying capacity, $b = \alpha\tilde{c}K$. Biologically, more efficient parasitoid searchers are better able to find available hosts and persist on faster-moving habitat patches. Larger clutch size, $\tilde{c}$, directly increases the parasitoid's ability to reproduce and persist. Similarly to R_0, larger host carrying capacity, K, increases hosts available for oviposition and parasitism. Unlike the results for R_0, my explorations show no apparent limit to benefits to parasitoid persistence as b increases.

For both host and parasitoid average dispersal distances, critical speed initially increases with increased average dispersal-distance and then decreases. This suggests that increased dispersal-distance is initially beneficial to the population, but that beyond a certain point, hosts and parasitoids can overdisperse. If the host population overdisperses, the critical speed for parasitoid survival decreases.

The crossing lines for larger values of host dispersal-distance in Figure 3.12a are consistent with a result from Cobbold et al. [18] that for higher host average dispersal-distance, the parasitoid must disperse shorter distances than the host to survive. For shorter host dispersal-distances towards the left of Figure 3.12a, the parasitoid gains an advantage from

dispersing further, and the critical speed increases as δ_p increases.

3.7 Case 3 methods

The Case 3 IDE model, system (3.26), is similar to Case 2, with the added complexity that the host can persist on a larger patch than the parasitoid's patch. I again analyze a spatially-implicit approximation to determine persistence criteria for the parasitoid. After demonstrating the usefulness of geometric symmetrization in comparison to other approximations for the Case 2 critical speed in Section 3.6.1, I specifically use geometric symmetrization for Case 3.

I also compare the critical speeds resulting from geometric symmetrization to those obtained from simulations. For simulations, I use the same methods described in Section 3.5.3. For Case 3 simulations, I define the critical speed, c^*, as the smallest speed for which the maximum parasitoid-density is below 10^{-3} after 1200 iterations. Grid spacing for simulations was $dx = 2^{-11}$, and I again computed the integrals at each iteration with `MATLAB`'s built-in '`conv`' function.

3.7.1 Analysis using population average approach

For Case 3, the host population experiences different dynamics on its patch depending on whether or not a particular part of the patch overlaps the parasitoid's patch. This suggests that the total average host population will have weighted contributions from each of the three sections, where the first interval is $x \in [-L_n/2, -L_p/2]$, the second interval is $x \in [-L_p/2, L_p/2]$, and the third interval is $x \in [L_p/2, L_n/2]$. Recall that these patch sections are in terms of the shifted spatial coordinates in the moving-habitat frame.

Heuristically, the spatially-implicit system of difference equations for Case 3 will have the

form

$$\bar{n}_{t+1} = \Phi_{n_1}\bar{n}_t u(\bar{n}_t, 0) + \Phi_{n_2}\bar{n}_t u(\bar{n}_t, \bar{p}_t) + \Phi_{n_3}\bar{n}_t u(\bar{n}_t, 0), \tag{3.71a}$$

$$\bar{p}_{t+1} = \Phi_p \bar{p}_t v(\bar{n}_t, \bar{p}_t), \tag{3.71b}$$

to reflect the absence of parasitoid reproduction on the sides of the host patch that extend beyond the parasitoid patch. It is now necessary to determine how to connect geometric symmetrization for the host with the weighting coefficients, Φ_{n_1}, Φ_{n_2}, Φ_{n_3}.

Following the method in Section 3.5.1, denote the average of the two populations over their respective patches as

$$\bar{n}_t = \frac{1}{L_n}\int_{-L_n/2}^{L_n/2} n_t(x)dx, \tag{3.72}$$

and

$$\bar{p}_t = \frac{1}{L_p}\int_{-L_p/2}^{L_p/2} p_t(x)dx, \tag{3.73}$$

where L_n is the length of the host's patch, L_p is the length of the parasitoid's patch, and $L_p < L_n$. Now compute the average of both sides of the equations in system (3.26). For the host,

$$\begin{aligned}
\bar{n}_{t+1} &= \frac{1}{L_n}\int_{-L_n/2}^{L_n/2} n_{t+1}(x)dx \\
&= \begin{cases}
\dfrac{1}{L_n}\displaystyle\int_{-L_n/2}^{L_n/2}\int_{-L_p/2}^{-L_p/2} k_n(x+c-y)n_t(y)u\left[n_t(y),0\right]dydx \\
\quad +\dfrac{1}{L_n}\displaystyle\int_{-L_n/2}^{L_n/2}\int_{-L_p/2}^{L_p/2} k_n(x+c-y)n_t(y)u\left[n_t(y),p_t(y)\right]dydx \\
\quad +\dfrac{1}{L_n}\displaystyle\int_{-L_n/2}^{L_n/2}\int_{L_p/2}^{L_n/2} k_n(x+c-y)n_t(y)u\left[n_t(y),0\right]dydx,
\end{cases}
\end{aligned} \tag{3.74}$$

and for the parasitoid,

$$\begin{aligned}
\bar{p}_{t+1} &= \frac{1}{L_p}\int_{-L_p/2}^{L_p/2} p_{t+1}(x)dx \\
&= \frac{1}{L_p}\int_{-L_p/2}^{L_p/2}\int_{-L_p/2}^{L_p/2} k_p(x+c-y)p_t(y)v\left[n_t(y),p_t(y)\right]dydx.
\end{aligned} \tag{3.75}$$

I next linearize around $(\bar{n}_t, \bar{p}_t)$ and drop higher order terms. Then

$$\bar{n}_{t+1} = \begin{cases} \bar{n}_t u\left(\bar{n}_t, 0\right) \dfrac{1}{L_n} \displaystyle\int_{-L_n/2}^{L_n/2} \int_{-L_n/2}^{-L_p/2} k_n(x+c-y)dydx \\ \quad + \bar{n}_t u\left(\bar{n}_t, \bar{p}_t\right) \dfrac{1}{L_n} \displaystyle\int_{-L_n/2}^{L_n/2} \int_{-L_p/2}^{L_p/2} k_n(x+c-y)dydx \\ \quad + \bar{n}_t u\left(\bar{n}_t, 0\right) \dfrac{1}{L_n} \displaystyle\int_{-L_n/2}^{L_n/2} \int_{L_p/2}^{L_n/2} k_n(x+c-y)dydx, \end{cases} \tag{3.76a}$$

$$\bar{p}_{t+1} = \bar{p}_t v\left(\bar{n}_t, \bar{p}_t\right) \frac{1}{L_p} \int_{-L_p/2}^{L_p/2} \int_{-L_p/2}^{L_p/2} k_p(x+c-y)dydx, \tag{3.76b}$$

which is equivalent to

$$\bar{n}_{t+1} = \begin{cases} \bar{n}_t u\left(\bar{n}_t, 0\right) \dfrac{1}{L_n} \displaystyle\int_{-L_n/2}^{-L_p/2} \int_{-L_n/2}^{L_n/2} k_n(x+c-y)dxdy \\ \quad + \bar{n}_t u\left(\bar{n}_t, \bar{p}_t\right) \dfrac{1}{L_n} \displaystyle\int_{-L_p/2}^{L_p/2} \int_{-L_n/2}^{L_n/2} k_n(x+c-y)dxdy \\ \quad + \bar{n}_t u\left(\bar{n}_t, 0\right) \dfrac{1}{L_n} \displaystyle\int_{L_p/2}^{L_n/2} \int_{-L_n/2}^{L_n/2} k_n(x+c-y)dxdy, \end{cases} \tag{3.77a}$$

$$\bar{p}_{t+1} = \bar{p}_t v\left(\bar{n}_t, \bar{p}_t\right) \frac{1}{L_p} \int_{-L_p/2}^{L_p/2} \int_{-L_p/2}^{L_p/2} k_p(x+c-y)dxdy, \tag{3.77b}$$

after changing the order of integration for each double integral. Each of the integrals in equation (3.77a) for $\bar{n}_{t+1}$ is similar to the expression for average dispersal success from equation (3.40), but differs due to different integration limits.

I now seek to incorporate geometric symmetrization, recognizing the asymmetry of the kernels in system (3.77). Using the definition of geometric symmetrization in equation (3.57), geometric symmetrizations for the host and parasitoid are

$$G_n = \frac{1}{L_n} \int_{-L_n/2}^{L_n/2} \int_{-L_n/2}^{L_n/2} \sqrt{k_n(x+c-y)k_n(y+c-x)}dxdy \tag{3.78}$$

and

$$G_p = \frac{1}{L_p} \int_{-L_p/2}^{L_p/2} \int_{-L_p/2}^{L_p/2} \sqrt{k_p(x+c-y)k_p(y+c-x)}dxdy. \tag{3.79}$$

To address the three different regions within the host patch, define

$$G_{n_1} = \frac{2}{L_n - L_p} \int_{-L_n/2}^{-L_p/2} \int_{-L_n/2}^{L_n/2} \sqrt{k_n(x+c-y)k_n(y+c-x)}dxdy, \tag{3.80}$$

$$G_{n_2} = \frac{1}{L_p} \int_{-L_p/2}^{L_p/2} \int_{-L_n/2}^{L_n/2} \sqrt{k_n(x+c-y)k_n(y+c-x)}dxdy, \tag{3.81}$$

and

$$G_{n_3} = \frac{2}{L_n - L_p} \int_{L_p/2}^{L_n/2} \int_{-L_n/2}^{L_n/2} \sqrt{k_n(x+c-y)k_n(y+c-x)}dxdy. \tag{3.82}$$

Then the host's geometric symmetrization (3.78) is

$$G_n = \frac{L_n - L_p}{2L_n} G_{n_1} + \frac{L_p}{L_n} G_{n_2} + \frac{L_n - L_p}{2L_n} G_{n_3}. \tag{3.83}$$

Now, define w to be the proportion of the host patch that is also occupied by the parasitoid. That is,

$$w = \frac{L_p}{L_n}. \tag{3.84}$$

Then the geometric symmetrization for the host is

$$G_n = \frac{1}{2}(1-w)G_{n_1} + wG_{n_2} + \frac{1}{2}(1-w)G_{n_3}. \tag{3.85}$$

Based on equation (3.85) and the limits of integration of G_{n_1}, G_{n_2}, and G_{n_3} in equations (3.80), (3.81), and (3.82), one can replace the double integrals in system (3.77) with geometric symmetrization expressions $\frac{1}{2}(1-w)G_{n_1}$, wG_{n_2}, and $\frac{1}{2}(1-w)G_{n_3}$. System (3.77) is now

$$\bar{n}_{t+1} = \frac{1}{2}(1-w)G_{n_1}\bar{n}_t u\left(\bar{n}_t, 0\right) + wG_{n_2}\bar{n}_t u\left(\bar{n}_t, \bar{p}_t\right) + \frac{1}{2}(1-w)G_{n_3}\bar{n}_t u\left(\bar{n}_t, 0\right), \tag{3.86a}$$

$$\bar{p}_{t+1} = G_p \bar{p}_t v\left(\bar{n}_t, \bar{p}_t\right), \tag{3.86b}$$

where G_p replaces the double integral for the parasitoid equation.

I again assume that the host exhibits compensatory density-dependence and that parasitism is aggregated (with a negative binomial distribution). Then the spatially-implicit system of difference equations to approximate IDE system (3.26) is

$$\bar{n}_{t+1} = \begin{cases} \frac{1}{2}(1-w)G_{n_1}\left[\frac{R_0\bar{n}_t}{1+(R_0-1)\bar{n}_t}\right] + wG_{n_2}\left[\frac{R_0\bar{n}_t}{1+(R_0-1)\bar{n}_t}\right]\left(\frac{1}{1+\bar{p}_t}\right) \\ \quad +\frac{1}{2}(1-w)G_{n_3}\left[\frac{R_0\bar{n}_t}{1+(R_0-1)\bar{n}_t}\right], \end{cases} \tag{3.87a}$$

$$\bar{p}_{t+1} = b\left[\frac{R_0\bar{n}_t}{1+(R_0-1)\bar{n}_t}\right]\left(\frac{p_t}{1+\bar{p}_t}\right)G_p. \tag{3.87b}$$

3.7.2 Fixed points and stability

The simple fixed points of system (3.87) are $(0,0)$ and

$$(\bar{n}^*, \bar{p}^*) = \left(\frac{G_n R_0 - 1}{R_0 - 1}, 0\right). \tag{3.88}$$

Notably, the exclusion equilibrium for Case 3, point (3.88), is the same as the exclusion equilibrium in Case 2.

The coexistence equilibrium for system (3.87) is the solution, $(\bar{n}^*, \bar{p}^*)$, to

$$1 = \frac{1}{2}(1-w)(G_{n_1} + G_{n_3})g(\bar{n}) + wG_{n_2}u(\bar{n},\bar{p}), \tag{3.89a}$$

$$1 = G_p v(\bar{n},\bar{p}). \tag{3.89b}$$

For compensatory density dependence and fractional parasitism, the host coordinate of the coexistence fixed point is the larger of the two solutions, $\bar{n}^*$ to

$$(R_0-1)(\bar{n}^*)^2 + \left[1 - R_0\left(\frac{1-w}{2}\right)(G_{n_1}+G_{n_3}) - \frac{wG_{n_2}}{bG_p}(R_0-1)\right]\bar{n}^* - \frac{wG_{n_2}}{bG_p} = 0. \tag{3.90}$$

After solving for $\bar{n}^*$ from equation (3.90), the parasitoid coordinate of the coexistence fixed point is found by substituting the expression for $\bar{n}^*$ into

$$\bar{p}^* = \frac{bR_0G_p\bar{n}^*}{1+(R_0-1)\bar{n}^*} - 1. \tag{3.91}$$

The expressions for $\bar{n}^*$ and $\bar{p}^*$ are algebraically nightmarish, so I do not write them explicitly here.

For parameter values that are restricted by the context of the IDE problem here, quadratic equation (3.90) has two real distinct roots. Only one of the solutions to equations (3.89) can be in the first quadrant for $R_0 > 1$, shown in Appendix 3.11.3.

Perhaps surprisingly, the stability criteria for the fixed points of spatially-implicit Case 3 system (3.87) can be expressed the same as those for the stability of the fixed points of Case 2 system (3.42). The extinction equilibrium for Case 3 is asymptotically stable if $G_n R_0 < 1$. The exclusion equilibrium, point (3.88), is asymptotically stable if $G_n R_0 > 1$ and

$$bG_p < \frac{G_n(R_0 - 1)}{R_0 G_n - 1}. \tag{3.92}$$

The coexistence equilibrium is asymptotically stable if $G_n R_0 > 1$ and

$$bG_p > \frac{G_n(R_0 - 1)}{G_n R_0 - 1}. \tag{3.93}$$

Details for the stability analysis are given in Appendix 3.11, where I use the Jury [40] conditions and the zero-growth isoclines to determine the stability criteria of the coexistence equilibrium without using the explicit expressions for $\bar{n}^*$ and $\bar{p}^*$.

The primary difference between the stability results for Case 2 and Case 3 is that the geometric symmetrization for Case 3 is the weighted sum of three integrals in order to capture the spatial habitat patch variation that is not present in Case 2. Because of the different limits of integration for G_{n_1} and G_{n_3}, there is not an explicit expression for G_n for the Laplace kernel for Case 3.

Nevertheless, one can still numerically solve

$$bG_p = \frac{G_n(R_0 - 1)}{G_n R_0 - 1}, \tag{3.94}$$

for c^* for given L_n, L_p, b, R_0, δ_n, and δ_p. I compare the resulting parasitoid critical speed to the critical speed found from simulations in Section 3.8.1.

3.8 Case 3 results

In this section, I compare the approximated parasitoid critical speed from geometric symmetrization with the critical speed from simulations. I also compare the critical speed predicted by Case 1 with the critical speed for Case 3. I consider conditions for which the Case 3 spatially-implicit system is a good estimate of the true critical speed and conditions when the Case 1 approximation is useful as an upper bound.

3.8.1 Critical speed for parasitoid survival, coexistence: Compare with simulations

As with Case 2, the spatially-implicit difference-equation system with geometric symmetrization provides a lower bound for the critical speed for Case 3. The geometric symmetrization results again qualitatively mirror the changes in the simulated critical speed as biological parameters are varied, shown for some parameter sets in Figure 3.13.

Due to the three regions within the host patch, there is not an analytic expression for G_n for Case 3. This means that critical speeds for Case 3 take significantly longer to compute than Case 2 critical speeds. Critical speeds from geometric symmetrization for Case 3 can still be computed more quickly than from simulations.

The lower bounds from geometric symmetrization for Case 3 are not particularly tight, but can still be used to investigate trends in critical speed for varied biological parameters. (The impacts of biological parameters on the critical speed for Case 3 are very similar to those discussed in Section 3.6.3 for Case 2.) On the other hand, geometric symmetrization for Case 3 does not have the advantage of analytic expressions that were possible for Case 2. Therefore, it would be worthwhile to develop a version of iterated geometric symmetrization appropriate for the three regions of the Case 3 host patch to compute tighter lower bounds on the parasitoid critical speed.

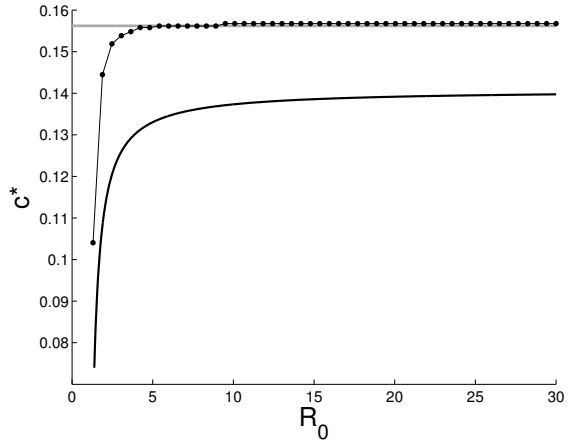

(a) Parasitoid critical speed with $L_n = 2$, $L_p = 1$, $b = 3$, $\delta_n = 1/5$, $\delta_p = 1/15$.

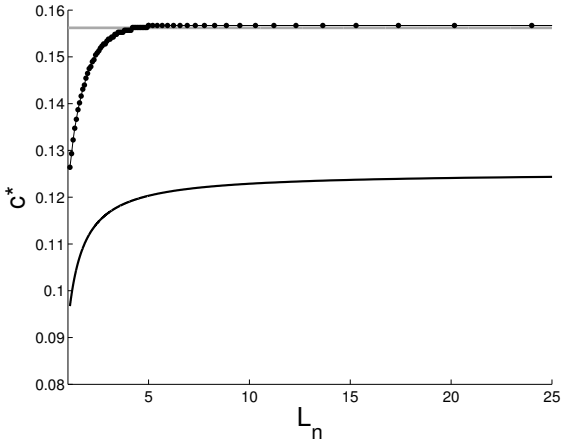

(b) Parasitoid critical speed with $L_p = 1$, $R_0 = 2$, $b = 3$, $\delta_n = 1/5$, $\delta_p = 1/15$.

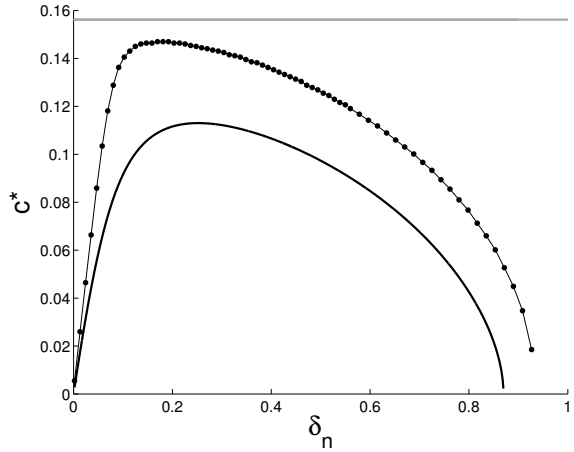

(c) Parasitoid critical speed with $L_n = 2$, $L_p = 1$, $R_0 = 2$, $b = 3$, $\delta_p = 1/15$.

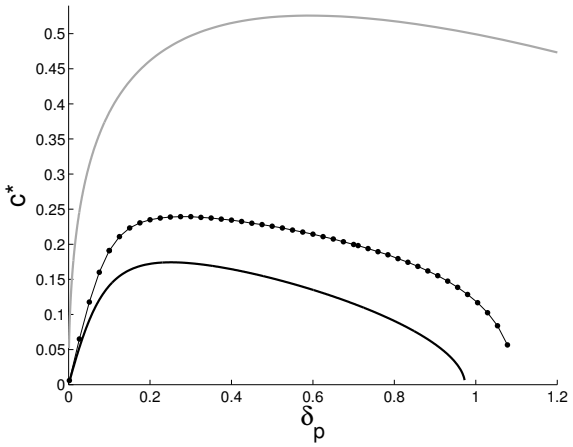

(d) Parasitoid critical speed with $L_n = 2$, $L_p = 1$, $R_0 = 2$, $b = 3$, $\delta_n = 1/5$.

Figure 3.13: Parasitoid critical speeds for Case 3. The results from geometric symmetrization are shown with a solid black line while the Case 1 critical speed is shown in grey. Simulations are shown with connected black markers. Notice that the c^* axis does not start at 0 for Figures 3.13a and 3.13b.

3.8.2 Critical speed for parasitoid survival, coexistence: Compare Case 1 with Case 3 simulations

Figure 3.13 shows critical speeds predicted by geometric symmetrization and simulations for Case 3. I also compare the corresponding Case 1 critical speed. I previously made the claim that the Case 1 critical speed provides an upper bound for parasitoid critical speed for both Cases 2 and 3. A close examination of Figures 3.13a and 3.13b reveals that the critical speed from Case 3 simulations exceeds the critical speed from Case 1, seemingly contradicting the statement that Case 1 provides an upper bound. However, after careful examination, which I explain in the following paragraphs, Case 1 can still be considered an upper bound on the parasitoid's true critical speed.

Recall that the critical speed from simulations, as defined in Sections 3.5.3 and 3.7, is itself only an upper bound on the true parasitoid critical speed. At the simulation-based critical speed where the maximum parasitoid-density falls below 10^{-3} after 1000 iterations for Case 2 or 1100 iterations for Case 3, one can reasonably conclude that the parasitoid population dies out asymptotically. Up to 4000 iterations, simulations have not ruled out the possibility that the parasitoid population also dies out asymptotically for speeds $c^* - \epsilon$ that are slightly smaller than the practically defined critical speed.

Due to computational constraints, the next-smallest speed tested by simulations is $dx = 2^{-11} = \mathcal{O}(10^{-4})$ less than the critical speed. (A finer grid of speeds can be tested with smaller spatial grid spacing at a cost of increased time.) Referring back to Figure 3.7 from Case 2, consider the largest c for which the maximum parasitoid-density did not fall below 10^{-3} after 1000 iterations. For this c value, the maximum parasitoid population did decrease between 200 iterations and 4000 iterations, and it is still possible that the parasitoid species would die out asymptotically at this habitat velocity. Simulations show that the maximum parasitoid-density did not fall below 10^{-3} after 4000 iterations. One cannot reasonably conclude that the population necessarily dies out asymptotically for this value of c, but one also cannot

rule out the possibility that the population does die out asymptotically for a speed $\mathcal{O}(10^{-4})$ below my definition of the critical speed. The same ideas hold true for Case 3 simulations, described in Section 3.7 but not shown. Therefore, I conclude that the definition of the critical speed from simulations of Case 3 has error estimated around $\mathcal{O}(10^{-4})$.

As R_0 or L_n increases, the difference between the critical speed from Case 1 and the critical speed from simulations in Case 3 is $\mathcal{O}(10^{-4})$ for both Figures 3.13a and 3.13b. This difference does not continue increasing as R_0 or L_n increases beyond the ranges shown in Figure 3.13. Since the Case 1 critical speeds are still within $\mathcal{O}(10^{-4})$ of the simulated critical speed for Case 3, which has error in the range of $\mathcal{O}(10^{-4})$, Case 1 can still be considered an upper bound for the true parasitoid critical speed.

3.8.3 Critical speed for parasitoid survival, coexistence: Comparing geometric symmetrization with Case 1

The host patch in Case 3 extends beyond the parasitoid patch. In some sense, Case 3 is intermediary between Case 2, for which the host and parasitoid exist on the same patch, and Case 1, where the host patch is infinite. One would expect that the critical speeds predicted for Case 3 would approach the Case 1 upper bound as R_0 and L_n increase. As seen in Figure 3.13, critical speeds from simulations of Case 3 do approach the Case 1 critical speed as R_0 or L_n increases, but the Case 3 geometric symmetrization critical speeds do not.

In Figure 3.14, I compare critical speeds from geometric symmetrization for Case 3 with critical speeds from Case 1 as the host patch length, L_n, varies with fixed parasitoid patch length, L_p. For Figures 3.14a and 3.14b, I also include the critical speeds from simulations of Case 3. Figures 3.14b and 3.14d are shown in terms of w, which was previously defined as L_p/L_n, the proportion of the host's patch that is also occupied by the parasitoid. The critical speed from geometric symmetrization demonstrates a clear trend of the parasitoid's critical speed increasing as the host's patch-length increases (or equivalently, as w decreases).

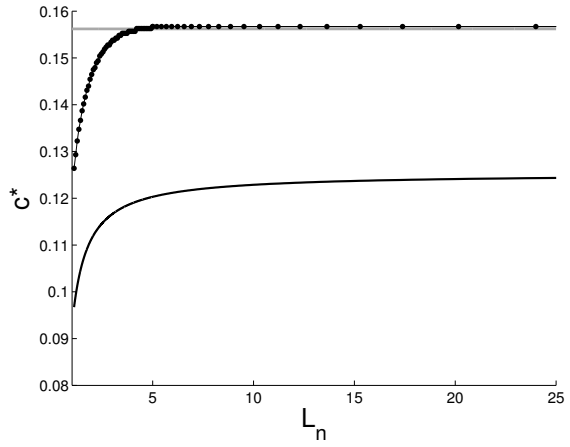

(a) Parasitoid critical speed with $L_p = 1$, $R_0 = 2$, $b = 3$, $\delta_n = 1/5$, and $\delta_p = 1/15$.

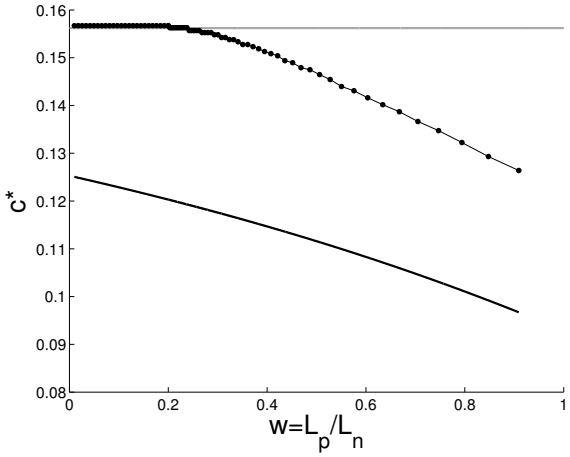

(b) Parasitoid critical speed with $L_p = 1$, $R_0 = 2$, $b = 3$, $\delta_n = 1/5$, and $\delta_p = 1/15$. $w = L_p/L_n$.

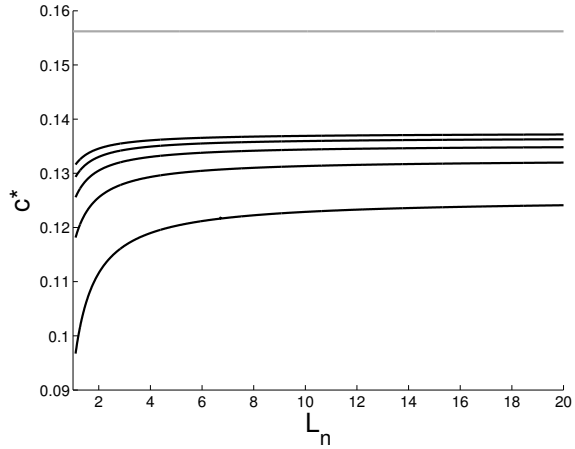

(c) Parasitoid critical speed with $L_p = 1$, $b = 3$, $\delta_n = 1/5$, and $\delta_p = 1/15$.

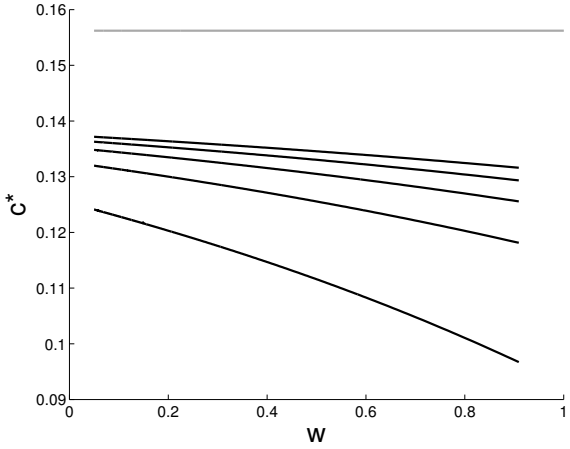

(d) Parasitoid critical speed with $L_p = 1$, $b = 3$, $\delta_n = 1/5$, and $\delta_p = 1/15$. $w = L_p/L_n$.

Figure 3.14: Parasitoid critical speeds for Case 3. Figures 3.14a and 3.14b have a fixed R_0 value and compare critical speed from simulations (connected black markers) with the critical speeds predicted by geometric symmetrization (black) and by Case 1 (grey). Figures 3.14c and 3.14d compare critical speed for Case 3 with geometric symmetrization (black) with values of R_0 from 2 to 6 in integer intervals, from bottom to top. The variable w is defined in equation (3.84) and is the proportion of the host patch that overlaps the parasitoid patch. The predicted critical speed from Case 3 is at best very slowly approaching the Case 1 upper bound as R_0 increases. Notice that the c^* axis does not start at 0.

However, the critical speed predicted by geometric symmetrization does not closely approach the Case 1 upper bound for the scenario with $R_0 = 2$ as L_n increases.

In Figures 3.14c and 3.14d, I consider the critical speeds predicted by Case 3 geometric symmetrization with increasing R_0 with values of R_0 from 2 to 6. While the critical speed increases both as L_n increases and as R_0 increases, the Case 3 geometric symmetrization critical speed does not closely approach the Case 1 speed for biologically reasonable values of R_0.

For smaller parasitoid dispersal-distances with larger R_0 and L_n, Case 1 is a closer estimate than Case 3 geometric symmetrization of the true parasitoid critical speed. Even for fairly large L_n and R_0, Case 3 geometric symmetrization critical speeds do not approach the Case 1 critical speed. When the host's habitat aligns closely with the parasitoid habitat, critical speeds for geometric symmetrization are a better estimate than the critical speed predicted by Case 1 for the parasitoid's true critical speed.

3.9 Discussion

Dynamics of real-world populations are significantly impacted by biotic interactions with other species and available habitat spatially. Integrodifference-equation models have the capacity to model species interactions while explicitly incorporating space, including climate-driven habitat shifts. At the same time, moving-habitat IDE models are rarely analytically tractable, and model analysis must rely on numerical approaches and approximations. Case 1 is a model that reduces the two-species host–parasitoid interactions to the dynamics of only one of the species while explicitly accounting for space. Analysis of Cases 2 and 3 takes the opposite approach: modeling both the host and parasitoid species but implicitly accounting for space. Both approaches can be useful.

As long as parasitoid average dispersal-distance is relatively small, Case 1 provides a decent upper bound on the critical speed for parasitoid persistence for both Cases 2 and 3, IDE

systems (3.20) and (3.25). For most sets of biological parameters, however, a more accurate prediction of parasitoid persistence requires modeling the host–parasitoid interactions in a model for which space is implicit, using difference-equation system (3.42) or (3.87).

Geometric symmetrization gives a lower bound on the parasitoid critical speed that qualitatively matches the true critical speed as biological parameters are varied. Geometric symmetrization is also flexible enough to permit modifications to the habitat assumptions, as was done for Case 3 and in Rinnan's work [80] for two competing species. For Cases 2 and 3 studied here, the lower bound from geometric symmetrization provides a conservative estimate for the maximum climate velocity that a parasitoid species could withstand.

If a more accurate estimate for critical speed is needed for Case 2, a tighter lower bound can be achieved with iterated geometric symmetrization, though at a computational cost. For an upper bound, Case 1 is appropriate for some circumstances or Yeh's iterated maximum row-sums can be used, also at a computational cost. Modification of iterated geometric symmetrization and Yeh's iterated maximum row-sums would be necessary to apply these methods to a scenario like Case 3 with habitat regions not fully overlapping.

Approximating the dynamics of a spatially-explicit model with a spatially-implicit model is certainly not a new idea. Spatially-implicit difference-equation models have been used to approximate IDE models with a network of domain patches [26, 77], habitat fragmentation [58], stage-structured populations [26, 58, 77], alongshore-currents [77], a host–parasitoid system [18], a host–parasitoid system in a patchy landscape [35], and two competing species on a moving habitat [80]. In the complementary realm of continuous-space models, Strohm and Tyson [85] reduced a PDE model for predator and prey dynamics to a system of spatially-implicit ODEs to explore the impact of habitat fragmentation on cyclic population dynamics.

While spatially-implicit models have widespread use, a lingering question remains: What is lost by approximating a spatially-explicit system by a spatially-implicit model? In this chapter, I have explored the conditions for which the parasitoid species persists by looking

at a difference-equation system for the dynamics of average host and parasitoid populations. Simulations reveal that averaging over the patch loses some of the interesting behavior demonstrated by simulations. For example, under certain conditions, the maximum parasitoid-density can actually increase from the maximum density on the stationary habitat patch when the habitat patch moves, as seen in Figure 3.15. A spike or outbreak in the parasitoid population that moves through a landscape with the moving habitat could potentially have consequences for ecosystems and interactions with other species. Transient dynamics and the changing shape of distributions, like those in Figure 3.16 are also not evident from the difference-equation model.

The spatially-implicit approximation techniques used in this chapter nevertheless have many avenues for continued study. Both parasitism and density-dependent effects on the host were modeled with relatively simple functional forms, equations (3.8) and (3.7), corresponding to aggregated parasitism and compensatory density-dependence. For the nonspatial host–parasitoid models studied in [59], Ricker growth [78] and/or an exponential form of parasitism led to wide array of possible dynamics, including population cycles and chaos. It would be interesting to consider how the type of host density-dependence or the level of parasitoid aggregation impacts the persistence of the coexisting host and parasitoid populations. Certain insect species exhibit periodic cycles and outbreaks [96], and the interaction of spiking and dropping population densities over time could certainly complicate a population's ability to persist as its habitat shifts.

Alternately, for koinobiont parasitoids where parasitism occurs during early host larval stages, emergence time of the parasitoid larvae impacts population dynamics [19]. In this chapter, I assumed that density dependence precedes parasitism in the life cycle of the host. Does the relative timing of parasitism in the life cycle of the host affect a parasitoid population's ability to persist as its habitat shifts due to climate change?

All of the results in this chapter assumed a Laplace kernel for dispersal of both the host

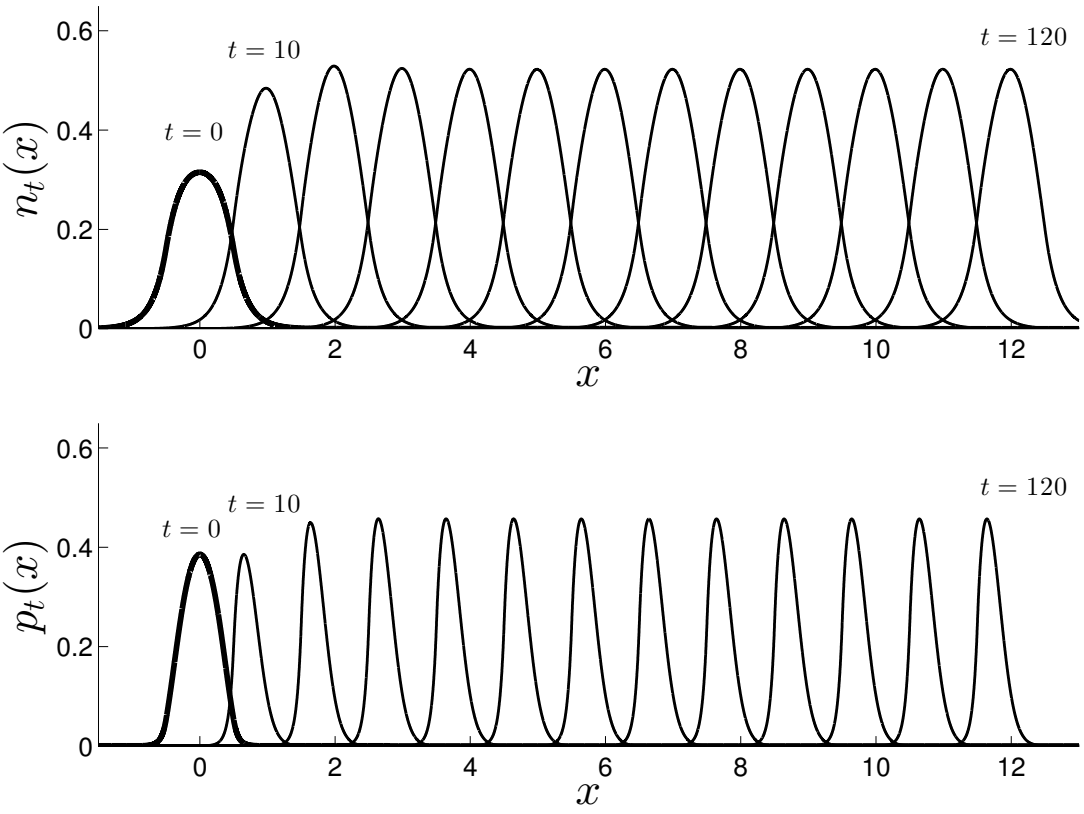

Figure 3.15: A simulation of the population distributions from Case 2 where the host and parasitoid occupy the same habitat that is moving to the right at speed c. These simulations used the same host and parasitoid parameters and set-up as Figure 3.2, but with $c = 0.1$ instead of $c = 0.115$. The population distributions for the moving habitat are shown every 10 generations. After the patch begins moving, the maximum parasitoid-density increases. The total parasitoid population of the steady-state distribution on the moving patch is smaller than the total parasitoid population prior to patch movement.

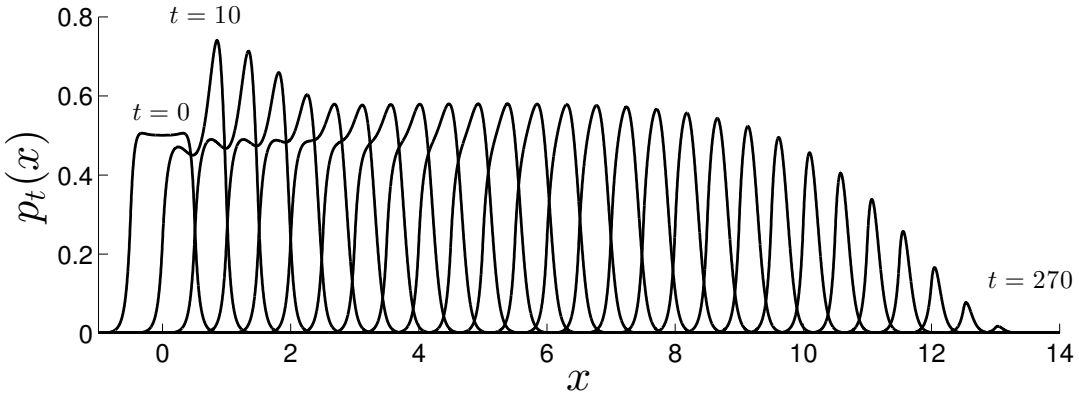

Figure 3.16: A simulation of the parasitoid population distributions from Case 3. This simulation used the same host and parasitoid parameters and set-up as Figure 3.3, but with $c = 0.05$ instead of $c = 0.045$. The population distributions for the moving habitat are shown every 10 generations. The parasitoid population appears to reach a steady state distribution, but this is only a transient phenomena, and the population dies out.

and the parasitoid. For some insect species, kernels with fatter tails than the Laplace kernel have experimentally been shown to better approximate dispersal, especially when individuals can disperse long distances [67]. The results in Sections 3.6 and 3.8 were based on average dispersal-distances for hosts and parasitoids assuming a Laplace dispersal kernel. For a fixed average dispersal-distance, it would be very interesting to consider the impact of tail fatness on the critical speed for host and parasitoid coexistence, building on the single-species results from Zhou and Kot [106].

Finally, this chapter provides additional support for the use of geometric symmetrization for spatially-implicit modeling of IDEs with asymmetric kernels, specifically for two interacting species. Even though an explicit mathematical connection between geometric symmetrization and the dominant eigenvalue of the integral operator is currently an open question [57], geometric systematization provides a valuable tool for modeling species' ability

to persist despite climate-driven habitat shifts.

3.10 Appendix F: Fixed points and stability for Case 2 system of difference equations

The fixed points for the difference-equation approximation for Case 2, system (3.42), are found by setting $\bar{n}_{t+1} = \bar{n}_t = \bar{n}^*$ and $\bar{p}_{t+1} = \bar{p}_t = \bar{p}^*$. Extinction of both species is an equilibrium solution for system (3.42). Additionally, if $\bar{p}^* = 0$, then the equilibrium is found by solving equation (3.42a) for $\bar{n}^*$,

$$1 = \Phi_n u(\bar{n}^*, 0), \tag{3.95}$$

which gives the exclusion equilibrium,

$$(\bar{n}^*, \bar{p}^*) = \left(\frac{\Phi_n R_0 - 1}{R_0 - 1}, 0 \right). \tag{3.96}$$

Finally, the solution to the system

$$1 = \Phi_n u(\bar{n}^*, \bar{p}^*), \tag{3.97a}$$

$$1 = \Phi_p v(\bar{n}^*, \bar{p}^*), \tag{3.97b}$$

is the coexistence equilibrium. For compensatory density-dependence and clumped or aggregated parasitism, the solution to this system is

$$(\bar{n}^*, \bar{p}^*) = \left(\frac{\Phi_n}{\Phi_p} \frac{1}{b}, \frac{bR_0\Phi_n\Phi_p - b\Phi_p + (1 - R_0)\Phi_n}{b\Phi_p + (R_0 - 1)\Phi_n} \right). \tag{3.98}$$

To determine the stability for each of the three fixed points, I also need the Jacobian of system (3.42), which is

$$J(\bar{n}, \bar{p}) = \begin{bmatrix} \Phi_n(\bar{n}u_n + u) & \Phi_n \bar{n} u_p \\ \Phi_p \bar{p} v_n & \Phi_p(\bar{p}v_p + v) \end{bmatrix}, \tag{3.99}$$

where the subscripts on u and v denote partial derivatives. The partial derivatives of u and v are given in the first column of Table 3.1.

Table 3.1: Partial derivatives used to simplify Jacobian expressions for the exclusion equilibrium and the coexistence equilibrium.

Partial Derivatives	Partial Derivatives at the Coexistence Equilibrium
$u_n = \left(\frac{1-R_0}{R_0}\right) g(n)^2 h(p)$	$\Phi_n u_n = \left(\frac{1-R_0}{R_0}\right) g(\bar{n}^*)$
$u_p = -g(n)h(p)^2$	$\Phi_n u_p = -h(\bar{p}^*)$
$v_n = \frac{b}{R_0} h(p)g(n)^2$	$\Phi_p v_n = \frac{g(\bar{n}^*)}{R_0 \bar{n}^*}$
$v_p = -bng(n)h(p)^2$	$\Phi_p v_p = -h(\bar{p}^*)$

The equations in the second column are valid at the coexistence fixed point and will be used for stability analysis in Appendix 3.10.3. To get the equations in the second column, multiply the equations for the partial derivatives of u by Φ_n and the equations for the partial derivatives of v by Φ_p. Then, use the zero-growth nullcline equations from system (3.97) to simplify.

3.10.1 Stability of the extinction equilibrium

At the extinction equilbrium, the Jacobian is

$$J(0,0) = \begin{bmatrix} \Phi_n R_0 & 0 \\ 0 & 0 \end{bmatrix}. \tag{3.100}$$

The eigenvalues are $\lambda = \Phi_n R_0$ and $\lambda = 0$. Therefore, the extinction equilibrium is stable when $\Phi_n R_0 < 1$.

3.10.2 Stability of the exclusion equilibrium

The Jacobian of system (3.42) at the exclusion equilibrium, point (3.96), is

$$J(\bar{n}^*, 0) = \begin{bmatrix} \Phi_n(\bar{n}^* u_n + u) & \Phi_n \bar{n}^* u_p \\ 0 & \Phi_p v \end{bmatrix}. \tag{3.101}$$

Next, use the expressions for u and v from equations (3.10) and (3.11) and their partial derivatives from Table 3.1. Recall that g and h are given in equations (3.7) and (3.8) and $h(0) = 1$. The Jacobian simplifies to

$$J(\bar{n}^*, 0) = \begin{bmatrix} \Phi_n \left[\left(\dfrac{1 - R_0}{R_0} \right) \bar{n}^* g(\bar{n}^*)^2 + g(\bar{n}^*) \right] & -\Phi_n \bar{n}^* g(\bar{n}^*) \\ 0 & b\Phi_p \bar{n}^* g(\bar{n}^*) \end{bmatrix}. \tag{3.102}$$

At this equilibrium, it also holds that $\Phi_n g(\bar{n}^*) = 1$ from equation (3.95). Use this to simplify the Jacobian to

$$J(\bar{n}^*, 0) = \begin{bmatrix} \left(\frac{1-R_0}{R_0} \right) \bar{n}^* g(\bar{n}^*) + 1 & -\bar{n}^* \\ 0 & b\Phi_p \bar{n}^* g(\bar{n}^*) \end{bmatrix}. \tag{3.103}$$

Further simplify by evaluating $g(\bar{n}^*)$ at point (3.96) and simplify. Then

$$g(\bar{n}^*) = \frac{1}{\Phi_n}. \tag{3.104}$$

The Jacobian is thus

$$J(\bar{n}^*, 0) = \begin{bmatrix} \dfrac{1}{R_0\Phi_n} & -\bar{n}^* \\ 0 & \dfrac{b\Phi_p(\Phi_n R_0 - 1)}{\Phi_n(R_0 - 1)} \end{bmatrix}. \tag{3.105}$$

Because this matrix is upper-triangular, the eigenvalues are the elements on the diagonal, and the exclusion equilibrium will be stable when $|\lambda_1| < 1$ and $|\lambda_2| < 1$. For the first eigenvalue, this criteria is

$$|\lambda_1| = \left| \frac{1}{R_0\Phi_n} \right| < 1. \tag{3.106}$$

Since R_0 and Φ_n are positive, this criteria is most succinctly expressed as

$$R_0\Phi_n > 1. \tag{3.107}$$

For the second eigenvalue, the stability criteria is

$$|\lambda_2| = \left| \frac{b\Phi_p(\Phi_n R_0 - 1)}{\Phi_n(R_0 - 1)} \right| < 1. \tag{3.108}$$

When inequality (3.107) is satisfied, λ_2 is positive. Further, satisfaction of inequality (3.107) also implies that $R_0 > 1$ since $0 < \Phi_n < 1$. Thus, stability criterion (3.108) reduces to

$$b\Phi_p < \frac{\Phi_n(R_0 - 1)}{\Phi_n R_0 - 1}, \tag{3.109}$$

where parameters pertaining to the parasitoid species are on the left and parameters pertaining to the host species are on the right.

3.10.3 Stability of the coexistence equilibrium

Now consider the coexistence equilibrium, point (3.98). The Jacobian is

$$J(\bar{n}^*, \bar{p}^*) = \begin{bmatrix} \Phi_n\bar{n}^* u_n + 1 & \Phi_n\bar{n}^* u_p \\ \Phi_p\bar{p}^* v_n & \Phi_p\bar{p}^* v_p + 1 \end{bmatrix} \tag{3.110}$$

using the nullcline equations in system (3.97) to simplify. The trace and determinant of this system are

$$\tau = 2 + \Phi_n \bar{n}^* u_n + \Phi_p \bar{p}^* v_p \tag{3.111}$$

and

$$\Delta = 1 + \Phi_p \bar{p}^* v_p + \Phi_n \bar{n}^* u_n + \Phi_n \Phi_p \bar{n}^* \bar{p}^* (u_n v_p - u_p v_n). \tag{3.112}$$

The three Jury [40] conditions for this equilibrium are,

$$1 - \tau + \Delta = \Phi_n \Phi_p \bar{n}^* \bar{p}^* (u_n v_p - u_p v_n) > 0, \tag{3.113}$$

$$1 + \tau + \Delta = 4 + 2\Phi_n \bar{n}^* u_n + 2\Phi_p \bar{p}^* v_p + \Phi_n \Phi_p \bar{n}^* \bar{p}^* (u_n v_p - u_p v_n) > 0, \tag{3.114}$$

and

$$\Delta = 1 + \Phi_p \bar{p}^* v_p + \Phi_n \bar{n}^* u_n + \Phi_n \Phi_p \bar{n}^* \bar{p}^* (u_n v_p - u_p v_n) < 1. \tag{3.115}$$

Satisfaction of these Jury conditions guarantees asymptotic stability of the coexistence fixed point. A detailed discussion of the meaning of the Jury conditions for a similar host–parasitoid system can be found in [59].

Jury conditions for stability of the coexistence equilibrium

Using the expressions from Table 3.1, the first Jury condition, inequality (3.113) simplifies to

$$\bar{n}^* \bar{p}^* \left[\left(\frac{R_0 - 1}{R_0} \right) g(\bar{n}^*) h(\bar{p}^*) + h(\bar{p}^*) \frac{g(\bar{n}^*)}{R_0 \bar{n}^*} \right] > 0. \tag{3.116}$$

This is the same first Jury condition as Model 1 in my nonspatial work [59]. If $\bar{n}^* > 0$, $\bar{p}^* > 0$, this reduces to

$$\frac{h(\bar{p}^*)}{\bar{n}^*} > 0. \tag{3.117}$$

This condition is satisfied whenever the coexistence fixed point is in the interior of the first quadrant. In the next section, I determine the criteria for the coexistence point to be in the interior of the first quadrant.

Now look at the second Jury condition. Using a strategy from [59], consider the sign of τ,

$$\tau = 2 + \Phi_n \bar{n}^* u_n + \Phi_p \bar{p}^* v_p = 2 - \left[\left(\frac{R_0 - 1}{R_0} \right) \bar{n}^* g(\bar{n}^*) + \bar{p}^* h(\bar{p}^*) \right]. \tag{3.118}$$

If $\tau > 0$ and the first Jury condition is satisfied, then

$$1 + \tau + \Delta > 1 - \tau + \Delta > 0, \tag{3.119}$$

and the first Jury condition is a sufficient criterion for the second Jury condition.

The expression for τ in equation (3.118) is the same as τ for Model 1 in my previous work [59] and was shown to be positive for $n^* > 0$, $p^* > 0$, and $R_0 > 1$. Therefore, the second Jury condition is a sufficient condition for the first Jury condition for coexistence equilibrium (3.98) if $n^* > 0$, $p^* > 0$, and $R_0 > 1$.

Finally, consider the third Jury condition, inequality (3.115), which simplifies to

$$1 + \left(\frac{1 - R_0}{R_0} \right) n^* g(n^*) < 1. \tag{3.120}$$

This expression is the starting point for the third Jury condition in Appendix B of [59]. Accordingly, the third Jury condition simplifies to

$$1 + (R_0 - 1) n^* > 1, \tag{3.121}$$

which is true for $R_0 > 1$ for the equilibrium in the interior of the first quadrant.

When is the coexistence equilibrium in the interior of the first quadrant?

The $\bar{n}$-coordinate of the coexistence equilibrium, point (3.98), is

$$\bar{n}^* = \frac{\Phi_n}{\Phi_p} \frac{1}{b}. \tag{3.122}$$

Since all of the parameters here are positive by definition, the $\bar{n}$-coordinate is positive.

The coexistence equilibrium value of the parasitoid for the averaged system is

$$\bar{p}^* = \frac{bR_0\Phi_n\Phi_p - b\Phi_p + (1-R_0)\Phi_n}{b\Phi_p + (R_0-1)\Phi_n}. \tag{3.123}$$

As previously mentioned in Section 3.5.1, I assume $R_0 >$, so the denominator,

$$b\Phi_p + (R_0-1)\Phi_n, \tag{3.124}$$

is positive.

Since the denominator is positive, $\bar{p}^*$ will be positive if the numerator is positive too,

$$bR_0\Phi_n\Phi_p - [b\Phi_p + (R_0-1)\Phi_n] > 0. \tag{3.125}$$

Solving to put parameters related to the parasitoid on the left and parameters related to the host species on the right,

$$b\Phi_p > \frac{(R_0-1)\Phi_n}{\Phi_n R_0 - 1}, \tag{3.126}$$

assuming that $\Phi_n R_0 - 1 > 0$. Recall that when $\Phi_n G_0 - 1 < 0$, the extinction equilibrium is stable and the coexistence equilibrium is unstable.

If $\Phi_n R_0 - 1 < 0$, then the direction of the inequality in (3.126) would change, and the value on the right-hand side of the inequality would be negative. This would imply that $b\Phi_p < 0$, which leads to a contradiction since $b\Phi_p > 0$ by definition. So if $\Phi_n R_0 - 1 < 0$, then the numerator of (3.123) is negative and $\bar{p}^* < 0$.

To summarize, the coexistence equilibrium is in the interior of the first quadrant if $\Phi_n R_0 - 1 > 0$ and inequality (3.126) is satisfied.

3.11 *Appendix G: Fixed points and stability for Case 3 system of difference equations*

The equilibria of system (3.87) are found by setting $\bar{n}_{t+1} = \bar{n}_t = \bar{n}^*$ and $\bar{p}_{t+1} = \bar{p}_t = \bar{p}^*$. The exclusion equilibrium, $(0,0)$, is a fixed point of system (3.87). If $\bar{p} = 0$, the non-zero $\bar{n}$

coordinate of the equilibrium is the solution to

$$1 = \frac{1}{2}(1-w)G_{n_1}u\left(\bar{n},0\right) + wG_{n_2}u\left(\bar{n},0\right) + \frac{1}{2}(1-w)G_{n_3}u\left(\bar{n},0\right) = G_n g(\bar{n}), \tag{3.127}$$

where the second equality is true because

$$G_n = \frac{1}{2}(1-w)(G_{n_1} + G_{n_3}) + wG_{n_2} \tag{3.128}$$

and $u(\bar{n},0) = g(\bar{n})$. The exclusion equilibrium is therefore

$$(\bar{n}^*, \bar{p}^*) = \left(\frac{G_n R_0 - 1}{R_0 - 1}, 0\right). \tag{3.129}$$

The coexistence equilibrium for Case 3 is the solution $(\bar{n}^*, \bar{p}^*)$ to

$$1 = \frac{1}{2}(1-w)(G_{n_1} + G_{n_3})g(\bar{n}) + wG_{n_2}u(\bar{n},\bar{p}), \tag{3.130a}$$

$$1 = G_p v(\bar{n},\bar{p}). \tag{3.130b}$$

Equation (3.130a) is the host nullcline, and equation (3.130b) is the parasitoid nullcline.

To determine the stability of each of the three fixed points, I need the Jacobian of system (3.87), which is

$$J(\bar{n},\bar{p}) = \begin{bmatrix} \frac{1}{2}(1-w)\left(G_{n_1}+G_{n_3}\right)\left[g(\bar{n}) + \bar{n}g'(\bar{n})\right] & wG_{n_2}\bar{n}u_p(\bar{n},\bar{p}) \\ \quad + wG_{n_2}\left[u(\bar{n},\bar{p}) + \bar{n}u_n(\bar{n},\bar{p})\right] & \\ G_p p v_n(\bar{n},\bar{p}) & G_p[\bar{p}v_p(\bar{n},\bar{p}) + v(\bar{n},\bar{p})] \end{bmatrix}, \tag{3.131}$$

where subscripts on functions u and v denote partial derivatives, given in the first column of Table 3.1.

3.11.1 Stability of the extinction equilibrium

At the extinction equilibrium, the Jacobian is

$$J(0,0) = \begin{bmatrix} R_0\left[\frac{1}{2}(1-w)\left(G_{n_1}+G_{n_3}\right) + wG_{n_2}\right] & 0 \\ 0 & 0 \end{bmatrix} = \begin{bmatrix} G_n R_0 & 0 \\ 0 & 0 \end{bmatrix}, \tag{3.132}$$

where I use equation (3.128) to simplify. The eigenvalues are $\lambda_1 = G_n R_0$ and $\lambda_2 = 0$, so the extinction equilibrium is stable when $G_n R_0 < 1$.

3.11.2 Stability of the exclusion equilibrium

At the exclusion equilibrium, $\bar{p} = 0$, and the Jacobian simplifies to

$$J(\bar{n}, 0) = \begin{bmatrix} \frac{1}{2}(1-w)\left(G_{n_1} + G_{n_3}\right)\left[g(\bar{n}) + \bar{n}g'(\bar{n})\right] & wG_{n_2}\bar{n}u_p(\bar{n}, 0) \\ +wG_{n_2}\left[u(\bar{n}, 0) + nu_n(\bar{n}, 0)\right] & \\ 0 & G_p v(\bar{n}, 0) \end{bmatrix}. \tag{3.133}$$

Using the definition of u and partial derivatives u_n and u_p from Table 3.1, the Jacobian simplifies to

$$J(\bar{n}, 0) = \begin{bmatrix} \left[\frac{1}{2}(1-w)\left(G_{n_1} + G_{n_3}\right) + wG_{n_2}\right]\left[\bar{n}g'(\bar{n}) + g(\bar{n})\right] & -wG_{n_2}\bar{n}g(\bar{n}) \\ 0 & bG_p\bar{n}g(\bar{n}) \end{bmatrix}. \tag{3.134}$$

Using equation (3.128), the Jacobian is

$$J(\bar{n}, 0) = \begin{bmatrix} G_n[\bar{n}g'(\bar{n}) + g(\bar{n})] & -wG_{n_2}\bar{n}g(\bar{n}) \\ 0 & bG_p\bar{n}g(\bar{n}) \end{bmatrix}. \tag{3.135}$$

Since

$$g'(n) = \left(\frac{1 - R_0}{R_0}\right) g(n)^2, \tag{3.136}$$

then the diagonal entries of Jacobian (3.135) are the same as those of the Jacobian for the exclusion equilibrium in Case 2, equation (3.102). The expression for the coexistence equilibrium is the same for Cases 2 and 3, and the eigenvalues simplify in the same way. Therefore, the exclusion equilibrium for Case 3 will be stable when

$$R_0 G_n > 1 \tag{3.137}$$

and

$$bG_p < \frac{G_n(R_0 - 1)}{G_n R_0 - 1}, \tag{3.138}$$

where parameters pertaining to the parasitoid species are on the left and parameters pertaining to the host species are on the right.

3.11.3 Existence and uniqueness of the coexistence equilibrium

Instead of working with the algebraically messy expression for the coexistence equilibrium to determine conditions for its existence and uniqueness, I instead work with the nullclines, equations (3.130a) and (3.130b).

Begin with the host nullcline, equation (3.130a), and solve for $\bar{p}$,

$$\bar{p} = \frac{G_n R_0 - [1 + (R_0 - 1)\bar{n}]}{1 - \frac{1}{2}(1 - w)\left(G_{n_1} + G_{n_3}\right) R_0 + (R_0 - 1)\bar{n}}. \tag{3.139}$$

In the $\bar{n}$–$\bar{p}$ plane, the slope of the host nullcline is

$$\bar{p}' = \frac{R_0(R_0 - 1)\left[\frac{1}{2}(1 - w)\left(G_{n_1} + G_{n_3}\right) - G_n\right]}{[1 - \frac{1}{2}(1 - w)\left(G_{n_1} + G_{n_3}\right) R_0 + (R_0 - 1)\bar{n}]^2}. \tag{3.140}$$

Since the denominator of p' is positive, the slope of the host nullcline will be negative when

$$R_0(R_0 - 1)\left[\frac{1}{2}(1 - w)\left(G_{n_1} + G_{n_3}\right) - G_n\right] < 0. \tag{3.141}$$

This is true when $R_0 > 1$, since $G_n = \frac{1}{2}(1 - w)\left(G_{n_1} + G_{n_3}\right) + wG_{n_3}$ by definition.

Now consider the asymptotes of the host nullcline. There is a horizontal asymptote at $\bar{p} = -1$ as $\bar{n} \to \infty$ and $\bar{n} \to -\infty$. The vertical asymptote occurs when the denominator of equation (3.139) is zero, which occurs at

$$\bar{n} = \frac{\frac{1}{2}(1 - w)\left(G_{n_1} + G_{n_3}\right) R_0 - 1}{R_0 - 1}. \tag{3.142}$$

If $R_0 > 1$ and

$$\frac{R_0}{2}(1 - w)\left(G_{n_1} + G_{n_3}\right) > 1, \tag{3.143}$$

then the vertical asymptote will occur in the first quadrant. Whether or not this is true, the $\bar{n}$-intercept of the host nullcline is

$$n_{\text{int}} = \frac{G_n R_0 - 1}{R_0 - 1}, \tag{3.144}$$

which is positive if $G_n R_0 > 1$ and $R_0 > 1$. If $R_0 > 1$, the host nullcline will only pass through the first quadrant if $G_n R_0 > 1$.

Now consider the parasitoid nullcline, equation (3.130b), which can also be solved for $\bar{p}$,

$$\bar{p} = \frac{bG_p R_0 \bar{n} - [1 + (R_0 - 1)\bar{n}]}{1 + (R_0 - 1)\bar{n}}. \tag{3.145}$$

The slope of the parasitoid nullcline is

$$\bar{p}' = \frac{bG_p R_0}{[1 + (R_0 - 1)\bar{n}]^2}. \tag{3.146}$$

This quantity is positive.

Next consider the asymptotes of the parasitoid isocline. For $\bar{n} \to \infty$ and $\bar{n} \to -\infty$, there is a horizontal asymptote at

$$\bar{p} = \frac{R_0(bG_p - 1) + 1}{R_0 - 1}. \tag{3.147}$$

This asymptote is positive when $R_0 > 1$ and

$$bG_p > \frac{R_0 - 1}{R_0}. \tag{3.148}$$

The parasitoid vertical asymptote occurs at

$$\bar{n} = \frac{-1}{R_0 - 1}. \tag{3.149}$$

This is negative for $R_0 > 1$.

Since the parasitoid nullcline is monotone increasing except at the vertical asymptote for which $\bar{n} < 0$, I conclude that if the nullcline exists in the first quadrant, it is monotonically

increasing. Additionally, since the parasitoid vertical asymptote is negative and the nullcline is monotonically increasing except at the asymptote, the parasitoid nullcline is in the first quadrant if and only if the horizontal asymptote is positive, which requires $R_0 > 1$ and

$$bG_p > \frac{R_0 - 1}{R_0}. \tag{3.150}$$

If the host nullcline is in the first quadrant, it is monotonically decreasing. If the parasitoid nullcline is in the first quadrant, it is monotonically increasing. Therefore, if there is a coexistence equilibrium in the first quadrant, it is unique.

The parasitoid isocline has $\bar{n}$-intercept at

$$\bar{n}_{\text{int}} = \frac{1}{bG_pR_0 - (R_0 - 1)}. \tag{3.151}$$

The host and parasitoid nullclines will intersect in the first quadrant if both nullclines are in the first quadrant and the parasitoid $\bar{n}$-intercept is smaller than the host $\bar{n}$-intercept. Therefore, for $R_0 > 1$, existence of the coexistence equilibrium in the first quadrant requires $G_nR_0 > 1$ to ensure that the host nullcline is in the first quadrant,

$$bG_p > \frac{R_0 - 1}{R_0} \tag{3.152}$$

to ensure that the parasitoid nullcline is in the first quadrant, and

$$\frac{1}{bG_pR_0 - (R_0 - 1)} < \frac{G_nR_0 - 1}{R_0 - 1}. \tag{3.153}$$

to guarantee that the nullclines intersect in the first quadrant. A quick proof by contradiction shows that if $G_nR_0 > 1$ and

$$\frac{1}{bG_pR_0 - (R_0 - 1)} < \frac{G_nR_0 - 1}{R_0 - 1}, \tag{3.154}$$

then

$$bG_p > \frac{R_0 - 1}{R_0}. \tag{3.155}$$

So the condition for the coexistence equilibrium to be in the first quadrant simplifies to $G_n R_0 > 1$ and

$$\frac{1}{bG_pR_0 - (R_0 - 1)} < \frac{G_nR_0 - 1}{R_0 - 1}. \tag{3.156}$$

3.11.4 Stability of the coexistence equilibrium

At the coexistence equilibrium, $(\bar{n}^*, \bar{p}^*)$, the Jacobian from equation (3.131) simplifies to

$$J(\bar{n}^*, \bar{p}^*) = \begin{bmatrix} 1 + \frac{1}{2}(1-w)\left(G_{n_1} + G_{n_3}\right) ng'(\bar{n}^*) + wG_{n_2}\bar{n}^* u_n(\bar{n}^*, \bar{p}^*) & wG_{n_2}\bar{n}^* u_p(\bar{n}^*, \bar{p}^*) \\ G_p\bar{p}^* v_n(\bar{n}^*, \bar{p}^*) & G_p p v_p(\bar{n}^*, \bar{p}^*) + 1 \end{bmatrix}, \tag{3.157}$$

where I use the nullclines, equations (3.130) to simplify. The trace and determinant of this system are

$$\tau = 2 + \frac{1}{2}(1-w)(G_{n_1} + G_{n_3})\bar{n}^* g'(\bar{n}^*) + wG_{n_2}\bar{n}^* u_n + G_p\bar{p}^* v_p \tag{3.158}$$

and

$$\Delta = \begin{cases} 1 + G_p\bar{p}^* v_p + \frac{1}{2}(1-w)(G_{n_1} + G_{n_3})\bar{n}^* g'(\bar{n}^*) + wG_{n_2}\bar{n}^* u_n \\ \quad + G_p\bar{n}^*\bar{p}^* \left[\frac{1}{2}(1-w)(G_{n_1} + G_{n_3})g'(\bar{n}^*)v_p + wG_{n_2}u_n v_p - wG_{n_2}u_p v_n\right]. \end{cases} \tag{3.159}$$

Using expressions for g' and the partial derivatives of u and v from the first column of Table 3.1, the trace is

$$\tau = \begin{cases} 2 + \bar{n}^* \left(\frac{1 - R_0}{R_0}\right) g(\bar{n}^*) \left[\frac{1}{2}(1-w)(G_{n_1} + G_{n_3})g(\bar{n}^*) + wG_{n_2}g(\bar{n}^*)h(\bar{p}^*)\right] \\ \quad -\bar{p}^* h(\bar{p}^*)[bG_p\bar{n}^* g(\bar{n}^*)h(\bar{p}^*)]. \end{cases} \tag{3.160}$$

Using the host and parasitoid nullclines, equations (3.130), this reduces to

$$\tau = 2 + \left(\frac{1-R_0}{R_0}\right)\bar{n}^* g(\bar{n}^*) - \bar{p}^* h(\bar{p}^*). \tag{3.161}$$

Similarly, use expressions for g' and the partial derivatives of u and v from the first column of Table 3.1 and then use the host and parasitoid nullclines, equations (3.130), to simplify the determinant. The result is

$$\Delta = 1 - \bar{p}^* h(\bar{p}^*) + \left(\frac{1-R_0}{R_0}\right)\bar{n}^* g(\bar{n}^*) + \bar{n}^*\bar{p}^*\left[\left(\frac{1-R_0}{R_0}\right) g(\bar{n}^*) v_p G_p - w G_{n_2} G_p u_p v_n\right]. \tag{3.162}$$

I now use the three Jury [40] conditions,

$$1 - \tau + \Delta > 0, \tag{3.163}$$

$$1 + \tau + \Delta > 0, \tag{3.164}$$

and

$$\Delta < 1, \tag{3.165}$$

to determine the stability of the coexistence equilibrium.

First Jury condition for stability of the coexistence equilibrium

The first Jury condition simplifies to

$$0 < \bar{n}^*\bar{p}^*\left[\left(\frac{1-R_0}{R_0}\right) g(\bar{n}^*) v_p G_p - w G_{n_2} G_p u_p v_n\right]. \tag{3.166}$$

Using the expressions for the partial derivatives from Table 3.1 and simplifying, the Jury condition can be written

$$0 < \bar{n}^*\bar{p}^*\left[\frac{R_0 - 1}{R_0} g(\bar{n}^*) h(\bar{p}^*)\right][b G_p \bar{n}^* g(\bar{n}^*) h(\bar{p}^*)] + p\frac{w G_{n_2}}{R_0} g(\bar{n}^*)^2 h(\bar{p}^*)^2 [b G_p \bar{n}^* g(\bar{n}^*) h(\bar{p}^*)]. \tag{3.167}$$

Using the parasitoid isocline equation to simplify, this is

$$0 < \bar{n}^*\bar{p}^* \left(\frac{R_0 - 1}{R_0}\right) g(\bar{n}^*)h(\bar{p}^*) + \frac{\bar{p}^* w G_{n_2}}{R_0} g(\bar{n}^*)^2 h(\bar{p}^*)^2. \tag{3.168}$$

Multiplying by R_0 and dividing by $g(\bar{n}^*)$ and $\bar{p}^*h(\bar{p}^*)$, which are all positive, gives

$$0 < \bar{n}^*(R_0 - 1) + wG_{n_2} g(\bar{n}^*)h(\bar{p}^*). \tag{3.169}$$

For $R_0 > 1$ and a coexistence equilibrium in the interior of the first quadrant, this expression is positive, so the first Jury condition is satisfied.

Second Jury condition for stability of the coexistence equilibrium

For the second Jury condition, I use the method as in Section 3.10.3. If $\tau > 0$ and $1-\tau+\Delta > 0$, then $1 + \tau + \Delta > 1 - \tau + \Delta > 0$. That is to say, a positive trace and the satisfaction of the first Jury condition are sufficient criteria for the second Jury condition

Plug in $g(\bar{n}^*)$ and $h(\bar{p}^*)$ into equation (3.161) and simplify,

$$\tau = 2 - \frac{(R_0 - 1)\bar{n}^*}{1 + (R_0 - 1)\bar{n}^*} - \frac{\bar{p}^*}{1 + \bar{p}^*}. \tag{3.170}$$

Since $R_0 > 1$, both the middle and last terms are of the form $z(1 + z)^{-1}$ where z is positive, where I assume $\bar{n}^* > 0$, $\bar{p}^* > 0$, since I'm analyzing the stability of the coexistence equilibrium in the interior of the first quadrant. The middle and last terms are each less than one individually because $z < 1 + z$ and $z(1 + z)^{-1} < 1$ for positive z. I therefore conclude that $\tau > 0$, and thus the first Jury condition is a sufficient criterion for the second Jury condition.

Third Jury condition for stability of the coexistence equilibrium

Begin by using the parasitoid nullcline, equation (3.130b) to further simplify the determinant to

$$\Delta = 1 - \bar{p}^*h(\bar{p}^*) + \left(\frac{1 - R_0}{R_0}\right)\bar{n}^*g(\bar{n}^*) + \bar{n}^*\bar{p}^*\left[\frac{R_0 - 1}{R_0} g(\bar{n}^*)h(\bar{p}^*) + \frac{w}{R_0\bar{n}^*} G_{n_2} g(\bar{n}^*)^2 h(\bar{p}^*)^2\right]. \tag{3.171}$$

After quite a bit of algebra, the third Jury condition, $\Delta < 1$, can be written

$$0 > \frac{\bar{p}^* h(\bar{p}^*)\{-[1+(R_0-1)\bar{n}^*] + wG_{n_2} h(\bar{p}^*)R_0\} + (1-R_0)\bar{n}^*[1+(R_0-1)\bar{n}^*]}{[1+(R_0-1)\bar{n}^*]^2}. \quad (3.172)$$

Multiply both sides by $[1+(R_0-1)\bar{n}^*]^2$ so that

$$0 > -\bar{p}^* h(\bar{p}^*)[1+(R_0-1)\bar{n}^*] + \bar{p}^* h(\bar{p}^*)^2 wG_{n_2}R_0 - [(R_0-1)\bar{n}^* + (R_0-1)^2(\bar{n}^*)^2]. \quad (3.173)$$

Next, use the host nullcline, equation (3.130a) to solve for $h(\bar{p}^*)$,

$$h(\bar{p}^*) = \frac{1}{1+\bar{p}^*} = \frac{1+(wG_{n_2}-G_n)g(\bar{n}^*)}{wG_{n_2}g(\bar{n}^*)}. \quad (3.174)$$

Then solve for $\bar{p}^*$ and simplify,

$$\bar{p}^* = \frac{-1+g(\bar{n}^*)G_n}{1+g(\bar{n}^*)(wG_{n_2}-G_n)}. \quad (3.175)$$

Then simplify the expression for $\bar{p}^* h(\bar{p}^*)$,

$$\bar{p}^* h(\bar{p}^*) = \frac{g(\bar{n}^*)G_n - 1}{wG_{n_2}g(\bar{n}^*)}. \quad (3.176)$$

Return to the third Jury condition as written in inequality (3.173) and now substitute in expressions (3.175) and (3.176) for $\bar{p}^*$ and $\bar{p}^* h(\bar{p}^*)$. Also, use the definition of $g(n)$ from equation (3.7) and simplify. The third Jury condition is now

$$0 > \frac{(G_n - wG_{n_2})[1+(R_0-1)\bar{n}^*] + R_0G_n(wG_{n_2}-G_n)}{wG_{n_2}} - (R_0-1)\bar{n}^*[1+(R_0-1)\bar{n}^*]. \quad (3.177)$$

where $\bar{p}^*$ is no longer in the expression.

Multiply both sides of the inequality by wG_{n_2}, which is positive, and rearrange terms until the expression is

$$0 > G_n + G_n(R_0-1)\bar{n}^* - G_n^2R_0 - wG_{n_2}[1+(R_0-1)\bar{n}^*]^2 + wG_{n_2}G_nR_0. \quad (3.178)$$

I was not able to analytically show that this is true for the coexistence equilibrium in the first quadrant. To test my hypothesis that it is true, I wrote a code in `MATLAB` to sweep through combinations of parameter values, check for conditions to see if those parameters align with a coexistence equilibrium in the first quadrant, and to check inequality (3.178).

To do this, I also needed an expression for $\bar{n}^*$, the host coordinate of the coexistence equilibrium. I solved equation (3.90) and used the positive value of n^*,

$$n^* = \begin{cases} \dfrac{-1}{2bG_p(R_0-1)}\left[bG_p(1-G_nR_0)+wG_{n_2}(1-R_0)+bG_pwG_{n_2}R_0\right] \\ \quad +\dfrac{-1}{2bG_p(R_0-1)}\sqrt{\dfrac{4wG_{n_2}}{bG_p}(R_0-1)+\left[1+R_0(wG_{n_2}-G_n)+\dfrac{wG_{n_2}}{bG_p}(1-R_0)\right]^2}. \end{cases} \tag{3.179}$$

The conditions on the parameters that I tested were:

$$R_0 > 1, \tag{3.180}$$

$$b > 1, \tag{3.181}$$

$$0 < G_p < 1, \tag{3.182}$$

$$0 < G_n < 1, \tag{3.183}$$

$$0 < w < 1, \tag{3.184}$$

$$0 < G_{n_2} < 1, \tag{3.185}$$

$$G_n > wG_{n_2}, \tag{3.186}$$

$$G_nR_0 > 1, \tag{3.187}$$

$$bG_p > \frac{G_n(R_0-1)}{G_nR_0-1}. \tag{3.188}$$

I was able to numerically conclude that the third Jury condition is satisfied when the coexistence equilibrium is in the interior of the first quadrant.

3.11.5 Critical speed for host and parasitoid survival, Case 3

To find critical speeds for parasitoid survival for Case 3, one can compute the critical speed c^* by using a root-finder to solve

$$bG_p = \frac{G_n(R_0 - 1)}{G_n R_0 - 1}, \tag{3.189}$$

which is the same expression as in Case 2.

Chapter 4

DISCUSSION

Mechanistic models of biological phenomena require careful investigation of the components that contribute to the whole. In the near century of development of host–parasitoid models, much of the work has proceeded in a stepwise manner to develop "a detailed understanding of how the important processes operating in the host and parasitoid life cycles affect the dynamics of the populations" [33]. My work in this dissertation has followed in that tradition, seeking to develop understanding of simple host–parasitoid models that had been historically overlooked in Chapter 2 and working to introduce the impacts of climate-driven range shifts into host–parasitoid modeling in Chapter 3.

As discussed in Chapter 2, it is not uncommon for researchers to present and analyze a mathematical model of a host–parasitoid system, or other population system, with little to no indication of the assumptions that are inherent in the structure of the model. A mathematical audience is likely to appreciate rigorous analysis and proofs regarding the dynamics of a particular model, regardless of lack of explanation of the biological underpinnings of the model. However, I question whether such an omission contributes to collaborations between theorists and experimentalists, mathematicians and ecologists.

I have briefly mentioned a large range of current ecological problems and crises: species extinction, loss of biodiversity, invasion of nonnative species, destructive agricultural pests, and climate change. It is widely acknowledged that ecological theory is strengthened by quantitative models, and mechanistic models are an important tool in the development of ecological theory. In light of the magnitude of global ecological challenges, it is imperative that the development of mathematical models of population dynamics includes clear commu-

nication of underlying biological assumptions. As stated by Murdoch, Briggs, and Nisbett, "the gap between theorists and field ecologists is a serious impediment to progress in ecology" [64]. The dire nature of current ecological problems requires removing any impediments, including lack of communication, from the path towards solutions. To this end, I have sought to provide clear and sufficient explanation of the assumptions in the difference-equation models in Chapter 2 and the IDE models in Chapter 3.

4.1 Impacts of density-dependence and parasitism on dynamics

The building blocks that I analyzed in Chapter 2 were density dependence in the host species and interspecific parasitism, specifically for systems where density dependence precedes parasitism in the life cycle of the host. I compared two functions for intraspecific density-dependent survivorship: one function with a fractional form and the other with an exponential form. Similarly, one of the functions that I considered for fraction of hosts escaping parasitism has a fractional form and the other has an exponential form. Each function has a biological interpretation. The density-dependence functions describe the type of intraspecific competition for the host species, and the parasitism functions describe the degree of parasitoid aggregation in searching for hosts.

Livadiotis et al. [55] demonstrated that κ-parameterized functions with the same form can be written to describe both density-dependence and parasitism. The fractional forms of both density dependence and parasitism that I consider arise from the same κ value of Livadiotis et al.'s [55] κ-parameterized functions. The exponential forms of density dependence and parasitism arise from the $\kappa \to \infty$ case of Livadiotis et al.'s [55] functions. Despite the similarities in derivation, the impact of using a fractional vs. exponential form for density dependence differs from the results of using fractional vs. exponential parasitism.

The base host–parasitoid model that I considered includes both fractional density–dependence from the Beverton–Holt model and fractional parasitism. In this simple host–

parasitoid model, the system asymptotically approaches one of three equilibria: the extinction equilibrium, the exclusion equilibrium where the host is at carrying capacity with no parasitoid presence, or the coexistence equilibrium. If either of the fractional functions in the model are replaced with the alternative exponential one, population cycles can result. However, the type of cycle differs, depending on whether exponential density-dependence or exponential parasitism is substituted into the basic model. The exponential form of density dependence, corresponding to stronger nonlinearity in the density-dependence term, produces period-doubling bifurcations and the potential for bistability. Population dynamics after the period-doubling bifurcation can include large oscillations in host population size, including values both below and above carrying capacity. Alternately, the exponential form of parasitism, which corresponds to higher parasitism, produces Neimark–Sacker bifurcations and invariant circles for certain parameter ranges. The population dynamics in these situations involve smaller oscillations in host and parasitoid population size, with host values remaining below carrying capacity. The fourth model that I analyzed includes both exponential density-dependence and exponential parasitism. Population cycles in the fourth model take the form of invariant circles, and the period-doubling bifurcation is subcritical, such that the two-cycle is not stable.

Despite several decades of study, there continues to be much interest in better understanding the causes of cyclical outbreaks of insect herbivores [1, 19, 35, 64, 91, 92]. My work with the difference-equation models for host–parasitoid systems in Chapter 2 primarily focused on analysis around equilibria states, and I did not explicitly consider cycle length or amplitude for parameter ranges that result in invariant circles or n-cycles. To extend the applicability of my work, I would like to further analyze the impacts of density dependence and parasitism on population cycles. At present, the results of my analysis suggest that overcompensatory density-dependence can yield shorter-period, higher-amplitude oscillations and that stronger parasitism can cause multi-generation cycles with smaller amplitude. Ultimately, compari-

son with experimental data and collaboration with experimentalists is necessary to test the hypotheses suggested by my work.

4.2 Impacts of biotic interactions and space in the context of climate change

To the best of my knowledge, Allen et al. [3] analyzed the first IDE model for a host–parasitoid system. Their investigation used numerical simulations and was based on a "discrete spatial convolution model" [3], derived by discretizing the IDE system. A couple years later, Cobbold et al. [18] explored the effects of patch size on population persistence in a host–parasitoid IDE model. The IDE context added continuous space to the host–parasitoid difference-equation model they had previously studied [19]. My work in Chapter 3 builds on Cobbold et al.'s results by introducing climate change into a host–parasitoid IDE model, following the approach developed by Zhou and Kot [105, 106]. Note that unlike the system studied by Cobbold et al., the host–parasitoid system that I analyzed assumes that density dependence precedes parasitism.

One question addressed in my work in Chapter 3 is whether critical speed for parasitoid persistence on a moving habitat can be adequately approximated by a model that leaves out the full biotic interactions between the host and parasitoid. Case 1 considers the critical habitat speed for parasitoid persistence without modeling the simultaneous host dynamics, instead assuming the host is at carrying capacity on an infinite patch. Critical speeds for parasitoid survival in this case can be found using techniques developed for single-species moving-habitat IDE models. Because I assumed large host growth rate and an infinite host habitat patch, the results of Case 1 can provide an upper bound on the parasitoid's critical speed.

If the host and parasitoid share the same habitat patch, as is assumed in Case 2, the Case 1 critical speed is only a decent upper bound if the average parasitoid dispersal-distance is sufficiently small. The Case 1 estimate of critical speed improves with larger host net

reproductive rate, R_0, which makes sense since Case 1 assumes large R_0. Nevertheless, in most circumstances, the Case 1 system poorly predicts parasitoid survival criteria, because it does not account for less than ideal, and therefore more realistic, circumstances for the host population. In this scenario, the building block of modeling both host and parasitoid densities is necessary to capture the ability of the parasitoid to persist in the moving habitat.

On the other hand, if the host has a larger habitat than the parasitoid, as assumed in Case 3, the Case 1 critical speed is an excellent approximation for circumstances with large R_0 or large host patch-length. Again, this result makes sense since Case 1 assumes large host net reproductive rate and large host patch-size. The Case 3 model assumes that the parasitoid habitat patch is centered within the host patch, so it is possible that the Case 1 approximation would be a poor estimate for the parasitoid critical speed if the parasitoid patch was at either end of the host patch. Under certain spatial and biological assumptions, it appears that modeling the full biotic interactions between the host and parasitoid is not necessary to estimate parasitoid persistence criteria.

The other building block that I considered in Chapter 3 was explicit representation of space. To analyze parasitoid persistence on a finite, stationary habitat patch, Cobbold et al. [18] considered two approaches, both of which eventually required implicitly representing space with Van Kirk and Lewis's [95] average dispersal success. Through the work of Kot and Phillips [48] and Rinnan [79], the average dispersal success approximation has been shown to perform poorly for the asymmetrical kernels involved in analysis of single-species moving-habitat IDE models. In my analysis in Chapter 3, I compared a number of approximations for the proportion of individuals that remain in the patch after dispersal. Ultimately, geometric symmetrization and iterated geometric symmetrization are the best methods for representing the impacts of population loss due to dispersal with an asymmetric kernel. With the right approximation, implicit representation of space has minimal impact in addressing the question of criteria for coexistence of the host and parasitoid populations on a moving

habitat.

4.3 Closing thoughts

Any mathematical model of a biological phenomenon is limited in its explanation of the truth, but "the key question is not whether a model is true, but whether it is useful" [64]. The usefulness of a mathematical model will depend, at least in part, on the clarity of the assumptions inherent in the model. It is the responsibility of the theorist to describe the factors that are included in the model and to be honest about what is omitted. By necessity, simple mechanistic models of population dynamics will leave out ecological features that have some impact on the system. In doing so, something is lost, but the simplicity that is gained allows for clear description of the mechanisms that are present.

The models that I have studied in this dissertation undoubtedly fall into the category of simple models. The degree to which these models may predict specific population sizes or the exact limits of persistence for a parasitoid population is minimal at best. Yet these models elucidate some general principles and predictions about the general consequences of particular aspects of host–parasitoid population dynamics.

As a mathematician, I have a deep appreciation for conclusive truths that can be irrefutably established through logical proof. As an applied mathematician in the field of mathematical ecology, I understand the practicality and necessity of assessing models and theories by a metric of usefulness, rather than one of perfection. Indeed, "our simple theories can never capture all the complexity and detail of nature" [91]. As a life-long lover of wilderness and nature, I revel in the beauty of developing deeper understanding of the world around us. Paradoxically, while I intend to seek increased comprehension of the myriad of ecological processes at work in the world, I also find peace in acknowledging the limits of human comprehension and soaking in the wonder of the natural world, however imperiled it may be.

BIBLIOGRAPHY

[1] K. C. Abbott and G. Dwyer. Food limitation and insect outbreaks: Complex dynamics in plant-herbivore models. *J. Anim. Ecol.*, 76:1004–1014, 2007.

[2] D. Aikman and G. Hewitt. An experimental investigation of the rate and form of dispersal in grasshoppers. *J. Appl. Ecol.*, 9:807–817, 1972.

[3] J. C. Allen, C. C. Brewster, and D. H. Slone. Spatially explicit ecological models: a spatial convolution approach. *Chaos Solitons Fractals*, 12:333–347, 2001.

[4] L. J. S. Allen. *An Introduction to Mathematical Biology.* Pearson Education, Upper Saddle River, NJ, 2007.

[5] J. H Argyris, G. Faust, M. Haase, and R. Friedrich. *An Exploration of Dynamical Systems and Chaos: Completely Revised and Enlarged Second Edition.* Springer, Berlin, 2015.

[6] D. G. Aronson, M. A. Chory, G. R. Hall, and R. P. McGehee. Bifurcations from an invariant circle for two-parameter families of maps of the plane: A computer-assisted study. *Commun. Math. Phys.*, 83:303–354, 1982.

[7] R. Asheghi. Bifurcations and dynamics of a discrete predator–prey system. *J. Biol. Dyn.*, 8:161–186, 2014.

[8] N. D. Barlow. Models in biological control: a field guide. In B. A. Hawkins and H. V. Cornell, editors, *Theoretical Approaches to Biological Control*, pages 43–68. Cambridge University Press, Cambridge, 1999.

[9] J. R. Beddington, C. A. Free, and J. H. Lawton. Dynamic complexity in predator-prey models framed in difference equations. *Nature*, 255:58–60, 1975.

[10] E. Bešo, S. Kalabušić, N. Mujić, and E. Pilav. Stability of a certain class of a host–parasitoid models with a spatial refuge effect. *J. Biol. Dyn.*, 14:1–31, 2020.

[11] H. Berestycki, O. Diekmann, C. J. Nagelkerke, and P. A. Zegeling. Can a species keep pace with a shifting climate? *Bull. Math. Biol.*, 71:399, 2008.

[12] R. J. H. Beverton and Holt S. J. *On the Dynamics of Exploited Fish Populations*. Her Majesty's Stationery Office, London, 1957.

[13] F. J. J. A. Bianchi, N. A. Schellhorn, and W. van der Werf. Predicting the time to colonization of the parasitoid *Diadegma semiclausum*: The importance of the shape of spatial dispersal kernels for biological control. *Biol. Control*, 50:267–274, 2009.

[14] E. S. Brondizio, J. Settele, S. Diaz, and H. T. Ngo, editors. *Global Assessment Report on Biodiversity and Ecosystem Services*, Bonn, Germany, 2019. Intergovernmental Science-Policy Platform on Biodiversity and Ecosystem Services, IPBES secretariat.

[15] L. R. Carrasco, T. D. Harwood, S. Toepfer, A. MacLeod, N. Levay, J. Kiss, R. H. A. Baker, J. D. Mumford, and J. D. Knight. Dispersal kernels of the invasive alien western corn rootworm and the effectiveness of buffer zones in eradication programmes in Europe. *Ann. Appl. Biol.*, 156:63–77, 2010.

[16] D. S. Chapman, C. Dytham, and G. S. Oxford. Modelling population redistribution in a leaf beetle: an evaluation of alternative dispersal functions. *J. Anim. Ecol.*, 76:36–44, 2007.

[17] I-C. Chen, J. K. Hill, R. Ohlemüller, D. B. Roy, and C. D. Thomas. Rapid range shifts of species associated with high levels of climate warming. *Science*, 333:1024–1026, 2011.

[18] C. A. Cobbold, M. A. Lewis, F. Lutscher, and J. Roland. How parasitism affects critical patch-size in a host–parasitoid model: application to the forest tent caterpillar. *Theor. Popul. Biol.*, 67:109–125, 2005.

[19] C. A. Cobbold, J. Roland, and M. A. Lewis. The impact of parasitoid emergence time on host–parasitoid population dynamics. *Theor. Popul. Biol.*, 75:201–215, 2009.

[20] G. De Vries, T. Hillen, M. Lewis, J. Müller, and B. Schönfisch. *A Course in Mathematical Biology: Quantitative Modeling with Mathematical and Computational Methods*. Society for Industrial and Applied Mathematics, Philadelphia, PA, 2006.

[21] L. M. Delves and J. Walsh. *Numerical Solution of Integral Equations*. Clarendon Press, London, 1974.

[22] Q. Din. Global stability and Neimark–Sacker bifurcation of a host–parasitoid model. *Internat. J. Systems Sci.*, 48:1194–1202, 2017.

[23] Q. Din, M. A. Khan, and U. Saeed. Qualitative behaviour of generalised Beddington model. *Z. Naturforsch. A*, 71:145–155, 2016.

[24] T. Dobzhansky and S. Wright. Genetics of natural populations. X. Dispersion rates in *Drosophila pseudoobscura*. *Genetics*, 28:304–340, 1943.

[25] L. Edelstein-Keshet. *Mathematical Models in Biology*. SIAM, 2005.

[26] W. F. Fagan and F. Lutscher. Average dispersal success: Linking home range, dispersal, and metapopulation dynamics to reserve design. *Ecol. Appl.*, 16:820–828, 2006.

[27] Z. Fric and M. Konvicka. Dispersal kernels of butterflies: Power-law functions are invariant to marking frequency. *Basic Appl. Ecol.*, 8:377–386, 2007.

[28] G. Frobenius. Über matrizen aus nicht negativen elementen. *Sitz. Königlich Preuss. Akad. Wissensch.*, 1912:456–477, 1912.

[29] H. C. J. Godfray. *Parasitoids*. Princeton University Press, Princeton, NJ, 1994.

[30] M. A. Harsch, A. Phillips, Y. Zhou, M.-R. Leung, D. S. Rinnan, and M. Kot. Moving forward: insights and applications of moving-habitat models for climate change ecology. *J. Ecol.*, 105:1169–1181, 2017.

[31] M. A. Harsch, Y. Zhou, J. HilleRisLambers, and M. Kot. Keeping pace with climate change: Stage-structured moving-habitat models. *Am. Nat.*, 184:25–37, 2014.

[32] M. P. Hassell. *The Dynamics of Arthropod Predator–Prey Systems*. Princeton University Press, Princeton, NJ, 1978.

[33] M. P. Hassell. *The Spatial and Temporal Dynamics of Host–Parasitoid Interactions*. Oxford University Press, Oxford, 2000.

[34] T. Hovestadt, B. Binzenhöfer, P. Nowicki, and J. Settele. Do all inter-patch movements represent dispersal? A mixed kernel study of butterfly mobility in fragmented landscapes. *J. Anim. Ecol.*, 80:1070–1077, 2011.

[35] J. S. Hughes, C. A. Cobbold, K. Haynes, and G. Dwyer. Effects of forest spatial structure on insect outbreaks: Insights from a host-parasitoid model. *Am. Nat.*, 185:E130–E152, 2015.

[36] S. R.-J. Jang and D. M. Johnson. Dynamics of discrete-time larch budmoth population models. *J. Biol. Dyn.*, 3:209–223, 2009.

[37] S. R.-J. Jang and J.-L. Yu. Discrete-time host–parasitoid models with pest control. *J. Biol. Dyn.*, 6:718–739, 2012.

[38] M. H. Jensen and S. Krishna. Inducing phase-locking and chaos in cellular oscillators by modulating the driving stimuli. *FEBS Letters*, 586:1664–1668, 2012.

[39] Robert Jentzsch. Über integralgleichungen mit positivem kern. *J. Reine Angew. Math.*, 1912:235–244, 1912.

[40] E. I. Jury. *Theory and Application of the z-Transform Method*. Wiley, New York, 1964.

[41] Y. Kang, D. Armbruster, and Y. Kuang. Dynamics of a plant–herbivore model. *J. Biol. Dyn.*, 2:89–101, 2008.

[42] S. Kapçak, S. Elaydi, and Ü. Ufuktepe. Stability of a predator–prey model with refuge effect. *J. Difference Equ. Appl.*, 22:989–1004, 2016.

[43] S. Kapçak, Ü. Ufuktepe, and S. Elaydi. Stability and invariant manifolds of a generalized Beddington host–parasitoid model. *J. Biol. Dyn.*, 7:233–253, 2013.

[44] L. Yu. Kolotilina. Lower bounds for the Perron root of a nonnegative matrix. *Linear Algebra Appl.*, 180:133–151, 1993.

[45] R. Kon. Multiple attractors in host-–parasitoid interactions: Coexistence and extinction. *Math. Biosci.*, 201:172–183, 2006.

[46] M. Kot. *Elements of Mathematical Ecology*. Cambridge University Press, Cambridge, 2001.

[47] M. Kot, M. A. Lewis, and P. van den Driessche. Dispersal data and the spread of invading organisms. *Ecology*, 77:2027–2042, 1996.

[48] M. Kot and A. Phillips. Bounds for the critical speed of climate-driven moving-habitat models. *Math. Biosci.*, 262:65–72, 2015.

[49] M. Kot and W. M. Schaffer. Discrete-time growth-dispersal models. *Math. Biosci.*, 80:109–136, 1986.

[50] Y. A. Kuznetsov. *Elements of Applied Bifurcation Theory.* Springer, New York, 2004.

[51] H. A. Lauwerier. Two-dimensional iterative maps. In A. V. Holden, editor, *Chaos*, pages 58–95. Manchester University Press, Manchester, 1986.

[52] S. J. Leroux, M. Larrivée, V. Boucher-Lalonde, A. Hurford, J. Zuloaga, J. T. Kerr, and F. Lutscher. Mechanistic models for the spatial spread of species under climate change. *Ecol. Appl.*, 23:815–828, 2013.

[53] B. R. Liu and M. Kot. Accelerating invasions and the asymptotics of fat-tailed dispersal. *J. Theor. Biol.*, 471:22–41, 2019.

[54] G. Livadiotis, L. Assas, B. Dennis, S. Elaydi, and E. Kwessi. A discrete-time host–parasitoid model with an Allee effect. *J. Biol. Dyn.*, 9:34–51, 2015.

[55] G. Livadiotis, L. Assas, B. Dennis, S. Elaydi, and E. Kwessi. Kappa function as a unifying framework for discrete population modeling. *Nat. Resour. Model.*, 29:130–144, 2016.

[56] D. R. Lockwood, A. Hastings, and L. W. Botsford. The effects of dispersal patterns on marine reserves: Does the tail wag the dog? *Theor. Popul. Biol.*, 61(3):297–309, 2002.

[57] F. Lutscher. *Integrodifference Equations in Spatial Ecology.* Springer, Cham, Switzerland, 2019.

[58] F. Lutscher and M. A. Lewis. Spatially-explicit matrix models. *J. Math. Biol.*, 48:293–324, 2004.

[59] K. Marcinko and M. Kot. A comparative analysis of host–parasitoid models with density dependence preceding parasitism. *J. of Biol. Dyn.*, 14:479–514, 2020.

[60] R. M. May. Host–parasitoid systems in patchy environments: A phenomenological model. *J. Animal Ecol.*, 47:833–844, 1978.

[61] R. M. May, M. P. Hassell, R. M. Anderson, and D. W. Tonkyn. Density dependence in host-parasitoid models. *J. Animal Ecol.*, 50:855–865, 1981.

[62] N. J. Mills and W. M. Getz. Modelling the biological control of insect pests: A review of host–parasitoid models. *Ecol. Model.*, 92:121–143, 1996.

[63] H. Minc. *Nonnegative Matrices*. John Wiley & Sons, New York, 1988.

[64] W. W. Murdoch, C. J. Briggs, and R. M. Nisbet. *Consumer-Resource Dynamics*. Princeton University Press, Princeton, 2003.

[65] J. D. Murray. *Mathematical Biology I: An Introduction*. Springer, New York, 2002.

[66] J. H. Myers and D. R. Bazely. *Ecology and Control of Introduced Plants*. Cambridge University Press, Cambridge, 2003.

[67] R. Nathan, E. Klein, J. J. Robledo-Arnucio, and E. Revilla. Dispersal kernels: Review. In J. Clobert, M. Baguette, T. G. Benton, and J. M. Bullock, editors, *Dispersal Ecology and Evolution*, pages 187–210. Oxford University Press, Oxford, 2012.

[68] M. G. Neubert and M. Kot. The subcritical collapse of predator populations in discrete-time predator-prey models. *Math. Biosci.*, 110:45–66, 1992.

[69] M. G. Neubert, M. Kot, and M. A. Lewis. Invasion speeds in fluctuating environments. *Proc. Biol. Sci.*, 267:1603–1610, 2000.

[70] A. J. Nicholson. An outline of the dynamics of animal populations. *Aust. J. Zool.*, 2:9–65, 1954.

[71] A. J Nicholson and V. A. Bailey. The balance of animal populations.— Part I. *Proc. Zool. Soc. Lond.*, 1935 (often renumbered 105 ex post facto):551–598, 1935.

[72] C. Parmesan. Ecological and evolutionary responses to recent climate change. *Annu. Rev. Ecol. Evol. Syst.*, 37:637–669, 2006.

[73] C. Parmesan and G. Yohe. A globally coherent fingerprint of climate change impacts across natural systems. *Nature*, 421:37–42, 2003.

[74] A. Phillips and M. Kot. Persistence in a two-dimensional moving-habitat model. *Bull. Math. Biol.*, 77:2125–2159, 2015.

[75] A. B. Potapov and M. A. Lewis. Climate and competition: the effect of moving range boundaries on habitat invasibility. *Bull. Math. Biol.*, 66:975–1008, 2004.

[76] W. H. Press, S. A. Teukolsky, W. T. Vetterling, and B. P. Flannery. *Numerical Recipes in C*. Cambridge University Press, Cambridge, 1992.

[77] J. R. Reimer, M. B. Bonsall, and P. K. Maini. Approximating the critical domain size of integrodifference equations. *Bull. Math. Biol.*, 78:72–109, 2016.

[78] W. E. Ricker. Stock and recruitment. *J. Fish Res. Board Can.*, 11:559–623, 1954.

[79] D. S. Rinnan. The dispersal success and persistence of populations with asymmetric dispersal. *Theor. Ecol.*, 11:55–69, 2018.

[80] D. S. Rinnan. Population persistence in the face of climate change and competition: A battle on two fronts. *Ecol. Model.*, 385:78–88, 2018.

[81] J. Roland and P. D. Taylor. Herbivore–natural enemy interactions in fragmented and continuous forests. In N. Cappuccino and P. W Price, editors, *Population Dynamics: New Approaches and Synthesis*, pages 195–208. Academic Press, San Diego, California, 1995.

[82] J. Roland and P. D. Taylor. Insect parasitoid species respond to forest structure at different spatial scales. *Nature*, 386:710–713, 1997.

[83] M. L. Rosenzweig. Paradox of enrichment: Destabilization of exploitation ecosystems in ecological time. *Science*, 171:385–387, 1971.

[84] A. J. Schwenk. Tight bounds on the spectral radius of asymmetric nonnegative matrices. *Linear Algebra Appl.*, 75:257–265, 1986.

[85] S. Strohm and R. C. Tyson. The effect of habitat fragmentation on cyclic population dynamics: a reduction to ordinary differential equations. *Theor. Ecol.*, 5:495–516, 2012.

[86] D. B. Taylor, R. D. Moon, J. B. Campbell, D. R. Berkebile, P. J. Scholl, A. B. Broce, and J. A. Hogsette. Dispersal of stable flies (Diptera: Muscidae) from larval development sites in a Nebraska landscape. *Environ. Entomol.*, 39:1101–1110, 2010.

[87] R. a. J. Taylor. The relationship between density and distance of dispersing insects. *Ecol. Entomol.*, 3:63–70, 1978.

[88] W. R Thompson. Biologie-théorie de l'action des parasites entomophages. les formules mathématiques du parasitisme cyclique. *CR Acad. Sci. Paris*, 174:1201–1204, 1922.

[89] W. R. Thompson. La théorie mathématique de l'action des parasites entomophages et le facteur du hasard. *Ann. Fac. Sci. Marseille*, 2:69–89, 1924.

[90] W. R Thompson. On the effect of random oviposition on the action of entomophagous parasites as agents of natural control. *Parasitology*, 21:180–188, 1929.

[91] P. Turchin. *Complex Population Dynamics: A Theoretical/Empirical Synthesis*. Princeton University Press, Princeton, NJ, 2013.

[92] J. Umbanhowar and A. Hastings. The impact of resource limitation and the phenology of parasitoid attack on the duration of insect herbivore outbreaks. *Theor. Popul. Biol.*, 62:259–269, 2002.

[93] M. C. Urban. Accelerating extinction risk from climate change. *Science*, 348:571–573, 2015.

[94] M. C. Urban, P. L. Zarnetske, and D. K. Skelly. Moving forward: dispersal and species interactions determine biotic responses to climate change. *Ann. N. Y. Acad. Sci.*, 1297:44–60, 2013.

[95] R. W. Van Kirk and M. A. Lewis. Integrodifference models for persistence in fragmented habitats. *Bull. Math. Biol.*, 59:107–137, 1997.

[96] G. C. Varley, G. R. Gradwell, and M. P. Hassell. *Insect Populatin Ecology: An Analytical Approach*. University of California Press, Berkeley, 1974.

[97] B. Wallace. On the dispersal of *Drosophila*. *Am. Nat.*, 100:551–563, 1966.

[98] Y. H. Wang and A. P. Gutierrez. An assessment of the use of stability analyses in population ecology. *J. Animal Ecol.*, 49:435–452, 1980.

[99] D. Whitley. Discrete dynamical systems in dimensions one and two. *Bull. London Math. Soc.*, 15:177–217, 1983.

[100] S. Wiggins. *Introduction to Applied Nonlinear Dynamical Systems and Chaos*. Springer, New York, 2010.

[101] D. O. Wolfenbarger. Dispersion of small organisms, distance dispersion rates of bacteria, spores, seeds, pollen, and insects; incidence rates of diseases and injuries. *Am. Midl. Nat.*, 35:1–152, 1946.

[102] D. O. Wolfenbarger. Dispersion of small organisms, incidence of viruses and pollen; dispersion of fungus, spores, and insects. *Lloydia*, 22:1–106, 1959.

[103] D. O. Wolfenbarger. *Factors Affecting Dispersal Distances of Small Organisms*. Exposition Press, Hicksville, New York, 1975.

[104] L. Yeh. Inequalities for the maximal eigenvalue of a nonnegative matrix. *Glasg. Math. J.*, 39:276–284, 1997.

[105] Y. Zhou and M. Kot. Discrete-time growth-dispersal models with shifting species ranges. *Theor. Ecol.*, 4:13–25, 2011.

[106] Y. Zhou and M. Kot. Life on the move: Modeling the effects of climate-driven range shifts with integrodifference equations. In M. A. Lewis, P. K. Maini, and S. V. Petrovskii, editors, *Dispersal, Individual Movement and Spatial Ecology: A Mathematical Perspective*, pages 263–292. Springer, Berlin, 2013.